Univerzita Karlova v Praze
Matematicko-fyzikální fakulta

DIPLOMOVÁ PRÁCE

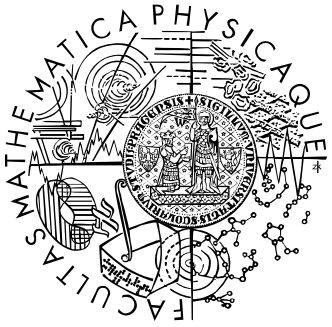

Bc. Simona Burianová

Magnetismus v oxidech tranzitivních kovů

Katedra fyziky kondenzovaných látek

Vedoucí diplomové práce: RNDr. Jana Poltierová Vejpravová, Ph.D.

Studijní program: Fyzika, Fyzika kondenzovaných soustav a materialů

Charles University of Prague
Faculty of mathematics and physics

DIPLOMA THESIS

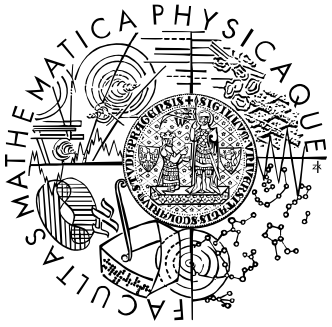

Bc. Simona Burianová

Magnetism in transition metal oxides

Department of Condensed Matter Physics

Supervisor: RNDr. Jana Poltierová-Vejpravová, Ph.D.

Study program: Physics, Physics of condensed matter and materials

Ráda bych zde poděkovala své vedoucí RNDr. Janě Poltierové Vejpravové, Ph.D. za její pomoc a čas, který mi věnovala. Také bych chtěla poděkovat RNDr. Danielu Nižňanskému, Ph.D. za jeho pomoc při měření a vyhodnocení Mössbauerovy spektroskopie. Dále bych chtěla poděkovat Mgr. Petru Holcovi za přípravu vzorků použitých v této práci.

Prohlašuji, že jsem svou diplomovou práci napsala samostatně a výhradně s použitím citovaných pramenů. Souhlasím se zapůjčováním práce.

V Praze dne 15.4.2010 Simona Burianová

Contents:

Název práce: Magnetismus v oxidech tranzitivnich kovů
Autor: Simona Burianová
Katedra (ústav): Katedra fyziky kondenzovaných látek
Vedoucí bakalářské práce: RNDr. Jana Poltierová Vejpravová, Ph.D.
E-mail vedoucího: jana@mag.mff.cuni.cz

Abstrakt:
Nanokrystaly $CoFe_2O_4$ jsou velice atraktivní materiály především díky svým magnetickým vlastnostem – vysoké koercivitě (dosahující 2 T v nízkých teplotách), přiměřené saturované magnetizaci (80 $A.m^2.kg^{-1}$), značné chemické stabilitě a mechanické pevnosti. Dopováním těchto materialů pomocí prvků vzácných zemin se dá očekávat významná změna těchto vlastností. Tato práce je zaměřena na zkoumání vzorků nanočástic $Co_{1-x}La_xFe_2O_4$, x = 0.05 – 0.5 and $CoLa_xFe_{2-x}$ O_4 x = 0.05 – 0.2. Vzorky byly připraveny metodou sol-gel a mikroemulzní metodou, s různou velikostí částic závisející na teplotě žíhání. Nanočástice připravené metodou sol-gel byly zapouzdřeny v SiO_2 matrici, zatímco nanočástice připravené mikroemulzní metodou byly bez matrice. Charakterizace vzorků byla provedena pomocí rentgenové difrakce a Mössbauerovy spektroskopie. Z měření teplotních závislostí magnetizace známé jako ZFC-FC měření bylo zjištěno, že teplota blokace je nad pokojovou teplotu. Koercivita a saturovaná magnetizace je ovlivněna velikostí částic, která je určena metodou přípravy. Vysokou koercivitu kolem 2 T při 10 K vykazují vzorky připravené metodou sol-gel. Dosažené výsledky jsou diskutovány vzhledem k metodě přípravy, velikostí částic a stupni La dopování.
Klíčová slova: nanočástice $CoFe_2O_4$, metoda sol-gel, mikroemulzní metoda, vysoká koercitivita

Title: Magnetism in transition metal oxides
Author: Simona Burianová
Department: Department of Condensed Matter Physics
Supervisor: RNDr. Jana Poltierová Vejpravová, Ph.D.
Supervisor's e-mail address: jana@mag.mff.cuni.cz

Abstract:
The $CoFe_2O_4$ nanocrystals are highly attractive due to their magnetic properties - large coercivity (up to 2 T at low temperatures) with moderate saturation magnetization (80 $A.m^2.kg^{-1}$), remarkable chemical stability and mechanical hardness. Upon RE doping, a significant change of the properties is expected. This thesis is focused on investigation of $Co_{1-x}La_xFe_2O_4$, x = 0.05 – 0.5 and $CoLa_xFe_{2-x}$ O_4 x = 0.05 – 0.2 nanoparticles prepared by sol-gel and microemulsion method, respectively, with varying particle size according to the final heat treatment. In the former case, the particles were embedded in amorphous SiO_2 matrix, while in the latter case, the samples were matrix-free. The samples were characterized using X-ray diffraction and Mössbauer spectroscopy. Measurements of the temperature dependence of the ZFC-FC magnetization revealed that the blocking temperature is above the room temperature. The values of coercivity and saturation magnetization strongly depend on particles size determined by method of preparation. The higher coercivity values of about 2 T at 10 K show the samples prepared by the sol-gel method. The obtained results are discussed in the context of preparation method, particle size and level of La doping.
Keywords: $CoFe_2O_4$ nanoparticles, sol-gel method, microemulsion route, high coercivity

1. Motivations and aims of the work

Magnetic nanoparticles are under intensive research within last years due to their physical properties that are very different from the bulk material [1-2]. Due to the wide range of possible applications, the requirements on variety of magnetic properties are imposed, mostly on the blocking temperature, coercivity and saturation magnetization. One of the promising groups are transition metal oxides, especially the spinel ferrite nanoparticles as their properties highly depend on cation distribution within the lattice [3-4].

The cobalt ferrite nanoparticles are well-known for their large coercivity and reasonable saturation magnetization [5-6] and also promising dielectric properties [7] that can be utilized in many fields of application, e.g. in high-density recording and biomedicine [8]. Other advantages of these materials are their mechanical hardness and chemical stability. They can be prepared by various methods as sol-gel, co-precipitation or microemulsion.

The diploma thesis is therefore highly motivated with attempt to improve and control the structure and magnetic properties of $CoFe_2O_4$ nanoparticles. One of the possibilities is doping them by rare earth elements that, as was predicted, should affect the structure and magnetic properties of spinels, particularly to enhance the coercivity by introducing other source of the spin-orbital interaction. Only few studies of these materials have been done with contrary results [9-12] and a complex study is therefore highly needed. This thesis is concentrated on structural and magnetic properties of $CoFe_2O_4$ nanoparticles upon La doping.

Aims of the work are summarized as follows:

1) study of the influence of preparation method on particle size and crystallinity,

2) study of the influence of final treatment on particle size prepared by the sol-gel method,

3) effect of La doping on cation distribution in spinel structure and its influence on magnetic properties,

4) influence of La doping on the spin canting.

The diploma thesis starts with motivation and aims of the work followed by the theoretical part where the general information on magnetism is briefly summarized, then magnetism in transition metals and the key principles of magnetism of magnetic nanoparticles are discussed. Afterwards, the details of the spinel crystal structure and the influence of the rare earth doping are shown and the crystal structures of the compounds formed in samples are presented.

In the experimental part the general idea and differences of the preparation routes used (the microemulsion route and the sol-gel method) are discussed. Then the characterization of samples by X-ray diffraction, transmission electron microscopy and Mössbauer spectroscopy is described. The Mössbauer spectroscopy is one of the unique techniques for studying the microstructural and magnetic environments in materials.

This method was used to study the cation distribution within the spinel network and to determine the spin canting angle that affects the values of the saturation magnetization. Methods of magnetic measurements, the SQUID and VSM magnetometers, are also discussed.

The results are divided into three parts. In the first part, the results of the samples prepared by the microemulsion route are discussed, mainly the characterization of the samples obtained by X-ray diffraction, transmission electron microscopy and Mössbauer spectroscopy and the magnetic properties (coercivity, saturation and remanent magnetization). In the second part, the same discussion is made for samples prepared by the sol-gel method. In the third part, comparison of the obtained results is presented.

Finally, conclusions to the presented results are given followed by appendix and references used in the thesis.

2. Theoretical part

2.1. Introduction to magnetism

In this chapter the fundamentals of magnetism in condensed matter will be briefly described – the origin of magnetism, interactions between magnetic moments that lead to magnetic ordering in materials, and types of the magnetic ordering. The chapter is based on [13-15].

2.1.1. List of used constants

In all equations of the theoretical part the SI units are used. There is a list of constants that are used in the thesis:

Boltzmann constant	$k_B = 1.38.10^{-23}$ J.K^{-1}
Electron mass	$m_e = 9.11.10^{-31}$ kg
Bohr magneton	$\mu_B = 9.27.10^{-24}$ J.T^{-1}
Elementary electric charge	$e = 1.602.10^{-19}$ C
Vacuum permeability	$\mu_0 = 4\pi.10^{-7}$ N.A^{-2}

2.1.2. Basics magnetic terms

The fundamental object in magnetism is the magnetic moment, μ that is connected with the current loop in classical physics that occurs because of the motion of one or more electrons (electrical charges). A magnetic solid consists of a large number of atoms with magnetic moments; hence the quantity magnetization M is defined as the quantity of magnetic moment per unit volume V:

$$M = \frac{1}{V}\sum_j \mu_j \tag{2.1}$$

where the sum is taken over the whole magnetic atoms in the solid.

For describing the magnetic field, the two vector fields are defined - B called the magnetic induction and H called the magnetic field strength or intensity. In free space (vacuum) they are linearly related by:

$$B = \mu_0 H \tag{2.2}$$

In a magnetic solid the relation is modified as:

$$B = \mu_0 (H + M) \tag{2.3}$$

The degree of magnetization, M of a material in response to the applied magnetic field, H is defined by the dimensionless quantity called the magnetic susceptibility:

$$\chi = \frac{\partial M}{\partial H} \tag{2.4}$$

2.1.3. Magnetism in non-interacting system

In this section, the isolated magnetic moments are considered. It means that the interactions between magnetic moments on different atoms are ignored. The perturbed Hamiltonian for an atom in a uniform magnetic field B can be written as:

$$\hat{H} = \hat{H}_0 + \mu_B (L + gS).B + \frac{e^2}{8m_e} \sum_i (B \times r_i)^2 \tag{2.5}$$

$$\hat{H}_0 = \sum_{i=1}^{Z} \left(\frac{p_i^{\,2}}{2m} + V_i \right) \tag{2.6}$$

where g is an electron spin g-factor, generally defined as the Landé g-factor:

$$g_J = \frac{3}{2} + \frac{S(S+1) - L(L+1)}{2J(J+1)} \tag{2.7}$$

and r_i the position of i^{th} electron in atom, H_0 is the original Hamiltonian that consists of the electronic kinetic energy (the first term in (2.6)) and the potential energy (second term in (2.6)). The sum is taken over all Z electrons in atom.

As the perturbation in Hamiltonian is quite small on the scale of atomic excitation energies, the changes in the energy levels induced by the field can be computed with ordinary perturbation theory. The susceptibility can be calculated as a second derivative with respect to the magnetic field, second-order perturbation theory in B is used:

$$\Delta E = \mu_B \vec{B}\left(\langle n | \vec{L} + g\vec{S} | n \rangle\right) + \sum_{n' \neq n} \frac{\left| \langle n | \mu_B \vec{B}\left(\vec{L} + g\vec{S}\right) | n' \rangle \right|^2}{E_n - E_{n'}} + \frac{e^2}{8m_e} \langle n | \sum_i \left(B \times r_i\right)^2 | n \rangle \tag{2.8}$$

The first two terms in equation (2.8) are known as the paramagnetic terms, the third term is due to the diamagnetic contribution.

2.1.3.1. Diamagnetism

For a diamagnetic material it is typical that the external magnetic field induces a magnetic moment that points in opposite direction to this external field. Therefore the diamagnetic susceptibility is negative. If no unfilled shells in spherically symmetric atom are supposed (hence the paramagnetic terms in (2.8) vanish), the relation for the diamagnetic susceptibility is given by:

$$\chi_d = -\frac{N}{V} \frac{e^2 \mu_0}{6m_e} \sum_{i=1}^{Z} \left\langle r_i^{\,2} \right\rangle \tag{2.9}$$

where V is the solid volume, N is number of ions with Z electrons of mass m_e.

The term is known as the Larmor diamagnetic susceptibility and it is temperature and field independent. This equation should describe the magnetic response of solid noble gases and of simple ionic crystals etc. Diamagnetism occurs in every material but it is only a weak perturbation that can be ignored in most cases.

2.1.3.2. Paramagnetism

In a paramagnetic material the magnetic moment that is induced by an applied external field is linear with this field; hence the magnetic susceptibility is positive. Unfilled shells are considered (the paramagnetic terms in (2.8) are then non-zero), therefore atoms have non-zero magnetic moment even without the applied field. As L and S weakly couple via the spin-orbit interaction and they are not separately conserved, it is useful to define the total angular momentum, J that is conserved:

$$J = L + S \tag{2.10}$$

The paramagnetic susceptibility is computed in two different cases:

1) The electron configuration with $J = 0$

This is the case for shells that are one electron short of being half filled and the ground state is nondegenerate. The first term in (2.8) vanishes and from the second and third terms, the magnetic susceptibility is given by:

$$\chi = \frac{N}{V}\left(2{\mu_B}^2 \sum_n \frac{\left|\langle 0|(L_z + gS_z)|n\rangle\right|^2}{E_n - E_0} - \frac{e^2\mu_0}{6m_e}\sum_{i=1}^{Z}\left\langle {r_i}^2 \right\rangle \right) \tag{2.11}$$

The second term is the known Larmor diamagnetic susceptibility discussed above. The first term is known as the Van Vleck paramagnetism and it is positive (because $E_n > E_0$) and temperature independent.

2) The electron configuration with $J \neq 0$:

It is in all cases except the one that was discussed above. The first term in energy shift (2.8) will not vanish and as is much larger than the other two they can safely be ignored. The mean value of the magnetization is given by:

$$M = ng_J\mu_B J.B_J\left(\frac{\mu_B JB}{k_B T}\right) \tag{2.12}$$

where B_J is the Brillouin function.

Except at very low temperatures and/or extremely large magnetic fields, the experimental situation will correspond to small argument in the Brillouin function. Using the Maclaurin expansion the susceptibility is given as:

$$\chi = \frac{n\mu_0{\mu_{eff}}^2}{3k_B T} = \frac{C}{T} \tag{2.13}$$

where $\mu_{eff} = g_J\mu_B\sqrt{J(J+1)}$ is the effective moment.

The variation of the susceptibility inversely with temperature (see Figure 2.1) is known as the Curie law. This equation presents a typical behavior of paramagnetic materials – the alignment of magnetic moments is favored by the magnetic field and opposed by the thermal disorder. The paramagnetic susceptibility is much larger than the temperature-independent Larmor diamagnetic susceptibility therefore for an ion with partially filled shell with nonzero J, the diamagnetic contribution to the susceptibility is negligible.

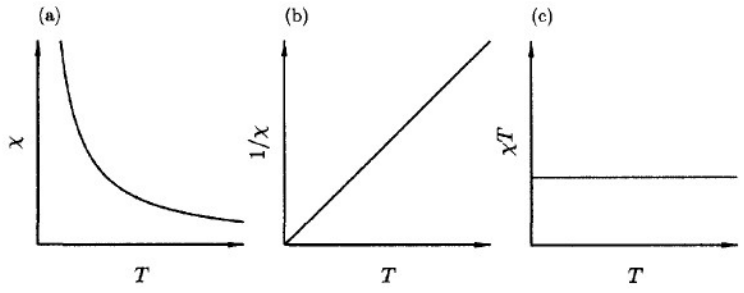

Figure 2.1: The plot of the Curie law in different representations [13].

2.1.3.3. Contributions of conduction electrons

In the previos section the susceptibility for insulators where the magnetic moment is due to the localized electrons in partially filled ionic shells was derived. However the conduction electrons contribute to the magnetic moment of metals. The resulting paramagnetic susceptibility (known as the Pauli susceptibility) is given by:

$$\chi_P \approx \mu_0 {\mu_B}^2 g(E_F) = \frac{3n\mu_0 {\mu_B}^2}{2E_F} \tag{2.14}$$

In contrast to the susceptibility of paramagnetic ions (2.13), the Pauli susceptibility is essentially independent on temperature and moreover it is much smaller.

Another contribution of the conduction electrons to the magnetic moment is the Landau diamagnetism that is due to the orbital electronic motion induced by the magnetic field. For free electrons it can be shown that:

$$\chi_L = -\frac{1}{3}\chi_P \tag{2.15}$$

2.1.3.4. The particular magnetic susceptibilities

The characteristic behaviors of the particular contributions to the magnetic susceptibility of diamagnetic and paramagnetic substances are displayed in Figure 2.2.

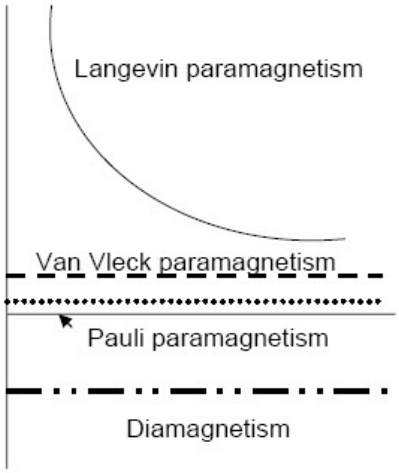

Figure 2.2: Characteristic magnetic susceptibilities of diamagnetic and paramagnetic substances.

2.1.4. Interactions in magnetic materials

The main interactions that are responsible for magnetic ordering in solids will be now described.

The most important interaction is the exchange interaction that is purely quantum mechanical effect. It is a result of the fact that the wave function of indistinguishable particles is subjected to the exchange symmetry resulting in electric repulsion and the Pauli exclusion principle. The equation was firstly derived by Heisenberg:

$$\hat{H} = -\sum_{i,j} J_{ij} \hat{S}_i \hat{S}_j \tag{2.16}$$

where J_{ij} is the exchange constant between i^{th} and j^{th} spin, respectively.

There are several types of the exchange interaction:

a) direct exchange

The direct exchange proceeds between neighboring magnetic moments that have sufficient overlap of their wave functions (see Figure 2.3 (a)). Therefore there is no need for an intermediary. The direct interaction is unfavored in most elements and materials because most of the orbitals are localized and lie very close to nucleus. Thus in many magnetic materials it is necessary to consider some kind of indirect exchange interaction. The indirect interaction orders magnetic moments over large distances. It acts through an intermediary, which in metals are the conduction electrons or it can be a nonmagnetic element (known as the superexchange).

b) RKKY interaction

The RKKY interaction is named after Ruderman, Kittel, Kasuya and Yoshida, who discovered the effect. A localized magnetic moment spin-polarizes the conduction electrons and these conduction electrons then interact with neighboring localized magnetic moment a distance r away (see Figure 2.3 (c)). The interaction is long range and has an oscillatory dependence on the distance between the magnetic moments.

c) Superexchange

The superexchange proceeds between non-neighboring magnetic ions and is mediated by non-magnetic ion, which is placed between the magnetic ions (see Figure 2.3 (b)). The interaction mainly occurs in ionic salts as MnO or MnF_2.

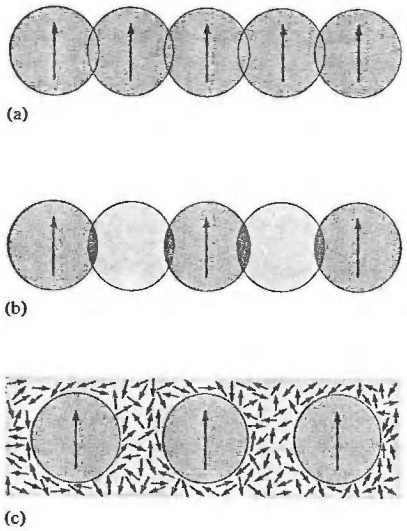

Figure 2.3: Schematic illustrations of (a) direct exchange, in which the magnetic ions interact because their charge distribution overlap; (b) superexchange, in which the magnetic ions with no overlapping charge distributions interact because both have overlap with the same nonmagnetic ion; and (c) indirect exchange, in which in the absence of overlap a magnetic interaction is mediated by interactions with the conduction electrons [14].

2.1.5. Magnetic ordering

The result of the operating interactions that were discussed above is the magnetic ordering without applied field. The description of the basic magnetic ground states (see Figure 2.4) will be now discussed.

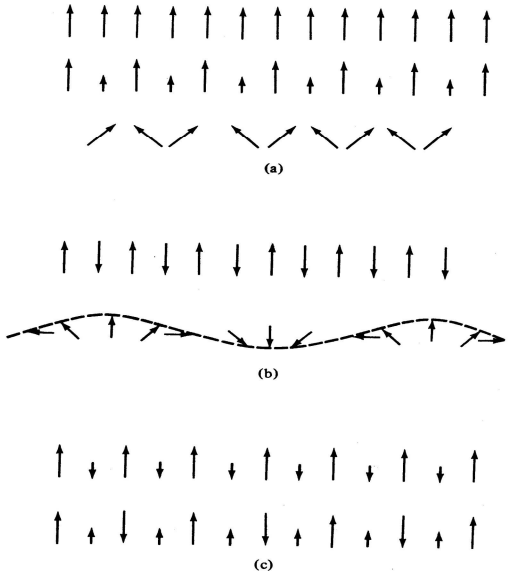

Figure 2.4: Various spin arrangements in ordered systems: (a) ferromagnets, (b) antiferromagnets, (c) ferrimagnets [15].

2.1.6. Ferromagnetism

Generally, ferromagnets are described as materials where all magnetic moments lie along a single unique direction. The exchange constant, J_{ij} is positive.

2.1.6.1. Weiss model of ferromagnetism – Mean field theory

The mean field theory that was developed by P. Weiss was one of the first attempts how to quantitatively analyze the behavior of ferromagnets and their transitions to paramagnetic state. Although this theory has lots of inadequacies (as inadequate picture of the critical region) it is always taken as a starting point for viewing the basic properties of ferromagnets.

The energy of the i^{th} spin in ferromagnet has two parts – the Zeeman part and the exchange part. The following approximation is made – the exchange interaction is replaced by an effective molecular field, B_{mf} produced by the neighboring spins. The effective Hamiltonian can be written as:

$$\hat{H} = g\mu_B \sum S_i \left(B + B_{mf}\right) \tag{2.17}$$

it looks like the Hamiltonian for a paramagnet in a magnetic field $B+B_{mf}$. The essence of the approximation is that all magnetic ions experience the same effective molecular field. Since the molecular field measures the effect of the ordering of the system one can assume that:

$$B_{mf} = \lambda M \tag{2.18}$$

where λ is a constant that parametrizes the strength of the molecular field as a function of magnetization.

At low temperatures the magnetic moments can be ordered because of the molecular field even without an applied field. As the temperature raises the thermal fluctuations become more important and at some point they exceed the energy related to the molecular field and the magnetic moments become disordered. Therefore there exists a critical temperature at which the ferromagnetic material becomes paramagnetic. The transition is a second-order phase transition. To find the critical temperature that is for ferromagnets called the Curie temperature the analogues problem as in paramagnets is solved but now with the additional molecular field. The derivation is well described in [13-14] and the solution for the critical temperature is given by:

$$T_C = \frac{n\lambda\mu_{eff}^{\ 2}}{3k_B} \tag{2.19}$$

and the susceptibility above the Curie temperature is given by:

$$\chi = \frac{C}{T - T_C} \tag{2.20}$$

which is known as the Curie-Weiss law (see Figure 2.5). The Curie temperature corresponds to the so-called Weiss critical temperature as $T_C \sim \theta_p$.

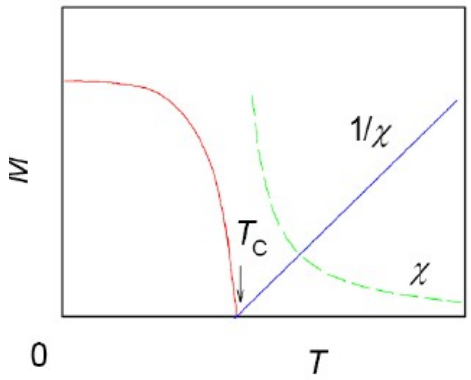

Figure 2.5: The temperature dependence of the magnetization and the susceptibility in ferromagnetic material [15].

2.1.6.2. Magnetic domains

In real system the magnetization of ferromagnets (or ferrimagnets) is divided into small regions called domains, within each the local magnetization reaches the saturation value, but the magnetization of each domain points in different direction. The formation of the domain is balancing the dipolar energy and the exchange energy due to spins near domain boundaries (see Figure 2.6), the domain walls.

The width of the domain wall depends on the exchange energy that favor to spread out the reversal of spin direction over many spins and on the anisotropy energy contracting the domain wall. The total energy per unit area, σ including both contributions is given by:

$$\sigma = JS^2 \frac{\pi^2}{Na^2} + \frac{NKa}{2} \tag{2.21}$$

where J is the exchange constant, N the numbers of rotating spins in the wall, a wall length and K the anisotropy constant, respectively.

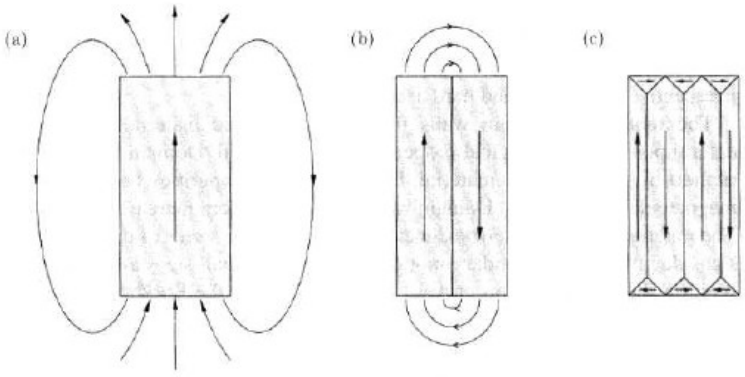

Figure 2.6: A sample which is (a) uniformly magnetized, (b) divided into two domains, (c) with a simple domain closure structure [13].

2.1.6.3. Hysteresis loop

The feature in which the ferro-materials differ from paramagnetic or diamagnetic materials is the character of the magnetization dependence on the applied field. The observed curve is known as the hysteresis loop (see Figure 2.7). If the sample is magnetized to the saturation magnetization, M_s by the applied field, then the applied field is reduced to zero when the magnetization reduces to the so-called remanent magnetization, M_r. The magnetic field equal to the coercive field, H_c is needed to switch the magnetization into the opposite direction. The parameters M_r and H_c are usually used to characterize a ferromagnet.

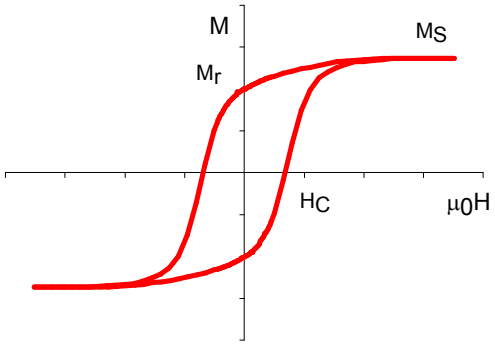

Figure 2.7: A hysteresis loop showing the saturation magnetization M_s, the remanent magnetization M_r, and the coercive field H_c.

2.1.7. Antiferromagnetism

Antiferromagnets are magnetically ordered materials where the local magnetic moments sum to zero total moment and hence there is no spontaneous magnetization. The simplest model of antiferromagnet is when the nearest neighbor magnetic moments are oriented antiparallel to each other. It can be considered as two interpenetrating sublattices of identical magnetic structure. Within each sublattice the moments have the same magnitude and average direction, but the net moments of the two sublattices are oppositely directed, summing to zero total moment (see Figure 2.8). The model is described by the Néel theory of sublattices. The exchange constant, J_i, is negative between two sublattices and positive within each sublattice.

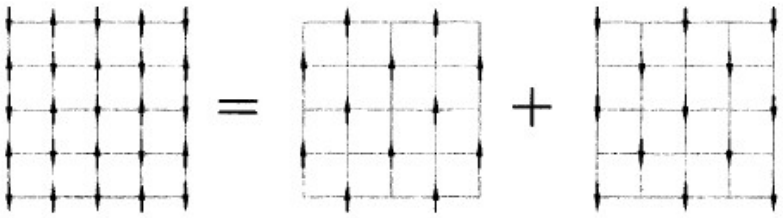

Figure 2.8: An antiferromagnet can be decomposed into two interpenetrating sublattices [13].

Considering the two sublattices the magnetic susceptibility can be calculated in same way as in ferromagnetic case. It is assumed that the molecular field acting on one sublattice is proportional to the magnetization of the other sublattice. For each sublattice the situation is identical to ferromagnets, there exist a critical temperature called the Néel temperature above which the magnetization disappears. The magnetic susceptibility above the Néel temperature is given by:

$$\chi = \frac{C}{T + T_N} \tag{2.22}$$

The relation looks pretty similar to the Curie-Weiss law but with the term $-T_C$ replaced by the $+T_N$. The result gives interpretation of the susceptibility data in the paramagnetic state. The data can be fitted to the Curie-Weiss law and the sign of the critical temperature, Θ_p suggests if the material is ferromagnetic ($\Theta_p > 0$, see Figure 2.5) or antiferromagnetic ($\Theta_p < 0$, see Figure 2.9).

The behavior of the susceptibility below the Néel temperature is more complicated than in ferromagnets because it strongly depends on orientation of the applied field.

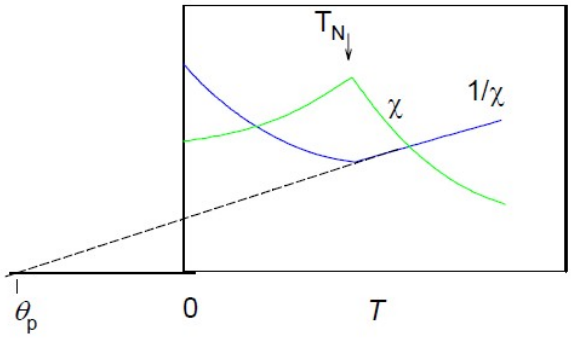

Figure 2.9: The temperature dependence of the susceptibility in antiferromagnetic material [15].

2.1.8. Ferrimagnetism

In the previos discussion two equivalent sublattices were considered. In the case where the magnetization of the two sublattices is not equal (e.g. neighboring magnetic ions are not identical), the net magnetization will occur and this phenomenon is called ferrimagnetism. Because the molecular field on each sublattice is different, the temperature dependence of the net magnetization and the susceptibility, respectively is quite complicated. The M_a and M_b are defined as the magnetization of the two sublattices A and B. Below the Curie temperature the both magnetizations increase with increasing temperature, however the temperature behavior for partial magnetization is different. If the net magnetization, M is the sum of the M_a and M_b, it has the same characteristic behavior as ferromagnets. However if the net magnetization, M is determined by antiparallel orientation of M_a and M_b with respect to each other, the temperature behavior of the net magnetization shows anomal behavior as is presented in Figure 2.10. In the first type of anomaly, the M can be zero even below the T_c as the M_a

and M_b are equal at this point, and therefore the total magnetization, M reduces to zero (Type N). This temperature is known as the compensation temperature, θ_k. The second type of anomaly can occur when one of the partial magnetizations has more rapid decrease than the other. Then the M has maximum at T > 0 (Type P).
Above the Curie temperature the magnetic susceptibility does not follow the Curie-Weiss law.

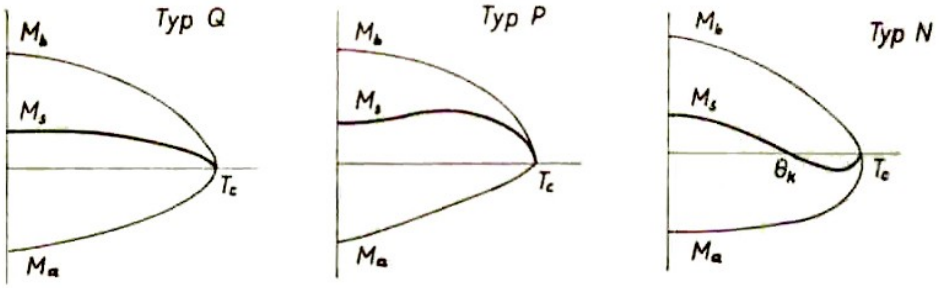

Figure 2.10: Basics types of magnetization dependence on temperature for ferrimagnets with two sublattices A, B orientated antiparallel with respect to each other [16].

2.2. Magnetism of 3*d* ions (ferrite oxides)

The specificity of magnetism of 3*d* ions will be now described. The representatives of 3*d* ions are Co^{2+}, Fe^{2+} or Fe^{3+}. As the 3*d* orbitals are extended further from nucleus an influence of the chemical environment has to be taken into account. To model this influence, the crystal field theory (CFT) was developed in 1930s by Hans Bethe and John Hasbrouck van Vleck. More information about the magnetism of 3*d* ions can be found in references that were used [13, 16].

2.2.1. Crystal field theory

The crystal field is an electric field originated by neighboring atoms in the crystal that are modelled as negative point charges. The model assumes that electrons are localized in the vicinity of the cations and lift the degeneracy of the energy of their states caused by the electrostatic field of its surrounding. The disadvantage of this theory is that it does not include the covalent effects. For calculation of the influence of both the covalence and the crystal field, the ligand field theory was developed. However, the basics of the influence of the environment can be well-described by the crystal field theory.

In case of spherically symmetric environment, the energies of all five *d*-orbitals are degenerated. The environment with lower symmetry (as cubic) causes splitting of the energy of the *d*-orbitals. The character of the splitting depends on the symmetry of the local environment and also on the symmetry of *d*-orbitals. The angular dependences of *d*-orbitals are shown in Figure 2.11.

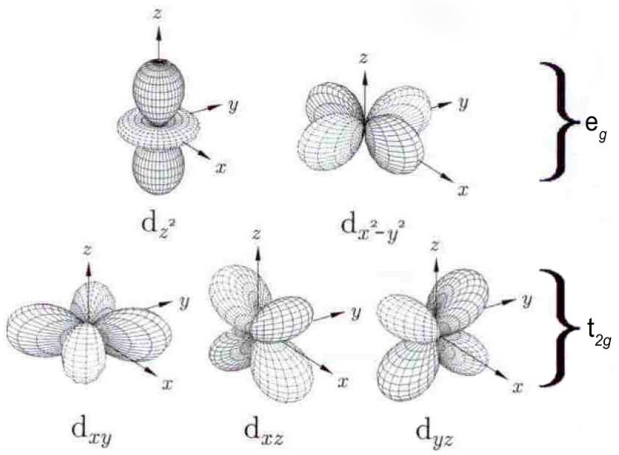

Figure 2.11: Angular dependence of *d*-orbitals. From symmetry view they can be divided into two groups – e_g (*e*) where orbitals point along the x, y, z axis and t_{2g} (t_2) orbitals that point between these axes [13].

In the case of the cubic symmetry (e.g. octahedral, tetrahedral environment) the *d*-orbitals can be divided into two classes with respect to their equivalency and energy degeneracy. The three orbitals that point between the x, y, z axes are called t_{2g} or t_2

orbitals for the octahedral and tetrahedral environment, respectively. The two orbitals pointing along these axes are called e_g or e orbitals. This notation of d-orbitals comes from the group theory – e is the two-fold degeneracy, t_2 is the three-fold degeneracy and g is correspondent with the centre of inversion.

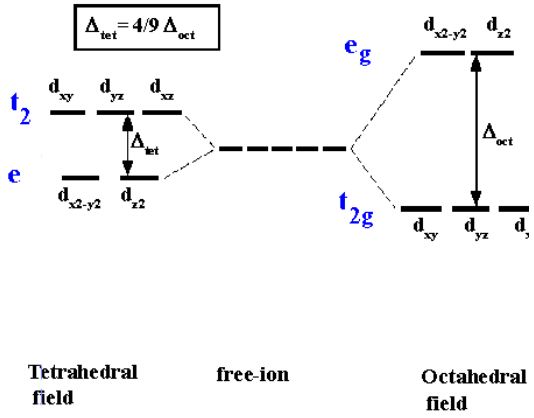

Figure 2.12: The splitting of d-orbitals caused by the crystal field [17].

In the tetrahedral environment the crystal field splits the d-orbitals oppositely than in the octahedral case, therefore the e orbitals have lower energy than the t_2 orbitals. The splitting in both cases is displayed in Figure 2.12.

The energy difference of the splitting is known as the crystal-field splitting parameter Δ and it depends on the geometry of the surrounding and kind of the cation and its electric charge. Because in the tetrahedral environment the ligand electrons are not oriented towards the d-orbitals, the energy splitting will be lower than in the octahedral environment:

$$\Delta_{octa} = \frac{9}{4}\Delta_{tetra} \tag{2.23}$$

In cases of lower symmetries an additional splitting of the t_{2g} (t_2) and e_g (e) orbitals is observed.

2.2.2. Consequences of the crystal field

2.2.2.1. Low spin and high spin configuration

As was shown in the previos section there are partially degenerated orbitals in the presence of the crystal field. Therefore the question how to fill them with electrons arises. The filling depends on competition between the crystal field and the Coulomb energy cost of putting two electrons in the same orbital. This competition can be divided into two cases. At first if the energy of the crystal field is lower than the Coulomb energy, the electrons at first singly occupy each orbital and after doubly occupy the lower-energy orbitals. This configuration is known as the high-spin configuration. On the other hand, if the crystal field is stronger than the Coulomb energy, electrons at first

doubly occupy the lower-energy orbitals and afterwards they occupy the high-energy orbitals. This configuration is known as the low-spin configuration.
The so-called spectrochemical serie was derived to demonstrate the approximate strength of the crystal field of the ligands. The oxygen anions that create the crystal field in case of ferrites belong to ligands with weak effect and therefore the ions of iron and cobalt are in the high-spin configuration. The magnetic moments determined from the spin configuration are:

$$\mu(Fe^{3+}) = 5\mu_B \qquad \mu(Co^{3+}) = 3\mu_B \tag{2.24}$$

2.2.2.2. Orbital quenching

In the 3*d* ions the *d*-orbitals are extended away from nucleus therefore the crystal field interaction is stronger than the spin-orbital interaction. Firstly, by not considering the spin-orbital interaction, the average magnetic moment associated with its orbital angular momentum is reduced to zero. This effect is known as the orbital quenching. It can be explained in this way: The crystal field is the non-uniform electric field, therefore angular momentum L_z is changing with time and the time average is $\langle L_Z \rangle = 0$.

Now by including the spin-orbital coupling as a small perturbation it can be shown that the orbital momentum is not completely quenched by using the second-order perturbation theory. This results in change of the *g*-factor that is not equal to the spin-only value of *2*.

2.2.2.3. Jahn-Teller effect

The degeneracy of the *d*-orbitals is removed only partially by the crystal field with the cubic symmetry (octahedral and tetrahedral environment). As was shown the *d*-orbitals are split into a doublet and a triplet. The H. A. Jahn and E. Teller demonstrated that systems with the degenerated states can not be stable therefore they undergo a geometric distortion to lower the energy. This breaking of the symmetry leads to the splitting of the *d*-orbitals. This effect is known as the Jahn-Teller effect (distortion) and is mostly seen in compounds with transition metals, typically in Cu^{2+} systems with d^9 configuration.
This distortion changes the symmetry of the crystal field from cubic to tetragonal. The splitting of the *d*-orbitals depends both on electron configuration and the environment.
Concretely, in the octahedral environment, the geometric distortion of the lattice is rather induced by the partially filled e_g orbitals (e.g. d^4, d^9 configuration) than by the t_{2g} orbitals. The e_g orbitals point along the x, y, z axis, therefore the distortion results in large energetic stabilisation. If the t_{2g} orbitals are partially filled, the Jahn-Teller distortion can also occur, however the effect is small and comparable with the effects of the spin-orbital coupling.

2.3. Magnetic nanoparticles

As the title suggests the magnetic nanoparticles have characteristic size of the order of nanometres. Due to their nano-size their physical properties are mostly very different from the bulk material. In this section, the superparamagnetic model of nanoparticles that assumes no interparticle interactions will be described. Afterwards the effects of interparticle interactions will be shown as they can not be ignored in many systems. Finally, surface effects in nanoparticles will be described. They play an important role because they cause the so-called spin canting.

2.3.1. Superparamagnetism

In the section 2.1.6.2. it was shown that formation of the magnetic domains is due to balance between the dipolar energy and the exchange energy (as the domain wall energy). As the size of particles reduces, the surface energy becomes more costly and there exists a critical size at which it is energetically favorable for a particle to become a single-domain. The first theoretical model about energetic stability of a single-domain particle was proposed by Ch. Kittel in 1946 [18].

To study the magnetic properties of single-domain particles within the so-called superparamagnetic theory the following assumptions are needed. At first, interactions between particles are neglected (the particles are very well separated). Furthermore, the magnetic moments within the particle rotate coherently, i.e. the net magnetic moment can be represented by a single classical vector. Now by considering the single-domain magnetic particle in a magnetic field H that is applied at an angle α to the easy axis of its uniaxial anisotropy, the relation for its energy can be written as [19]:

$$E = KV \sin^2 \theta - \mu H \cos(\alpha - \theta) \qquad (2.25)$$

where θ is the angle between the magnetic moment of the particle and its easy axis (see Figure 2.13a)).

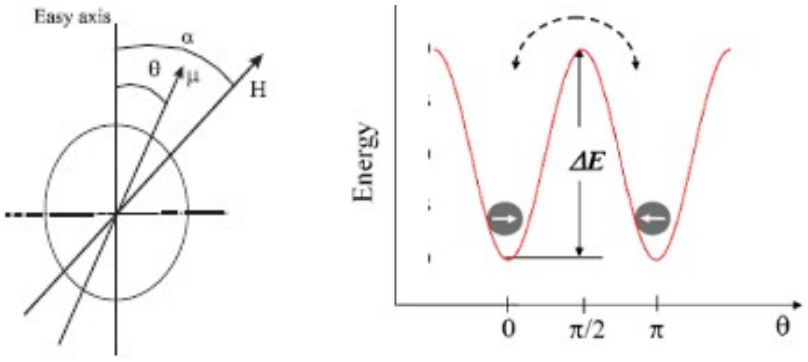

Figure 2.13: a) Definition of the axis system for a fine particle [19]. b) Dependence of anisotropy energy on angle θ. It is obvious that the energy is minimized when $\theta = 0$ *or* π, and the energy $\Delta E = KV$ is needed to flip the magnetization from one direction to another [20].

The first term in (2.25) is the anisotropy energy, where K is the so-called effective anisotropy constant (consists of intrinsic, shape and surface contributions) and V is the volume of the particle.

In absence of the applied field (second term in (2.25) vanishes), the magnetic moment of the particle prefers to line up along $\theta = 0$ or $\theta = \pi$. It is obvious that the energy barrier that separates both equilibrium states is equal to the KV. This energy is needed to flip the magnetic moment of particle from $\theta = 0$ to π. For small particles the energy barrier KV is comparable with thermal fluctuations k_BT. If $k_BT >> KV$ the system behaves like a paramagnet, but the magnetic moments are those of individual particles [13]. The system is therefore called a superparamagnet. In the superparamagnetic state the magnetization of the whole material is zero without applied field due to the thermal fluctuations of the magnetic moments – the coercivity and remanent magnetization is zero, on the other hand the saturation magnetization is higher than in paramagnetic material. The relaxation time of the particle moment is a function of the energy barrier and temperature:

$$\tau = \tau_0 \exp\left(\frac{KV}{k_BT}\right) \tag{2.26}$$

where τ_0 is typically 10^{-9}s. With decreasing temperature the fluctuations slow down and below the so-called blocking temperature, T_B the relaxation is very slowly and one can observe quasistatic properties as in ordered magnetic system. The particles are called to be in the blocked state – magnetic moments fluctuate only in the vicinity of the easy axis. Therefore the coercivity and remanent magnetization is non-zero.

It is important to note that the observed magnetic properties (as the blocking temperature) depend on characteristic measuring time of the employed experimental technique. This measuring time varies from 10^{-2}s (typical for a.c. susceptibility) over 10^{-7}s (Mössbauer spectroscopy) to 10^{-12}s (inelastic neutron scattering) [19].

From (2.26) the blocking temperature, T_B for a certain measuring and relaxation time can be calculated as [19]:

$$T_B \approx \frac{KV_0}{k_B} \tag{2.27}$$

It is obvious that with the increasing particle size (increasing particle volume, V_0) the blocking temperature increases too. Moreover if the sample has a distribution of particle size, there will be an insignificant "transition". The bigger particles become superparamagnetic at higher temperatures.

For particles in the superparamagnetic regime ($k_BT >> KV$) where the anisotropy energy is negligible, the macroscopic magnetization is given by:

$$\frac{M}{M_S} = L\left(\frac{\mu H}{k_BT}\right) \tag{2.28}$$

where $L(x) = \coth(x) - \frac{1}{x}$ is the well-known Langevin function. However this relation is usually not exact in real systems due to the non-negligible interparticle interactions, surface anisotropy and existence of distribution of the particle size.
In case of small fields or high temperature, the Langevin function can be expanded as a power series and the initial susceptibility in superparamagnetic regime undergoes the well-known Curie law (see equation (2.13)).

2.3.2. Interparticle interactions

In the previos section the magnetic properties via the superparamagnetic model that neglects interactions among the particles were described. However, this model is consistent only in well-diluted systems therefore in a real system of nanoparticles these interactions can not be ignored. There are several types of the interactions among nanoparticles: dipole-dipole interactions that always exist and have anisotropic character, exchange interaction through the surface of nanoparticles that are in close contact, superexchange via insulating matrix or RKKY that is presented when the matrix is metallic.
The first attempt to describe the interaction effects was the so-called ISP (interacting superparamagnetic model) made by Shtrikmann and Wohlfarth that is based on a sort of a mean field caused by the presence of neighboring magnetic nanoparticles. In this model the Vogel-Fulcher law for relaxation time in weak interaction limit was predicted [21]:

$$\tau = \tau_0 \exp\left(\frac{KV}{k_B (T_B - T_0)} \right) \tag{2.29}$$

where T_0 is an additional parameter which accounts for the interaction effects.
More general approach is done by Dormann-Bessais-Fiorani model [22] that describes the effect of interactions by the change of the energy barrier affecting individual particles. The interparticle interaction leads to increase of the effective anisotropy constant that leads to increase of the blocking temperature with the strength of the dipolar interactions. This is valid for strong interactions. Another model developed by Morup [23] suggests the opposite behavior of the blocking temperature in case of weak interactions. It is obvious that the role of interparticle interaction on magnetic properties is very complicated.
The collective state that occurs below the blocking temperature is usually described by the spin glass-like behavior. Spin glasses are usually defined as random, interacting systems with a cooperative freezing of spins at a defined freezing temperature, T_f. At high temperature the spins are independent, but with the decrease of temperature the spins build up into locally correlated units, known as clusters. With reaching the so-called freezing temperature, T_f the fluctuations of spins rapidly slow down and the system finds one of its many ground states and freezes. However, the system does not show long-range magnetic order [13].

2.3.3. Surface effects

The surface effects become very important in nanoparticles as by decreasing the particle size the fraction of atoms that lies on the surface increases. The atoms at the surface have lower coordination numbers that results from breaking of symmetry of the lattice at the surface. Moreover, the exchange bonds are broken that affects the magnetic behavior of the surface. This all leads to increase of the surface contribution to the anisotropy constant that can be at same order as the bulk value. For a spherical particle the relation for the effective anisotropy constant is given by:

$$K_{eff} = K_b + \frac{6}{d} K_s \tag{2.30}$$

where K_b is the bulk value, d the diameter of particles and K_s is the surface density of the surface anisotropy.

The surface effects affect the magnetic properties of such particles. The ideal superparamagnetic model where all spins point in the direction of the easy axis is not valid because there is a spin disorder and frustration at the surface. The spin structure of such nanoparticles can be well-described by the so-called core-shell model, that was firstly proposed by J. Coey in 1971 [24]. In the core-shell model, (see Figure 2.14) a nanoparticle consists of two parts: the magnetically ordered core, where all spins are aligned in direction of the easy axis, and the disordered shell of spins, where spins are inclined at some angle to their normal direction. This canting angle is not random but depends on the magnetic nearest neighbors of the canted spins. The magnetization of the surface layer is therefore smaller than in the core. As it was observed by Coey [24] in maghemite nanoparticles, the spin disorder lowers the value of the saturation magnetization.

The canting angle can be obtained from in-field Mössbauer spectroscopy as will be discussed later.

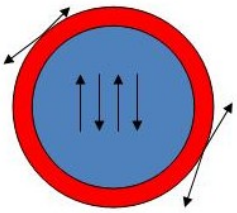

Figure 2.14: Core-shell model of nanoparticle.

2.3.4. Typical magnetic measurements of nanoparticles

The typical experiment probing magnetic behavior of the nanoparticles is the measurement of the magnetization dependence on temperature that is known as ZFC (zero field cooled) and FC (field cooled) curve. In the first step, the sample is cooled without applied field down to temperature much lower than the blocking temperature. Afterwards, small field (usually below 10 mT) is applied and the magnetization is

measured with increasing temperature. The obtained curve is called the ZFC. The same measurement is done only with the difference that the sample is cooled down with unchanged magnetic field – the FC curved is obtained. The typical curve is shown in Figure 2.15.

After cooling without an applied field the magnetic moments freeze in random orientation therefore the net magnetization is zero. With increasing temperature the magnetic moments can rotate near their easy axis that leads to increase of the net magnetization till the blocking temperature, T_B. Above this temperature the thermal fluctuations predominate, the sample is in superparamagnetic regime and the magnetization decreases like in paramagnet according to the Curie law.

In the case of field cooled measurement, the magnetic moments freeze in orientation near to the easy axis of magnetization. The magnetization decreases with rising temperature due to thermal fluctuations. In ideal superparamagnet, where the interparticle interactions are ignored, the net magnetization in the FC curve does not reach the saturation value and follows the Curie law.

Two characteristic temperatures can be obtained from this measurement - the blocking temperature, T_B as the temperature of the maximum of the ZFC curve and so-called irreversibility temperature, T_{irr} that is the temperature where the ZFC curves departs from the FC curve. In the ideal case (no particle size distribution and no interparticle interactions), the ZFC curves departs from the FC curve at the maximum of the ZFC curve.

Another typical magnetic measurement is the magnetization dependence on applied field known as the hysteresis loop that was briefly described in section 2.1.6.3. From this measurement the coercivity, saturation magnetization and remanent magnetization can be obtained. The magnetization isotherms above the T_B can be analysed in order to obtain particle size distribution as the macroscopic magnetization is given by the weighted sum of the Langevin functions:

$$M(H,T) = \int_0^\infty \mu L\left(\frac{\mu H}{k_B T}\right) f(\mu) d\mu \tag{2.31}$$

where $f(\mu)$ is the magnetic moment distribution, often derived as the log-normal distribution.

For studying the magnetization dynamics of samples, the a.c. susceptibility measurement is performed. From this measurement the relaxation time and the effective anisotropy constant can be determined.

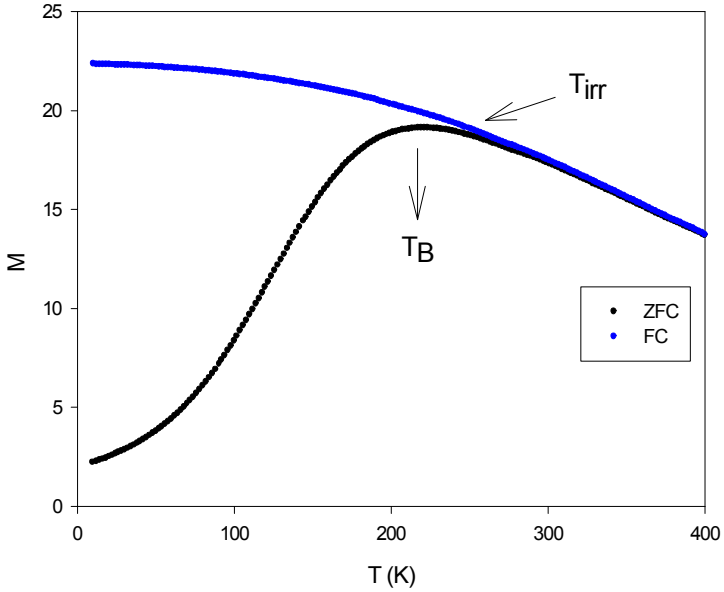

Figure 2.15: The typical ZFC-FC curve. The maximum of the ZFC curve corresponds to the blocking temperature, and the bifurcation point of the ZFC and the FC curve corresponds to the irreversibility temperature.

2.4. Characterization of our studied materials

In this section the basic characteristics of spinel ferrites will be described as their potential application followed by the general description of the crystal structure and magnetism of ferrites. Then the attention will be focused on $CoFe_2O_4$ and controlling of its magnetic properties by doping with rare earth elements. Afterwards, the brief description of the structure of other compounds that was formed in studied samples will be done: α-Fe_2O_3, La_2O_3, SiO_2, $LaFeO_3$ and Co_2SiO_4.

2.4.1. Spinels ferrite

2.4.1.1. Basic characteristic

Iron oxides are one of the most occurring materials in the nature, they are components of many rocks and soils, they take part in biochemical process etc. One of the large groups of these materials is the spinel ferrite materials. Their magnetic properties can be affected by the methods of preparation.

The spinel ferrites cover wide range of magnetic and electronic properties. In the bulk form they can be half-metallic (as Fe_3O_4), insulating ($NiFe_2O_4$), ferrimagnetic or antiferromagnetic ($ZnFe_2O_4$). However, the physical properties of the magnetic nanoparticles are very different from the bulk system due to its small size that brings other physical contributions (as the surface effects). As their magnetic properties strongly depend on the particle size, they can be utilized in variety of fields as in biomedicine, for example magnetite, Fe_3O_4 is a good candidate due to its non-toxicity and high chemical stability [25], another candidate is $CoFe_2O_4$ because of its high coercivity [5].

Most of the ferrite spinels are supposed to be utilized as gas sensors, as they show a significant change of the conductivity when they are exposed to a different gas atmosphere, e.g. $NiFe_2O_4$ nanoparticles are sensitive to chlorine gas [26], or doped with Ca, Mn to aceton [27], $MgFe_2O_4$ is sensitive to ethanol gas, $ZnFe_2O_4$ to sulphan H_2S [26] etc.

2.4.1.2. Crystal structure

The spinel structure is named after the compound spinel - $MgAl_2O_4$. The general formula can be written as $A^{2+}B^{3+}{}_2O^{2-}{}_4$, where A, B are cations of metals. The ideal spinel structure consists of the cubic close packing of the oxygen ions with the interstitial sites partially filled with the metal ions. The structure is face-centered cubic (space group Fd-3m). In the unit cell there are 32 atoms of oxygen. The metal ions lie in the tetrahedral (usually marked as “A”) and the octahedral sites (“B”), respectively (see Figure 2.16). The tetrahedral-interstitial ions are in the centre of tetrahedra that is formed by 4 oxygen atoms. The octahedral interstice lies in the centre of octahedra that

is created by 6 oxygen atoms (see Figure 2.17). In the unit cell there are 8 tetrahedral sites and 16 octahedral sites [28]. The occupation of the tetrahedral and octahedral sites is highly dependent on the kind of metal ion and its charge factor, because the tetrahedral intersticies are smaller than the octahedral. There are two boundary possibilities, how to occupy these sites:

a) Normal structure

In this type of structure, 8 A^{2+} ions per unit cell occupy the tetrahedral sites and 16 B^{3+} ions occupy the octahedral sites. The example of this structure is $MnFe_2O_4$.

b) Inverse structure

It represents the inverse distribution of cations. Hence, the tetrahedral sites are occupied by B^{3+} ions and the octahedral sites are occupied by A^{2+} and B^{3+} ions that are randomly distributed within the site. The most known representative is the magnetite, Fe_3O_4 (can be written as $(Fe^{3+})[Fe^{3+}Fe^{2+}]O_4$).

Most of the materials do not belong exactly to one of these groups but possess some degree of inversion that mostly depends on the condition of preparation [3].

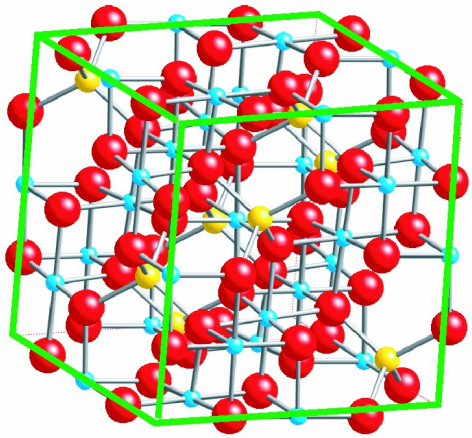

Figure 2.16: The image of the spinel crystal structure – red balls are atoms of oxygen, yellow balls are the tetrahedral sites and blue balls are the octahedral sites. In the case of cobalt ferrite, yellow balls are Fe^{3+} ions, and blue balls are Co^{2+} and Fe^{3+}.

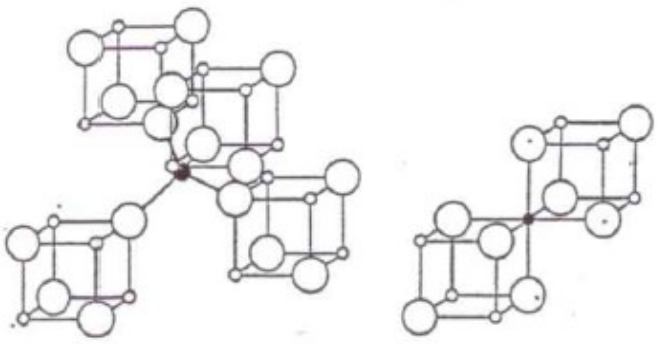

Figure 2.17: The image of the tetrahedral site (left plot) and the octahedral site (right plot). The black small balls are the ion positions, the white large balls are oxygen atoms [28].

2.4.1.3. Magnetic properties

The spinel ferrites are ferrimagnetic. This can be easily explained by the Néel theory of sublattices (section 2.1.7.). In the spinel structure there are two possible positions (sublattices) for magnetic ions – the tetrahedral (A) and octahedral (B) sites. The magnetic moments in A, respectively B sites are aligned parallel with respect to each other, because the exchange interaction is positive. On the other hand, the exchange interaction between A and B-sites is negative, therefore the magnetic moments between A and B-sites are oriented antiparallel (see Figure 2.18). The A-A and B-B interactions are weak with respect to the A-B interactions and do not contribute to the simple Néel theory. Therefore the net magnetic moment is given by the difference of those of the A and B sublattices and as there are twice many B-sites than A-sites, it leads to ferrimagnetic behavior in spinel structures [29]. The choice of the metal cation and the distribution of ions between the A and B-sites therefore tune the magnetic properties of the spinel system.

In ideal inverse ferrite spinel structure, half of Fe^{3+} ions are situated in A-sites and the other half in B-sites, hence they compensate each other. The net magnetic moment is then created only by the divalent metal ions Me^{2+}.

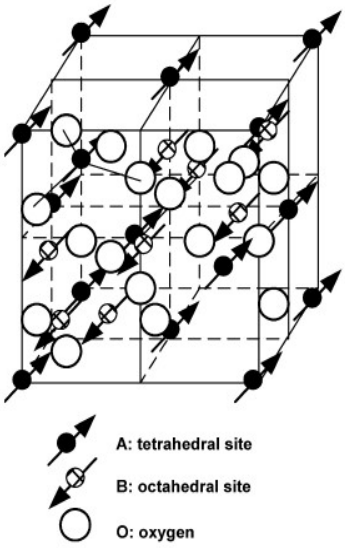

Figure 2.18: Schema of ferrimagnetic ordering in spinel structure [29].

2.4.2. Cobalt ferrite $CoFe_2O_4$

2.4.2.1. Crystal structure

The cobalt ferrite is mostly said to be a representative of the inverse type of spinel structure, but in fact it is not completely inverse [3] and the degree of inversion depends on condition of preparation (e.g. final heat treatment).

As it was mentioned before the crystal structure is cubic with the space group Fd-3m and lattice parameter $a = 8.4$ Å. The fraction coordinates of ions in the unit cell are

summarized in Table 2.1 [30]. The Co^{2+} and Fe^{3+} ions occupy the special sites, while the O^{2-} occupies the general positions. The positions of the O^{2-} ions that are shown in Table 2.1 are known from experiments and they differ from sample to sample.

Table 2.1: Fraction coordinates of ions in the $CoFe_2O_4$:

ion	x/a	y/b	z/c
Co^{2+}	0.125	0.125	0.125
Fe^{3+}	0.5	0.5	0.5
O^{2-}	0.23	0.23	0.23

2.4.2.2. Magnetic properties

The $CoFe_2O_4$ nanoparticles exhibit high coercivity (up to 2 T) in comparison to other ferrite spinels due to presence of the Co^{2+} ions. One of the contributions to magnitude of the anisotropy constant, K is the strength of the spin-orbital interaction. The Co^{2+} ions are presented in the octahedral environment in spinels with electronic configuration $3d^7$. The cubic symmetry of this environment is lowered to the trigonal symmetry resulting in splitting of the triplet-degenerated energy states. Therefore the Co^{2+} ions posses strong spin-orbital coupling that greatly contributes to the anisotropy constant [31].

2.4.2.3. Influence of doping RE ions on the properties of $CoFe_2O_4$

From the previos section it is obvious that doping of small amount of different ion can lead to change in the crystal structure and magnetic behavior of spinels. There exists a basic correlation between the lattice parameters and the anion-cation distance for a particular site, the general equation is given by [9]:

$$a = 2.0995R_{tetra} + \sqrt{5.8182R^2{}_{octa} - 1.4107R^2{}_{tetra}} \qquad (2.32)$$

where R_{tetra} and R_{octa} measure exactly the average value of the anion-cation distance on the tetrahedral and octahedral sites, respectively. For instance, the RE^{3+} ion with relatively large ionic radii (as for La^{3+} - $r_{La3+} = 1.032$ Å) preferably goes to the octahedral sites, which leads to increase of the lattice parameter (increase of R_{octa} in (2.32)). The ionic radius of Co^{2+} ions ($r_{Co2+} = 0.745$ Å) are larger than ionic radius of Fe^{3+} ions ($r_{Fe3+} = 0.645$ Å) in the octahedral environment. The group of L. B. Tahar [9] observed that the entrance of RE^{3+} ion led to partial migration of the Co^{2+} ions from B to A-sites accompanied by an opposite transfer of an equivalent number of the Fe^{3+} ions to relax the induced strain. This re-arrangement of the cation distribution in the spinel structure affects the resulting lattice parameter and also the magnetic properties.

The RE elements posses a variety of magnetic properties, they can be isotropic or anisotropic due to the number of electrons in the *f*-orbitals and therefore should contribute to the anisotropy energy of $CoFe_2O_4$.

2.4.3. Other oxide phases

2.4.3.1. Hematite – α-Fe_2O_3

Crystal structure

Hematite crystallizes in rhombohedral (hexagonal) system with a space group R-3c. The most known representative of this group is corundum, α-Al_2O_3. This structure consists of the hexagonally close-packed planes of oxygens with Fe^{3+} ions filling two-thirds of the octahedral intersticies. Each Fe^{3+} is surrounded by six oxygen atoms, which are not at the corners of a regular octahedron. Three of these oxygen atoms are a few percent nearer to the Fe^{3+} than the other three. Each oxygen atom is surrounded by four Fe^{3+} ions, two of them are closer than the other two [32]. The lattice parameters and fraction coordinates are presented in Table 2.2 and Table 2.3, respectively [30], and the crystal structure is shown in Figure 2.19.

Table 2.2: Lattice parameters of α-Fe_2O_3:

Lattice parameters	*a* (Å)	*b* (Å)	*c* (Å)	α (°)	β (°)	γ (°)
	5.032	5.032	13.737	90	90	120

Table 2.3: Fraction coordinates for ions in the α-Fe_2O_3:

ion	x/a	y/b	z/c
Fe^{3+}	0.0	0.0	0.35
O^{2-}	0.3	0.0	0.25

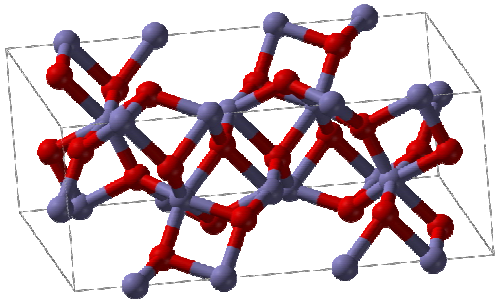

Figure 2.19: The crystal structure of hematite. The blue balls are the Fe^{3+} ions and red balls are the O^{2-} ions [33].

Magnetic properties

Hematite is antiferromagnetic below the so-called Morin transition at 250 K, above this temperature it shows the so-called weak ferromagnetism (canted antiferromagnetic) up to the Néel temperature at 950 K.

Below 250 K, the magnetic moments of Fe^{3+} are aligned parallel along the crystal axis [111]. Within this axis the pairs of spins are orientated parallel with respect to each other and antiparallel with respect to other pair of spin. Above the Morin transition, the

spins are lying in plane perpendicular to the crystal axis [111] and they are inclined at some small angle with respect to each other [16].

2.4.3.2. Lanthanum tri-oxide La_2O_3

Lanthanum tri-oxide belongs to a group of sesquioxides that crystallizes in three types of structures A (hexagonal), B (monoclinic) and C (cubic). Lanthanum tri-oxide La_2O_3 mostly exists in the A-type of structure at wide range of temperature (250°C to 2100°C), at low temperature it can converted to the metastable cubic C-type. The A-type crystallizes in the hexagonal close-packed structure with the space group P-3m1. Each La^{3+} is bonded to seven oxygens where four oxygens are closer than the other three [34]. The lattice parameters of the A-type structure that was found in our samples are summarized in Table 2.4.

Table 2.4 Lattice parameters of A-La_2O_3:

Lattice parameters	*a* (Å)	*b* (Å)	*c* (Å)	α (°)	β (°)	γ (°)
	3.94	3.94	6.12	90	90	120

2.4.3.3. Silicon dioxide SiO_2

Silicon dioxide is mostly found in nature as a sand or quartz. There are three crystalline forms of silica – quartz, tridymite and cristobalite and two variation of each of these known as low and high temperature structure. The transition temperature between the low and high structure is different for each crystalline form. In all these configurations each Si atom is presented in the tetrahedral coordination with four oxygen ions at corners of tetrahedra and each of these oxygen atoms must be bonded to two Si atoms that are also at corners of tetrahedra [35]. The crystalline forms vary from each other by the length of silicon-oxygen bonds, and angles between Si-O-Si from 140°to 180°.

In part of studied samples the α-quartz crystalline form was observed. α-Quartz crystallizes in rhombohedral (trigonal) structure with the space group $P3_221$. The lattice parameters are presented in Table 2.5 and the image of the crystal structure is shown in Figure 2.20.

Table 2.5: Lattice parameters of α-SiO_2:

Lattice parameters	*a* (Å)	*b* (Å)	*c* (Å)	α (°)	β (°)	γ (°)
	4.89	4.89	5.375	90	90	120

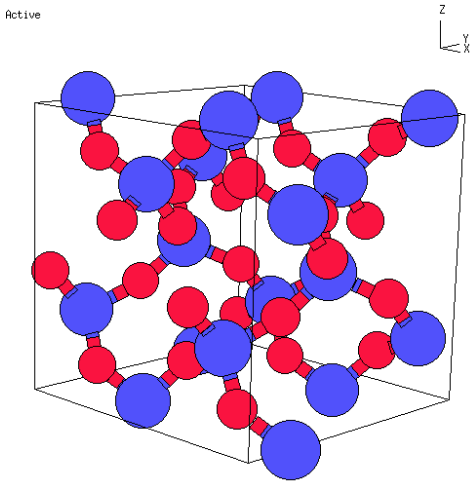

Figure 2.20: The crystal structure of α-quartz. Blue balls are atoms of silicon, red balls are atoms of oxygen [36].

2.4.3.4. Iron Lanthanum oxide $LaFeO_3$

Iron lanthanum oxide (sometimes known as lanthanum orthoferrite) is an antiferromagnetic oxide that crystallizes in the structure derived from the well-known orthorhombic perovskite-structure named after the compound perovskite ($CaTiO_3$). The space group is Pnma. The perovskite structure can be approximately shown as the cubic lattice, where the La^{3+} ions are in the corners of lattice, the Fe^{3+} ions in the centre and the O^{2-} ions are at face centered positions [37]. The lattice parameters are summarized in Table 2.6 and the unit cell is imaged in Figure 2.21.

Table 2.6: Lattice parameters of $LaFeO_3$:

Lattice parameters	*a* (Å)	*b* (Å)	*c* (Å)	α (°)	β (°)	γ (°)
	5.56	7.85	5.55	90	90	90

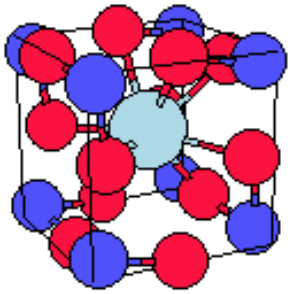

Figure 2.21: Image of the perovskite structure, where the grey ball is atom of iron, blue balls are atoms of lanthanum and red balls are atoms of oxygen [36].

2.4.3.5. Cobalt silicate Co_2SiO_4

Cobalt silicate is isomorphous with the structure of mineral olivine that belongs to the hexagonal close-packed oxygen of spinel-type structure described above. One eighth of

the tetrahedral sites is occupied by the Si^{4+} ions and half of the octahedral sites is occupied by the Co^{2+} ions [38]. The cubic lattice parameter *a* is *8.14 Å*.

3. Experimental details

3.1. Preparation

Two different methods of preparation were used – the sol-gel method and the microemulsion route, respectively. These methods differ in the sample constitution – the nanoparticles prepared by the sol-gel method are embedded in silica matrix whereas by the microemulsion route the nanoparticles are matrix-free. The samples were prepared by P. Holec (Institute of Inorganic Chemistry, Czech Academy of Sciences).

3.1.1. Sol-gel method

The sol-gel method is one of the most widely used preparation techniques of nanoparticles and nanocomposites. By this method a homogenous distribution of crystalline particles embedded in silica matrix can be prepared. It involves production of colloidal suspensions ("sols"), which are subsequently converted to a viscous gel. Colloids are suspensions of particles of linear dimension between 1 nm to 1 μm. The chemical reactions that describe these steps are hydrolysis and condensation. The crystalline nanoparticles are afterwards crystallized in silica matrix by final heat treatment. The advantage of this method is that by changing the reaction conditions as pH, concentration of catalyst, temperature, time of reaction, and by final annealing temperature the properties of the resulting product can be tuned. For more information, see [39].
The samples prepared by the sol-gel method are summarized in Table 3.1. All prepared samples were finally annealed at different temperatures (the marks in the Table 3.1 are shown as an example for the samples annealed at 800°C, for the other temperatures the end of the marks would change correspondingly).

Table 3.1: The list of samples prepared by the sol-gel method:

Annealing temperature	Chemical composition	Mark
800°C, 900°C, 1000°C, 1100°C	$La_{0.05}Co_{0.95}Fe_2O_4 * 5SiO_2$	La005_Co095_800
	$La_{0.1}Co_{0.9}Fe_2O_4 * 5SiO_2$	La01_Co09_800
	$La_{0.2}Co_{0.8}Fe_2O_4 * 5SiO_2$	La02_Co08_800
	$La_{0.3}Co_{0.7}Fe_2O_4 * 5SiO_2$	La03_Co07_800
	$La_{0.4}Co_{0.6}Fe_2O_4 * 5SiO_2$	La04_Co06_800
	$La_{0.5}Co_{0.5}Fe_2O_4 * 5SiO_2$	La05_Co05_800
800°C	$CoLa_{0.01}Fe_{1.99}O_4 * 5SiO_2$	La001_Fe199_800
	$CoLa_{0.05}Fe_{1.95}O_4 * 5SiO_2$	La005_Fe195_800
	$CoLa_{0.1}Fe_{1.9}O_4 * 5SiO_2$	La01_Fe19_800
	$CoLa_{0.2}Fe_{1.8}O_4 * 5SiO_2$	La02_Fe18_800

3.1.2. Microemulsion route

The microemulsion route is suitable for synthesizing uniform-size nanoparticles. If the emulsion consists of certain ratio of water, oil, surfactant and co-surfactant, a micelle (or inverse micelle) is created. As the micelle is small it performs a Brownian motion, even at room temperature, that leads to lots of collisions between two micelles. These two micelles create a dimer for a short time (~100 ns). During this lifetime of the dimer, two reverse micelles may exchange the contents of their aqueous cores before uncoupling. If the precursors are introduced into micelles, the centre of micelle serves as a nanoreactor. Afterwards the reaction products are removed from the emulsion and they are usually annealed to obtain final products. The size and shape of nanoparticles can be controlled by the radius and shape of micelles. More information can be found in [40].
The samples prepared by the microemulsion route are summarized in Table 3.2.

Table 3.2: List of samples prepared by the microemulsion route:

Annealing temperature	Chemical composition	Mark
550°C	$CoFe_2O_4$	Co550
750°C	$CoFe_2O_4$	Co750
950°C	$CoFe_2O_4$	Co950
500°C	$La_{0.1}Co_{0.9}Fe_2O_4$	La01
500°C	$La_{0.2}Co_{0.8}Fe_2O_4$	La02
500°C	$CoLa_{0.1}Fe_{1.9}O_4$	La03

3.1.3. Leaching of SiO_2 matrix

The goal of the leaching procedure is to remove the SiO_2 matrix to study the influence of the matrix on magnetic properties of the nanoparticles. The nanoparticles were mixed with 1M NaOH. The reaction mixture was then heated at 80°C for five hours. After that, the nanoparticles were collected by the centrifugation and repeatedly washed with distilled water until the pH was neutral. The leaching procedure was done for the sample La005_Co095_800.

3.2. Powder X-ray diffraction

The powder X-ray diffraction is a convenient method for determination of the crystal structure of the sample. The diffracted intensity of the interfering waves as a function of the diffraction angle is observed. The condition of the constructive interference can be expressed by the well-known Bragg's law:

$$2d_{hkl}\sin\Theta = \lambda \tag{3.1}$$

where d_{hkl} is the spacing between the planes in the crystal lattice, Θ is the angle between the incident X-ray beam and the scattering planes and λ is the wavelength of the X-rays. Each material has its unique X-ray powder pattern hence this method could be used for identification of unknown samples. The so-called phase analysis and also the information about the crystal lattice can be determined from the positions of the peaks. The microstructural effects as defects (dislocations etc.), micro-strains and small crystallite size affect the FWHM (full width at half maximum) and shape.

Using the known lattice parameters and fraction coordinates, the data can be fitted by the Rietveld method to obtain the exacts crystallographic parameters of the sample. The Rietveld analysis consists of refining the crystal structure by minimizing the weighted squared difference s_y between the observed y_i^{exp} and the calculated pattern y_i^{calc}[41]:

$$s_y = \sum_i w_i \left(y_i^{\exp} - \frac{1}{c} y_i^{calc} \right)^2 \tag{3.2}$$

where w_i is the statistical weight and c is the scale factor applied to y_i^{exp}. All structural parameters could not be refined at the same time – a typical sequence of refinement of a crystal structure is the following:

- scale factor,
- background,
- lattice parameters,
- FWHM of peaks,
- fraction coordinates,
- Debye-Waller factor or individual isotropic thermal parameters,
- occupancies,
- microstructural parameters: crystallite size and strain effects.

The quality of agreement between the observed and calculated profiles is measured by a set of reliability factors. There can be calculated several of those, the most presented are the Bragg factor, R_B and the crystallographic factor, R_F [41]:

$$R_B = 100 \frac{\sum_h \left| {}'I_{obs,h}{}' - I_{calc,h} \right|}{\sum_h \left| {}'I_{obs,h}{}' \right|} \tag{3.3},$$

$$R_F = 100 \frac{\sum_h \left| {}'F_{obs,h}{}' - F_{calc,h} \right|}{\sum_h \left| {}'F_{obs,h}{}' \right|} \tag{3.4}$$

where '$I_{obs,h}$' is the observed integrated intensity that contribute to the reflection h, $I_{calc,h}$ is the calculated intensity, '$F_{obs,h}$', $F_{calc,h}$ are the structural factors with the same meaning of indices.

The Rietveld procedure is implemented in the program Fullprof. More information about this program can be found in [41].

3.2.1. Determination of particle size

The particle size affects the FWHM of the diffraction peaks. The experimental profile is a convolution of the instrumental profile and the physical profile. There are two ways how to determine the instrumental profile. First by the mathematical calculation where the resulting instrumental function is computed as convolution of contributions from the different parts of the experimental setup. Second by measuring of a standard sample. In the ideal case the standard needs to be of the same material as investigated and with no own physical broadening. In reality the standard possesses physical broadening and it is usually a different material, the most used materials are lanthanum hexaborite and silicon [42].

In general both the instrumental and physical profile are described by the Voigt function that is convolution of Lorentzian and Gaussian:

$$V(x) = L(x) \otimes G(x) = \int_{-\infty}^{\infty} L(x-u)G(u)du \tag{3.5}$$

where $L(x)$ and $G(x)$ have different FWHM H_L, H_G respectively.

$$G(x) = a_G \exp(-b_G x^2) \tag{3.6}$$

$$L(x) = \frac{a_L}{1 + b_L x^2} \tag{3.7}$$

where a_G, b_G, a_L, b_L are constants that depend on FWHM of the peak. The precisely fitting procedure by the Voigt function is not so easy, therefore the pseudo-Voigt function is used within the program Fullprof as an approximation. It is a linear combination of Lorentzian and Gaussian.

To obtain the instrumental broadening of peaks the standard sample LaB_6 was measured at first. By fitting this pattern with the pseudo-Voigt function, the parameters H_L, H_G and positions of peaks were determined and then used as a known resolution function.

The volume-averaged apparent size of the crystallites in the direction normal to the scattering planes can be calculated from the Scherrer formula [43]:

$$d = \frac{\lambda}{\beta \cos\Theta} \tag{3.8}$$

where $\beta = \frac{A}{I_0}$ is the integral breadth (A is the space under the peak and I_0 is the maximum of the intensity).
The X-ray data were collected using the Bruker diffractometer AXS GmbH with the Cu-K_α beam with monochromator. The X-ray diffraction patterns were collected in the 2Θ range: 10° - 100° with a step of 0.04° for all samples.

3.3. Mössbauer spectroscopy

The Mössbauer spectroscopy is one of the excellent techniques for studying chemical, structural and magnetic properties of materials. This method is based on recoilless γ-ray emission and absorption of nuclei that is named Mössbauer effect after its discoverer Rudolph Mössbauer. He observed this effect in 1957 and received the Nobel Prize in Physics in 1961 for his pioneer work. For more information, see references [44-45] that were used.

3.3.1. Mössbauer effect

Nuclei in atoms undergo a variety of energy level transitions, associated with emission or absorption of a γ-ray. In a free atom the energy of the emitted γ-ray does not correspond to the energy of the nuclear transition but it is lower by the recoil energy of the emitting atom due to the conservation of momentum and conversely the energy of absorbed γ-ray needs to be greater by this recoil energy. However if the atom is within a solid matrix, the effective mass is much greater and that makes the recoil energy very small and thus negligible - the so-called resonance occurs. As the nuclear levels are influenced by their surroundings, the information about the local structure (electronic and magnetic) of atoms can be determined from the resonance spectra of γ-ray.
The small variation in the γ-rays energy is done by use of the Doppler effect and the dependence of the absorbance of γ-rays on velocity is measured. The suitable atom for Mössbauer spectroscopy is isotope of iron ^{57}Fe, which natural abundance is 2.2% only. By this method the structural and magnetic properties of materials containing atoms of iron can be investigated. There are three main ways, how the energy levels in the absorbing nuclei can be modified by their environment that will be now discussed in details: the isomer shift, the quadrupole splitting and the magnetic splitting.

3.3.2. Isomer shift

The isomer shift arises from the Coulomb interaction between nucleus and *s*-electrons of atoms, which have non-zero density in nucleus. Any difference in *s*-electrons environment between the source and the absorber (sample) produces a shift in the resonance energy of the transition. From the isomer shift the valence state of iron atom

can be determined - Fe^{2+} has higher isomer shift (0.8 - 1.2 $mm.s^{-1}$) than Fe^{3+} (0.2 - 0.4 $mm.s^{-1}$) due to lower density of *s*-electrons at nucleus.

3.3.3. Quadrupole splitting

The nuclei with $I > 1/2$ (I is the total angular momentum) exhibit an electric quadrupole moment, which arises from a non-spherical distribution of the electric charge of the nucleus. In the presence of the asymmetrical electric field the nuclear energy levels are split. For the nuclei with $I = 3/2$ (as excited state of ^{57}Fe) the state splits into two substates. The Mössbauer spectrum is a doublet (see Figure 3.1).

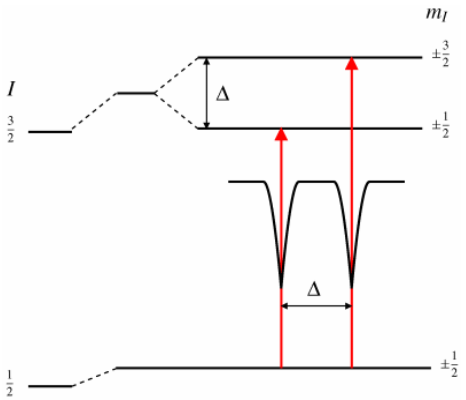

Figure 3.1: Quadrupole splitting of energetic levels of nuclei with $I = 3/2$ [45].

3.3.4. Magnetic splitting

The magnetic splitting is caused by interaction between nucleus and the local magnetic field or the external applied field. The source of the local magnetic field called hyperfine field, B_{hf} consists of three components: the Fermi contact term, the orbital term and the dipolar term. The most important is the Fermi contact term that is due to the spin densities of *s*-electrons at the nucleus. The orbital term is due to the orbital moment of electrons and the dipolar term is caused by interaction between the nuclear spin and the spin of its own electrons.

The magnetic field splits the nuclear levels into *(2I+1)* substates (this is shown in Figure 3.2. for nuclei with $I = 3/2$). Because allowed transitions are only those where m_I changes by 0 or +-1, the Mössbauer spectrum is a sextet.

The intensities of outer, middle and inner lines are related by:

$$3 : \frac{4\sin^2\theta}{1+\cos^2\theta} : 1 \qquad (3.9)$$

where θ is the angle between the γ-ray and z component of the nuclear angular momentum.

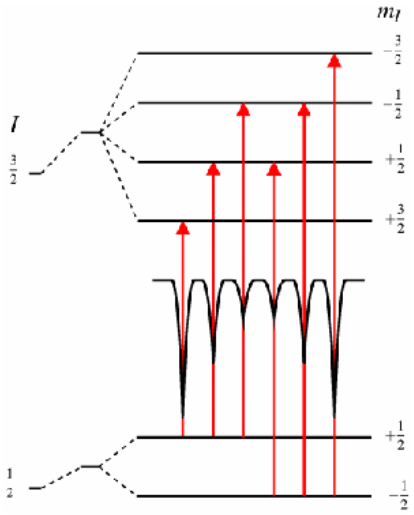

Figure 3.2: Magnetic splitting of the nuclear energy levels [45].

3.3.5. Measurements in magnetic field

The big advantage of in-field Mössbauer spectroscopy is the possibility of determination of the spatial orientation of magnetic sublattices with respect to the net magnetization. Moreover, the applied magnetic field B_{app} splits the overlapped sextets of spinel structure that simplifies the determination of the structure (and inversion degree).

In this measurement the nuclei experienced the resulting effective field:

$$\vec{B}_{eff} = \vec{B}_{app} + \vec{B}_{hf} \tag{3.10}$$

In Figure 3.3 two experimental setups of in-field measurement are shown. On the left plot the magnetic field is applied parallel to direction of the γ-ray. In this case the B_{eff} precesses around the direction of γ-ray that is equal to the direction of the B_{app} with the angle θ. The angle between the B_{eff} and the magnetization can be computed from the ratio of the intensities between the middle and inner line (relation (3.9)), respectively.

The right plot of Figure 3.3 demonstrates the experimental setup, where the magnetic field is applied perpendicular to the γ-rays. Now the situation is more complicated as the B_{eff} precceses around the B_{app} so the angle θ is not constant and varies.

Now let's show, how the spin canting angle can be determined in the perpendicular setup that was used for the studied samples. The spin canting angle is an angle between the hyperfine field and the applied field. This angle can be simply computed from the intensities of the middle and the inner lines. However this calculation is not exact due to the worse resolution than in the parallel case (the intensity ratio varies from 4:1 to 1.657:1, in contrast to parallel setup where the ratio varies from 4:1 to 0:1). Moreover, line intensities can be affected by the experimental errors namely by the so-called saturation. Therefore it is better to determine this angle by a different method. An alternative method for obtaining the canting angle α is to measure spectrum without an applied field, where the B_{hf} is determined and then do in-field measurement and get the

B_{eff}. The fitting procedure in the case of spinels can be done as follows: At first, due to the well resolved sextets, the in-field spectrum is fitted and the FWHM, area of peaks, isomer shift, quadrupole splitting and effective field B_{eff} are obtained. Except the B_{eff}, other parameters are not affected by the external field; therefore their values can be then used for fitting the spectra without applied field to obtain the B_{hf}. After that the spin canting angle α can be computed from the law of cosines (see triangle in Figure 3.3):

$$\cos\alpha = \frac{B_{eff}^{\ 2} - B_{app}^{\ 2} - B_{hf}^{\ 2}}{2B_{app}B_{hf}} \tag{3.11}$$

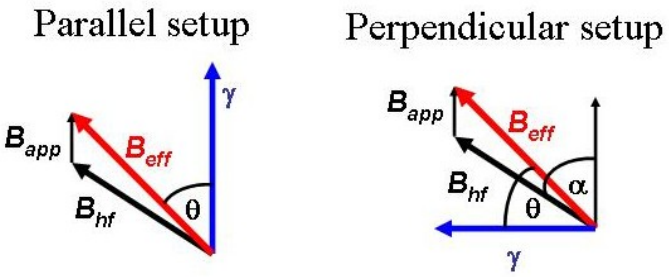

Figure 3.3: Diagram of the two experimental setups for measurements of in-field Mössbauer spectroscopy. On the left the B_{app} is applied parallel to orientation of the γ-ray, on the right the B_{app} is applied perpendicular to the γ-ray.

3.3.6. Typical Mössbauer spectra

3.3.6.1. $CoFe_2O_4$ nanoparticles

The typical Mössbauer spectra of transition from the superparamagnetic state to the blocked state of nanoparticles in the zero applied magnetic field are displayed in Figure 3.4 (left plot) [46]. At room temperature there is only a doublet indicating that nanoparticles are in the superparamagnetic regime (the relaxation time is shorter than the typical measuring time of the Mössbauer spectroscopy that is about 10^{-7}s). As the temperature decreases the magnetic sextet indicates the transition from the superparamagnetic state to the blocked state. The blocking temperature is usually determined when the 50% of the spectral area is magnetically split. In this case it is about 80 K.

The Figure 3.4 [47] also displays the typical spectra of the in-field measurement of $CoFe_2O_4$ nanoparticles. The external applied field causes the splitting of overlapped sextets that in the spinel structure belongs to the tetrahedral (A) and octahedral (B) sites, respectively. The applied field is added to the A-sites and subtracted from the B-sites. From the area of the well-splitted sextet the determination of the cation distribution over the tetrahedral and octahedral sites can be obtained.

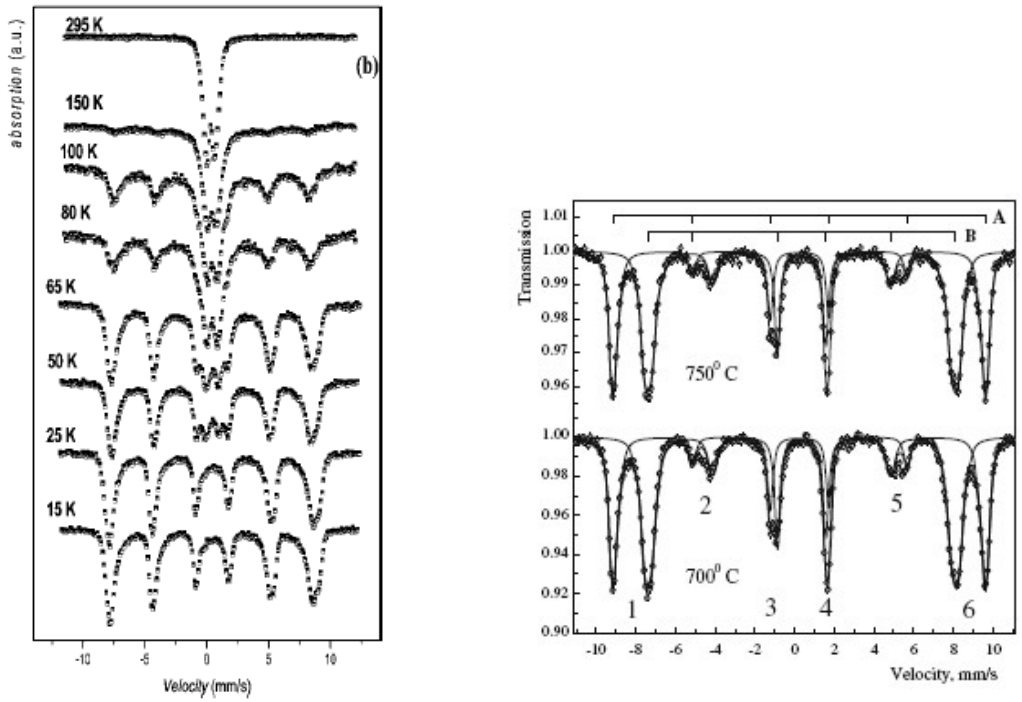

Figure 3.4: Typical Mössbauer spectra of $CoFe_2O_4$ nanoparticles. On the left side the variation of spectra with changing temperature in zero field is shown [46], on the right side the effect of the applied field is shown [47].

3.3.6.2. Hematite α-Fe_2O_3

The typical Mössbauer spectrum for a pure, bulk hematite measured at room temperature is shown in Figure 3.5. Till the so-called Morin transition (260 K) the hematite is antiferromagnetic, above the Morin transition up to its Néel temperature (960 K) it is weakly ferromagnetic therefore the Mössbauer spectrum shows the magnetic sextet at room temperature. The Morin temperature is well-defined only for pure, bulk hematite and in small particles or when the impurities are present the Morin transition can spread over a huge temperature range. As these two magnetic states of hematite have different Mössbauer parameters, the Morin transition can be well determined using Mössbauer spectroscopy. The Mössbauer parameters of hematite phases are summarized in Table 3.3 [48].

In comparison to the spinel structure, the only effect of the applied external field is a little broadening of lines. In a polycrystalline sample the angle between the applied field and the easy axis is distributed between 0 and π. By applying the external field the spin-flop transition occurs at a critical field that depends on the exchange and anisotropy energy. Below this critical value the signal is a superposition of all orientations of the B_{hf} [49-50].

Table 3.3: Mössbauer parameters of hematite:

compound	T (K)	δ (mm.s^{-1})	ΔE_q (mm.s^{-1})	B_{hf} (T)
Weakly ferromagnetic	300	0.38	-0.2	51.8
Antiferromagnetic	4.2	0.49	0.41	54.2
Weakly ferromagnetic	4.2	0.49	-0.2	53.5

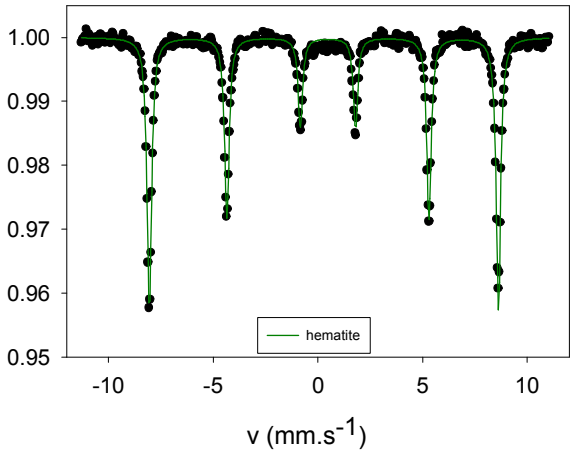

Figure 3.5: Typical spectrum for pure, bulk hematite measured at room temperature.

3.3.6.3. Details of measurement

The Mössbauer spectra measurement was done in the transmission mode with ^{57}Co diffused into a Rh matrix as the source moving with constant acceleration. The spectrometer (Wissel, Germany) was calibrated by means of a standard α–Fe foil and the isomer shift was expressed with respect to this standard at 293 K. The samples were also measured using cryostat (Janis Research) at the temperatures of 4.2 K equipped with superconducting magnet of 6 T. The fitting of the spectra was performed with the help of the NORMOS program. The list of the measured spectra is presented in Table 3.4.

Table 3.4: List of the measured spectra:

Sample	Temperature (K)	Field (T)
La005_Co095_800	Room temp. (300)	0
La005_Co095_900	300	0
	4.2	0
	4.2	6
La005_Co095_1000	300	0
La005_Co095_1100	300	0
La05_Co05_900	300	0
	4.2	0
	4.2	6
La005_Fe195_800	300	0
	4.2	0
	4.2	6
Co550	300	0
Co750	300	0
	4.2	0
	4.2	6
La01	300	0
La02	300	0
	4.2	0
	4.2	6
La03	300	0

3.4. Transmission electron microscopy (TEM)

The TEM operates on the same principles as the light microscope, but it uses the electron beam instead of light. Therefore higher resolution till 10^{-10}m can be obtained due to the lower wavelength of electrons. The beam of electrons passes through the ultrathin specimen and the interactions with the specimen creates an image that is afterwards magnified and focused on the fluorescent screen, where the image is observed.

The TEM images of selected samples were measured using TEM PHILIPS EM 201 80 kV with tungsten cathode.

3.5. Magnetic measurements

All magnetic measurements were done in Joint Laboratory for Magnetic Studies (JLMS). The SQUID magnetometer - MPMS7XL and the multifunctional device - PPMS14 were used (both from Quantum Design). In the former case, the device was used for measurements of the ZFC-FC curves, hysteresis loops and the a.c. susceptibility. In the latter case, the ZFC-FC curves in higher temperature were measured using the vibrating sample magnetometer system with oven. For more information about these devices see [51-52].

3.5.1. SQUID

SQUID (Super-conducting quantum interference device) is an extremely sensitive device that can be configured as a magnetometer to detect very small magnetic moments. The important is that it consists of two superconductors separated by thin insulating layers to form two parallel Josephson junctions.
Powder samples were placed in a gelatine capsule and fixed by glue to avoid orientation of particles of the sample to the field direction when being magnetized. The ZFC-FC curves were measured in temperature range of 10 – 400 K, the applied field was 10 mT for all samples summarized in Table 3.5. The magnetization dependence on the applied magnetic field (magnetization isotherms) were measured at different temperatures in the field range of -7 T to 7 T, the measured samples are summarized in Table 3.5. The coercivity H_c, saturation and remanent magnetization M_{7T}, M_r were obtained.

3.5.2. A.c. susceptibility

In contrast to the common magnetometry where the sample is magnetized by a constant magnetic field, in the a.c. magnetometry a small a.c. magnetic field is applied on the sample. As the induced sample moment is time-dependent, the measurement yields information about the magnetization dynamics. The temperature dependence of the a.c. susceptibility (the frequency ranges from 1 Hz – 1000 Hz) was measured in zero dc magnetic field for the La01 and La03 samples.

3.5.3. VSM (vibrating sample magnetometer)

In this type of magnetometry a sample vibrates sinusoidally and induces an electrical signal in a stationary pick-up coil. By the system with oven used in the PPMS, the measurements in the temperature range from 305 K to 1000 K, in magnetic field up to 14 T can be performed.
The samples were encapsulated into copper foil shield and then stick on the heater stick using alumina cement. The ZFC-FC curves were measured in the temperature range

from 310 K to 700 K under applied field of 10 mT and 50 mT. The measured samples were Co550, Co750, and Co950.

Table 3.5.: Details of measurement of hysteresis loops:

Sol-gel method		Microemulsion route	
sample	temperature	sample	temperature
La005_Co095_800	10 K, 400 K	Co550	10 K, 200 K, 400 K
La005_Co095_900	10 K, 200 K, 400 K	Co750	10 K, 200 K, 400 K
La005_Co095_1000	10 K, 100 K, 200 K, 400 K	Co950	10 K, 100 K, 200 K, 300 K, 400 K
La005_Co095_1100	10 K, 100 K, 200 K, 300 K, 400 K	La01	10 K, 400 K
La05_Co05_900	10 K, 400 K	La02	10 K, 200 K, 400 K
La001_Fe199_800	10 K, 400 K	La03	10 K, 100 K, 200 K, 400 K
La005_Fe195_800	10 K, 200 K, 400 K		
La01_Fe19_800	10 K, 400 K		

4. Results and Discussions

This chapter reports on the results obtained by XRD, TEM, Mössbauer spectroscopy and magnetic measurements. It is divided into three parts. In the first part, the results of the samples prepared by the microemulsion route are presented. The obtained crystal structure, cation distribution within the spinel network and the obtained coercivity are discussed. In the second part, the same discussion is made for the samples prepared by the sol-gel method. In the third part, a discussion comparing the results of the two different kinds of samples is presented.

4.1. Samples prepared by the microemulsion route

4.1.1. X-ray diffraction

X-ray diffraction patterns were measured at room temperature. Figure 4.1 shows the diffraction patterns for the Co550 and Co950 samples. Positions of all peaks in Co550 coincide well with the characteristic peaks for spinel structure of $CoFe_2O_4$ [30]. With the increasing annealing temperature additional peaks appear that belong to the α-Fe_2O_3 (hematite).

The XRD patterns for the La-doped samples are shown in Figure 4.2. Positions of all peaks belong to the spinel phase, there is no detectable trace of other impurities, and therefore the La-doped samples are found to be single-phase. The significant broadening of the diffraction lines in comparison to the undoped $CoFe_2O_4$ suggests smaller size of particles upon doping.

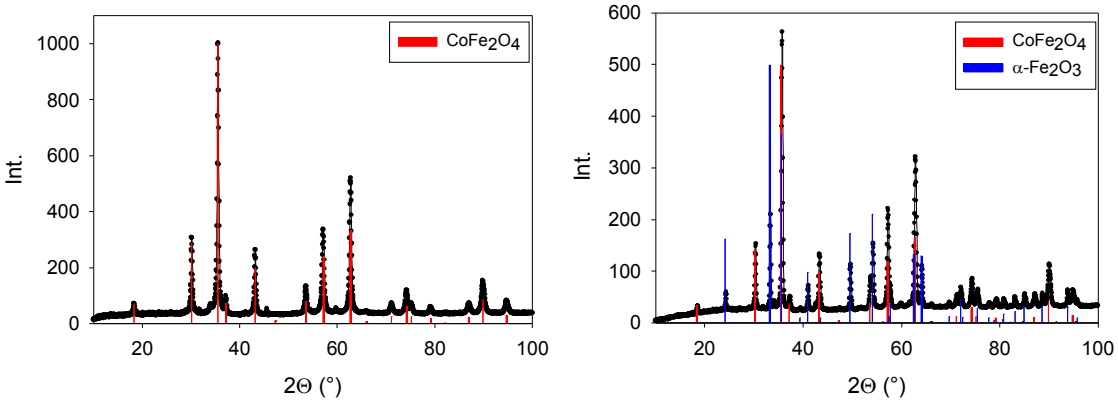

Figure 4.1: X-ray diffraction patterns of the $CoFe_2O_4$. The left plot displays Co550, the right plot displays Co950. The lines demonstrate the Bragg positions of the observed phases.

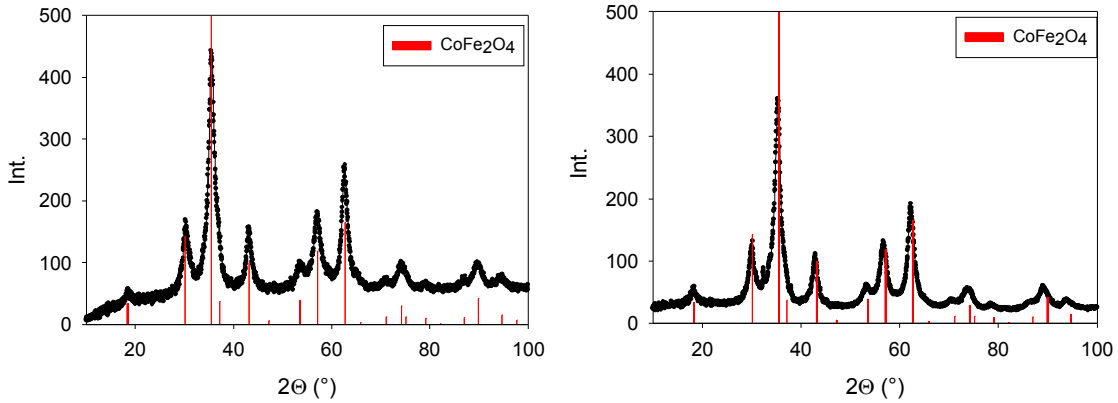

Figure 4.2: X-ray diffraction pattern of the La-doped $CoFe_2O_4$. The left plot displays La01, the right plot displays La02. The lines demonstrate the Bragg positions of the observed phases.

To obtain lattice parameters and particle diameters (mean size of the coherently diffracting domain) the Rietveld refinement was used within the program Fullprof (see section 3.2.1.). The resulting parameters are presented in Table 4.1.

The variation of lattice parameters in undoped $CoFe_2O_4$ nanoparticles is probably due to imperfections in crystal lattice. The particle diameters of the undoped $CoFe_2O_4$ samples increase with the increasing annealing temperature as expected [53].

There is a significant decrease of particle diameters upon La doping. The introduction of small amount of the La^{3+} ions (La01 sample) did not give a detectable change in lattice constant. However the twice-higher amount of the La^{3+} ions (La02 sample) causes a decrease of the lattice parameter *a*. The resulting lattice parameters are in good agreement with those obtained by other workers [54].

The La03 sample, where the La^{3+} ions were doped instead of the Fe^{3+} ions, shows significant increase of the lattice parameter *a*. As was discussed in the theoretical part (section 2.4.2.3.), the introducing of the La^{3+} ions in spinel lattice could lead to cation redistribution that affects the value of lattice parameters [9]. Therefore the cation distribution within spinel network in these two samples should be different.

Table 4.1: Lattice parameters, *a* particle diameters, *d* Bragg factor, R_B and crystallographic factor, R_F obtained from XRD:

sample	*d* (nm)	*a* (Å)	R_B	R_F
Co550	22	8.39(7)	7.9	8.6
Co750	26	8.37(7)	7.8	8.2
Co950	34	8.38(7)	12.1	7.2
La01	4.2	8.38(0)	3.2	3.0
La02	4.2	8.35(7)	11.2	14.7
La03	5.7	8.42(9)	14.6	17.1

4.1.2. TEM (Transmission electron microscopy)

Selected samples were characterized using the TEM, the micrographs are shown in Figure 4.3. The TEM observations confirmed the smaller particle size of the La-doped samples (La01, La03) in comparison to the undoped $CoFe_2O_4$ (Co750). The particle diameters range from 5 to 25 nm in case of the La-doped samples. The micrograph of the sample Co750 shows small particles and its aggregates.

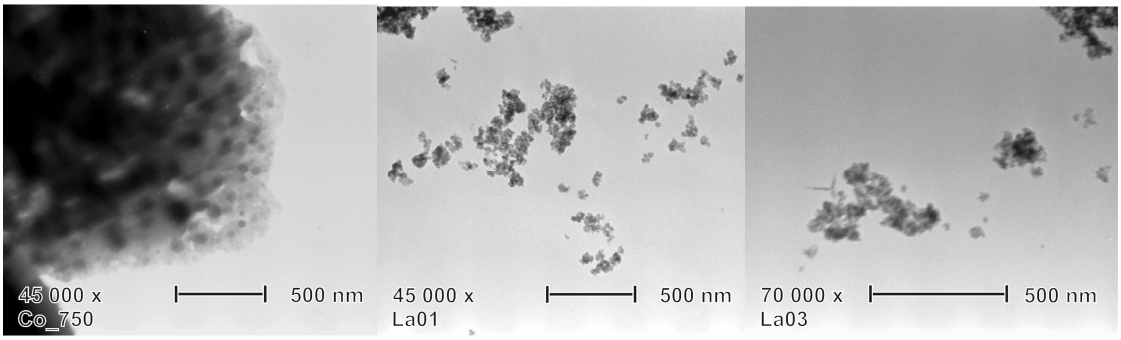

Figure 4.3: TEM observation of the Co750, La01 and La03 samples.

4.1.3. Mössbauer spectroscopy

Mössbauer spectroscopy at room temperature was performed for all samples prepared by the microemulsion route. Furthermore, for selected sample the measurements of the spectra in low temperature in absence and presence of 6 T field applied perpendicular to the direction of γ-ray were performed. The Figures of Mössbauer spectra contain the measured data (black dots), their fits (black lines), and additionally the individual subspectra (colorful lines). In all Tables this notation is used: O_h means octahedral sites, T_d tetrahedral sites, para/super means particles in paramagnetic or superparamagnetic state, block means particles in blocked state, respectively.

4.1.3.1. The undoped $CoFe_2O_4$ nanoparticles

Room-temperature Mössbauer spectroscopy

The room-temperature Mössbauer spectra for the Co550 and Co750 samples are shown in Figure 4.4. Both spectra consist of sextets indicating blocked state of nanoparticles that is in good agreement with magnetic measurements (see section 4.1.4.1.), the blocking temperatures for these samples were found out well above the room temperature.

The fitting model consists of two sextets corresponding to the octahedral and tetrahedral sites in the spinel structure. The resulting Mössbauer parameters for both samples are summarized in Table 4.2 . Values of the isomer shift, δ are consistent with the high spin

state of Fe^{3+} ions in the spinel environment and the values of the hyperfine fields are typical for the $CoFe_2O_4$ spinel structure [48, 55].

The assignment of sextets to the octahedral and tetrahedral sites, respectively, were done from the values of the isomer shift as the isomer shift is lower for the tetrahedral sites, because of the smaller volume available for the ions at these sites [56]. However this assignment does not agree with the obtained relative areas of the sextets that should correspond to the amount of Fe^{3+} ions in the tetrahedral and octahedral sites, respectively (as two third of Fe^{3+} ions cannot be located in the tetrahedral sites, in the ideal spinel structure with no degree of inversion the ratio of relative area should be 1:1).

It is worth to emphasize that the quantitative analysis made from the relative areas is only estimative due to overlap of the sextets belonging to the octahedral and tetrahedral sites, respectively. Therefore the calculated relative areas are estimations with the error about 20%. Moreover at room temperature, the area of the peaks does not correspond to the relative concentration of Fe^{3+} ions in the tetrahedral and octahedral sites, as the recoilless factor is not same for these two sites.

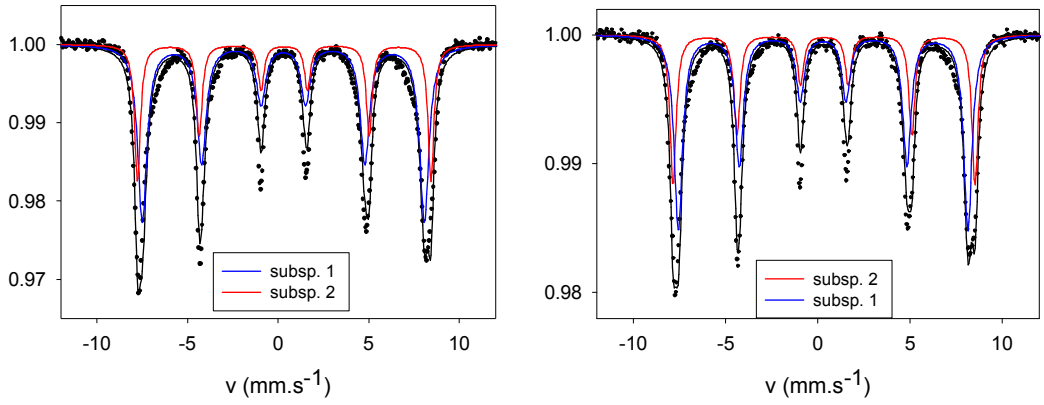

Figure 4.4: Mössbauer spectra of the Co550 (left plot) and Co750 (right plot) samples measured at room temperature.

Table 4.2 : Mössbauer parameters of the undoped $CoFe_2O_4$ measured at room temperature:

	Isomer shift δ ($mm.s^{-1}$)	Quadrupole. split. ΔE_q ($mm.s^{-1}$)	Hyperfine field B_{Hf} (T)	FWHM ($mm.s^{-1}$)	Rel. area (%)	Interpr.
Co550						
Subsp. 1	0.28	0.0	48.3	0.61	67	Fe^{3+} T_d
Subsp. 2	0.33	0.0	50.3	0.39	33	Fe^{3+} O_h
Co750						
Subsp. 1	0.28	0.0	48.8	0.54	63.5	Fe^{3+} T_d
Subsp. 2	0.34	-0.02	50.9	0.40	36.5	Fe^{3+} O_h

In-field Mössbauer spectroscopy

The Co750 sample was measured at 4.2 K without and with applied field of 6 T perpendicular to the direction of γ-ray. The Mössbauer spectra are shown in Figure 4.5. By applying magnetic field the overlapping sextets show completely resolved splitting of the outer and middle lines as the applied field adds to the magnetic hyperfine field at the tetrahedral sites and subtracts from the hyperfine field at the octahedral sites [56]. Each of them can be well fitted by one sextet.

The fitting procedure was done as was described in the experimental part (section 3.3.5.). The obtained Mössbauer parameters are summarized in Table 4.3. The spin canting angles with respect to the external magnetic field were determined using relation (3.11):

$$\alpha_1 = 22°$$
$$\alpha_2 = 162°$$

where α_1, α_2 denotes the canting angle of the Fe^{3+} magnetic moments in the tetrahedral (subsp. 1) and octahedral sites (subsp. 2), respectively. It is obvious that magnetic moments in both sites are slightly canted with respect to the external applied field (no canting angles would correspond to values 0° or 180°) taking into account the error of fitting that is about 10°. As was expected, these values also confirmed the antiparallel orientation of magnetic moments in the tetrahedral and octahedral sites with respect to each other, if the precession of the magnetic moment around the applied field is considered.

The area of these two split sextets is proportional to the amount of Fe^{3+} in the tetrahedral and octahedral sites, the cation distribution, which represents the degree of inversion in these two sites is:

$$(Co_{0.26}Fe_{0.74})[Co_{0.74}Fe_{1.26}]O_4$$

where rounded brackets denote the tetrahedral sites and squared brackets denote the octahedral sites.

The resulting cation distribution confirmed that the structure is not completely inversed as was observed before [3, 56]. About one quarter of Co^{2+} ions occupy the tetrahedral sites.

It is important to note, that at low temperatures the recoilless factors are same for both sites and equal to each other. Therefore the obtained inversion rate is more accurately determined from the measurement at low temperature under the external magnetic field.

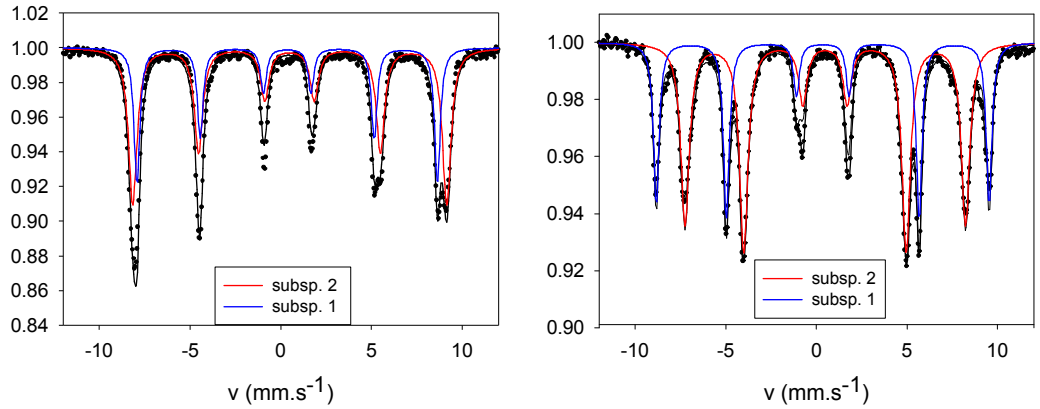

Figure 4.5: Mössbauer spectra of Co750 measured at 4.2 K without applied field (left plot) and with external applied field 6 T (right plot) perpendicular to γ-ray.

Table 4.3: In-field Mössbauer parameters of the Co750 sample:

	Isomer shift δ (mm.s^{-1})	Quadr. split. ΔE_q (mm.s^{-1})	Hyp. field B_{Hf} (T)	Eff. field B_{eff} (T)	FWHM (mm.s^{-1})	Rel. area (%)	Interpr.
Subsp. 1	0.35	0.00	51.4	57.1	0.39	37.0	Fe^{3+} T_d
Subsp. 2	0.49	0.02	53.7	48.1	0.56	63.0	Fe^{3+} O_h

4.1.3.2. La-doped samples

Room-temperature Mössbauer spectroscopy

The Mössbauer spectra of the La02 and La03 samples measured at room temperature are shown in Figure 4.6 and obtained Mössbauer parameters are summarized in Table 4.4.

The spectra of the La01 and La02 samples consist of broad sextet with asymmetric peaks, quadrupole doublet and a broad singlet. In comparison to the undoped $CoFe_2O_4$ the lines are significantly broader and the obtained hyperfine fields are lower due to smaller particle size and the presence of the La^{3+} ions. The La^{3+} ions are randomly distributed preferably within the octahedral sites due to their large ionic radii [12]. This random distribution gives rise to different environment for the octahedral and tetrahedral sites, therefore the increased distribution of the hyperfine fields leads to broadening of lines. The broadening of lines upon Nd doping was observed by L. Zhao [53]. The distributions of hyperfine fields were fitted using a broad sextet. The doublet demonstrates that part of the sample is in superparamagnetic state. The singlet is assigned to the part of the sample that is near its blocking temperature.

The line width of the La02-spectrum is broader in comparison to the La01-spectrum. Introducing twice higher amount of La^{3+} (La02) causes the higher distribution of hyperfine fields, therefore the line broadening is more pronounced.

The La03 sample shows a different tendency, majority of the sample is in superparamagnetic state and only minority is in the blocked state. This is consistent with magnetic measurement (shown further – section 4.1.4.1.), where the mean blocking temperature for the La03 sample is below the room temperature.
The singlets were not counted into the ratio of the relative area of individual subspectra due to broad width of lines.

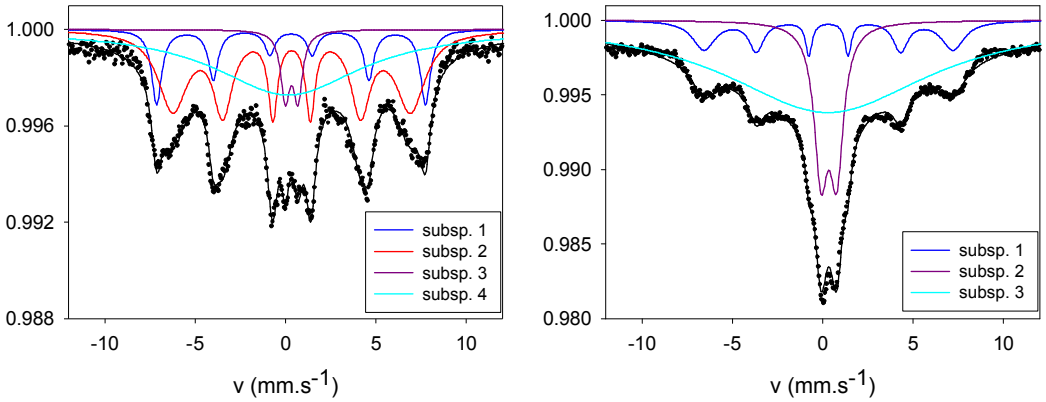

Figure 4.6: Mössbauer spectra of the La02 (left plot) and La03 (right plot) samples measured at room temperature.

Table 4.4: Mössbauer parameters of the La-doped samples measured at room temperature:

	Isomer shift δ (mm.s^{-1})	Quadrupole splitting ΔE_q (mm.s^{-1})	Hyperfine field B_{Hf} (T)	FWHM (mm.s^{-1})/ distribution of B_{hf} (T)	Rel. area (%)	Interpr.
La01						
Subsp. 1	0.28	0.004	46.4	0.62	25.3	Fe^{3+} T_d
Subsp. 2	0.32	-0.03	41.3	0.39/ 8.8	71.4	Fe^{3+} O_h
Subsp. 3	0.30	0.72	N/A	0.45	3.3	Fe^{3+} super/para
Subsp. 4	0.15		N/A	11.04	-	Fe^{3+} near T_B
La02						
Subsp. 1	0.30	0.0	46.2	0.67	22.3	Fe^{3+} T_d
Subsp. 2	0.33	0.0	40.9	0.37/9.8	68.7	Fe^{3+} O_h
Subsp. 3	0.33	0.7	N/A	0.61	9	Fe^{3+} super/para
Subsp. 4	0.14		N/A	9.83		Fe^{3+} near T_B
La03						
Subsp. 1	0.31	0.0	42.8	0.23/ 8	40.2	Fe^{3+} block
Subsp. 2	0.33	0.87	N/A	0.92	59.8	Fe^{3+} super/para
Subsp. 3	0.28		N/A	13.82	-	Fe^{3+} near T_B

In-field Mössbauer spectroscopy

The La02 sample was measured at 4.2 K without and with applied field of 6 T; these spectra are shown in Figure 4.7 and the obtained Mössbauer parameters are summarized in Table 4.5. The fitting procedure was done in same way as discussed previously.

The high intensities of the inner lines (3, 4) is caused by the experimental error (high absorption due to high amount of the measured sample) therefore the fit does not well correspond to measured data at these line positions.

The splitting of sextets is not as significant as in the undoped $CoFe_2O_4$ that can be attributed to the broadening of lines due to the presence of the La^{3+} ions, as was discussed in previous section. From the fitted B_{hf} and B_{eff} the spin canting angles with respect to the external magnetic field were determined as:

$$\alpha_1 = 136°$$

$$\alpha_2 = 41°$$

where α_1, α_2 denotes canting angle of the Fe^{3+} magnetic moments in the octahedral (subsp. 1) and tetrahedral sites (subsp. 2), respectively. The spin canting in the La-doped sample is much higher than in the undoped $CoFe_2O_4$. Therefore it is supposed that introducing the La^{3+} ions in the spinel lattice causes the spin frustration at the surface that leads to higher spin canting.

From relative area of the lines the degree of inversion was determined as (with the assumptions of La^{3+} presented in the octahedral sites):

$$(Co_{0.36}Fe_{0.64})[Co_{0.44}Fe_{1.36}La_{0.2}]O_4 .$$

The structure is also not completely inversed and the degree of inversion is higher than in the undoped $CoFe_2O_4$ that is in good agreement with results published by group of L. B. Tahar [9]. They observed that the introducing of the La^{3+} ions into the spinel lattice causes transferring of the Co^{2+} ions from the tetrahedral to octahedral sites and opposite transferring of the Fe^{3+} ions.

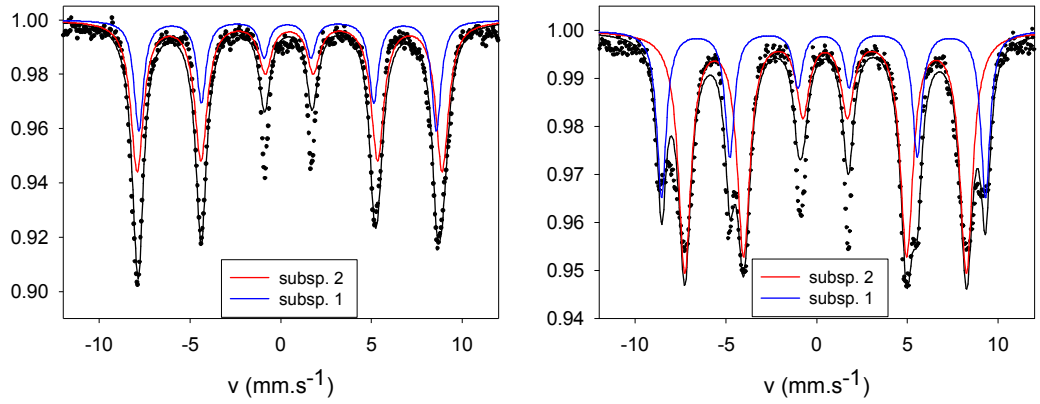

Figure 4.7: Mössbauer spectra of La02 measured at 4.2 K with zero applied field (left plot) and external applied field 6 T (right plot).

Table 4.5: In-field Mössbauer parameters of the La02 sample:

	Isomer shift δ (mm.s^{-1})	Quadrupole splitt. ΔE_q (mm.s^{-1})	Eff. field B_{eff} (T)	Hyp. field B_{Hf} (T)	FWHM (mm.s^{-1})	Rel. area (%)	Interpr.
Subsp. 1	0.37	0.00	55.4	50.9	0.62	32.2	Fe^{3+} T_d
Subsp. 2	0.48	0.02	48.2	52.2	0.85	67.8	Fe^{3+} O_h

4.1.4. Magnetic measurements

Magnetization measurements were performed for all samples as a function of temperature (known as the zero field cooled, ZFC and field-cooled FC curves) in low applied field of 10 mT and as a function of the applied field at constant temperature. For the La01 and La03 samples the a.c. susceptibility was also measured.

4.1.4.1. The ZFC and FC experiments

The temperature dependencies of the ZFC-FC magnetization of the Co550 sample are shown in Figure 4.8. All samples of the undoped $CoFe_2O_4$ show the same behavior; there are no significant maxima of the ZFC curve and the lack of a bifurcation point of the ZFC and the FC curve indicates that the blocking temperature is well above 400 K. Therefore same measurements were performed from 310 K up to 700 K using VSM with oven (see Figure 4.8, right plot). The obtained values of the blocking temperature, T_B and the irreversibility temperature, T_{irr} are summarized in Table 4.6. These values are approximative due to the broad maxima of the ZFC curve (the error was estimated to be around 20 K). With increasing particle size, the T_B slightly increases with respect to error as is consistent with relation (2.27).

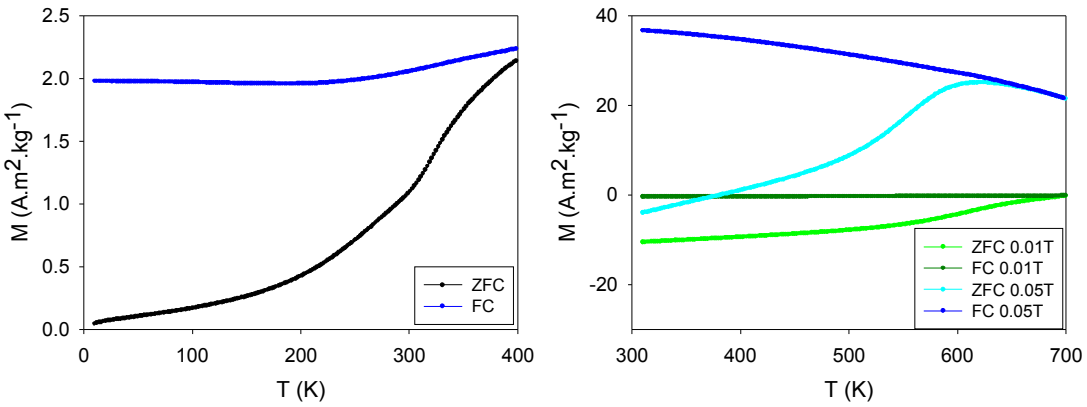

Figure 4.8: Temperature dependence of ZFC-FC magnetization of the Co550 sample measured at different fields. In left plot the measurement performed in temperature range 10 – 400 K is shown, in right plot the temperature range was 310 – 700 K.

Table 4.6: The blocking, T_B and irreversibility, T_{irr} temperature for the undoped $CoFe_2O_4$:

sample	$\mu_0 H$ (T)	T_B (K)	T_{irr} (K)
Co550	0.1	700	-
	0.5	620	660
Co750	0.5	600	630
Co950	0.5	660	700

In comparison to the undoped $CoFe_2O_4$, the La-doped samples show different behavior of the ZFC-FC curves (see Figure 4.9). The maxima of the ZFC curve that roughly correspond to the T_B are observed below 400 K. However the ZFC and FC curves do not coincide signalizing that the T_{irr} is still above 400 K. The differences of the T_B and T_{irr} indicate the particle size distribution and the presence of inter-particle interactions [2]. The ZFC-FC measurements of the La01 sample were performed also in different magnetic fields. The decrease of the blocking temperature with increasing field was observed as is consistent with relation (2.27). The obtained blocking and irreversibility temperatures are presented in Table 4.7.

The La01 and La02 samples have approximately the same particle size therefore the values of their blocking temperatures are comparable. With increasing amount of La^{3+} ion in $CoFe_2O_4$ the value of the blocking temperature remains more or less intact, taking into account the estimation error of ± 15 K. On the other hand, the T_B is significantly lower for the La03 sample where the La^{3+} ion was doped instead of Fe^{3+} and the sample consists of larger particles. Also the difference of the T_B and T_{irr} is quite higher indicating larger particle size distribution.

The lower blocking temperature in the La-doped samples in comparison to the pure $CoFe_2O_4$ is attributed mostly to the reduced particle size.

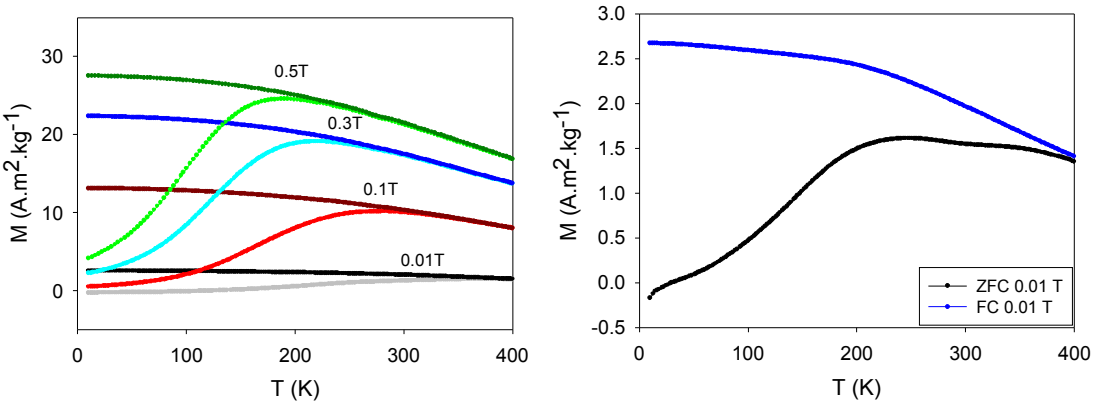

Figure 4.9: Temperature dependence of ZFC-FC magnetization measured at different fields of the La01 (left plot) and La03 (right plot) samples. The ZFC curve is that of lower magnetization at lower temperature, the FC curve is that of higher magnetization at higher temperature.

Table 4.7: The blocking T_B and irreversibility T_{irr} temperature for the La-doped samples:

sample	$\mu_0 H$ (T)	T_B (K)	T_{irr} (K)
La01	0.01	370	-
	0.1	280	360
	0.3	220	350
	0.5	190	370
La02	0.01	380	-
La03	0.01	250	-

4.1.5. Hysteresis loops in the blocked state

The hysteresis loops of the Co550, Co950, La01 and La03 samples are shown in Figures 4.10 and 4.11. From these measurements the coercivity, remanent magnetization and magnetization at 7 T were determined. The obtained values are summarized in Table 4.8 and Table 4.9 for the undoped $CoFe_2O_4$ and the La-doped samples, respectively.

The coercivity at 10 K of the undoped $CoFe_2O_4$ increases in consistency with increasing particle size as the energy that is needed to flip the magnetic moment is proportional to the volume of particles. With increasing temperature, the coercivity steadily decreases to a non-zero value at 400 K indicating that the particles are still blocked in consistency with the measurement of the ZFC-FC curves. The values of the magnetization at 7 T reach the expected values around 80 $A.m^2.kg^{-1}$ [6]. This result is consistent with the small canting angle obtained from Mössbauer spectroscopy.

The smaller particle size in the La-doped samples exhibit larger coercivity at 10 K that is of the same order as those reported by L. B. Tahar in nanoparticles prepared by the polyol method [9]. This enhancement can be explained by presence of the non-negligible surface effects that leads to increase of the surface anisotropy constant. The magnetization at 7 T is then slightly lower due to the spin canting effect [24]. At 400 K, the magnetization dependencies on applied field of the La-doped samples show no hysteresis indicating the samples are in superparamagnetic state.

The really small coercivity value of the La03 sample in comparison to other La-doped samples with nearly same particle size is very surprising and further experiments are needed to explain this effect.

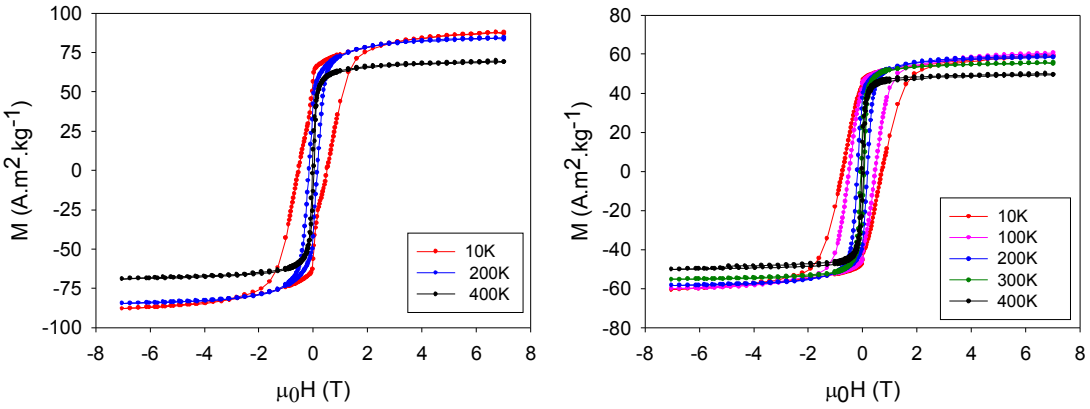

Figure 4.10: Hysteresis loops of the Co550 (left plot) and Co950 (right plot) samples measured at different temperatures.

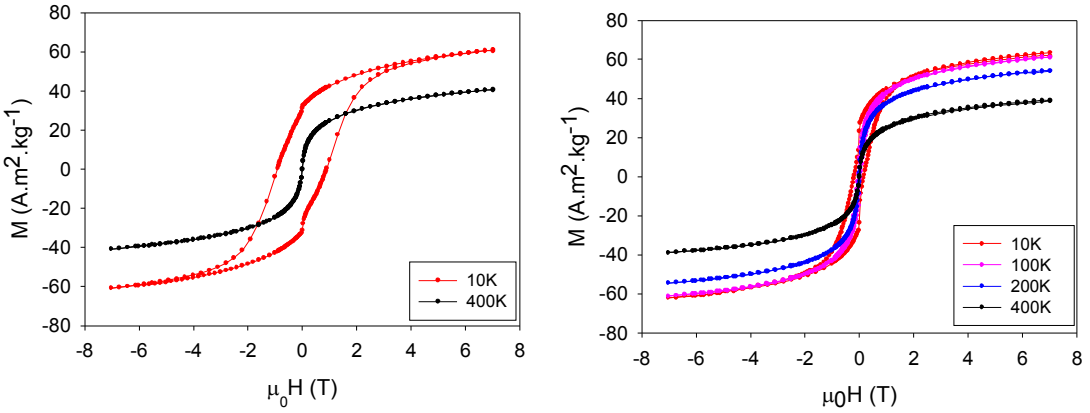

Figure 4.11: Hysteresis loops of the La01 (left plot) and La03 (right plot) samples measured at different temperatures.

Table 4.8: The coercivity (H_C), remanent magn. (M_r) and magn. at 7 T (M_{7T}) of the undoped $CoFe_2O_4$:

Sample	T (K)	H_c (T)	M_{7T} (A.m^2.kg^{-1})	M_r (A.m^2.kg^{-1})
Co550	10	0.52	88.4	56.5
	200	0.16	84.3	42.3
	400	0.03	69.5	13.4
Co750	10	0.73	85.2	60.1
	200	0.22	81.9	45.3
	400	0.03	68.3	12.5
Co950	10	0.73	60	45.3
	100	0.48	60	44.9
	200	0.18	58.9	37.6
	300	0.06	55.4	22.1
	400	0.03	50.1	15.0

Table 4.9: The coercivity (H_C), remanent magn. (M_r) and magn. at 7 T (M_{7T}) of the La-doped samples:

Sample	T (K)	H_c (T)	M_{7T} (A.m^2.kg^{-1})	M_r (A.m^2.kg^{-1})
La01	10	0.90	60.7	31.2
	400	0.0	40.9	0.0
La02	10	1.03	53.7	26.3
	200	0.04	49.5	4.0
	400	0.0	36.3	0.0
La03	10	0.18	62.1	23.4
	100	0.04	61.1	9.4
	200	0.01	54.2	2.4
	400	0.0	38.8	0.0

4.1.5.1. Magnetization curves in the SPM state

As the La-doped samples exhibit no hysteresis at 400 K, the universal curve M/M_s vs. $\mu_0 H/T$ could be fitted using the Langevin function (relation (2.28)). However, the La-doped samples do not show saturation of magnetization even in applied field of 7 T (see Figure 4.11) due to non-negligible surface effects that were reported by other authors for small-sized nanoparticles [57-58]. At high temperatures two contributions to the magnetization are proposed: the superparamagnetic core that saturates according to the Langevin law and the paramagnetic shell that displays the linear behavior.

Therefore the data were corrected by subtracting the linear contribution of the paramagnetic-like shell. For comparison, both the uncorrected and corrected curves were fitted and the results are plotted in Figure 4.12. The obtained values of the average magnetic moments are summarized in Table 4.10 where μ_1 is the magnetic moment per nanoparticle and μ_2 is magnetic moment of the spinel unit cell. It is obvious that the fit better corresponds to the experimental data after subtracting the paramagnetic contribution.

The magnetic moment per unit cell of the $CoFe_2O_4$ varies from 3 μ_B (inverse spinel) to 7 μ_B (normal spinel). The calculated values of the magnetic moments are in the range between these two boundaries, however the La01 and La02 samples corresponds to the normal structure. The difference could be either due to non-negligible particle size distribution that was not included into our fitting and also due to spin canting that lowers the saturation magnetization, hence it would correspond to lower degree of inversion.

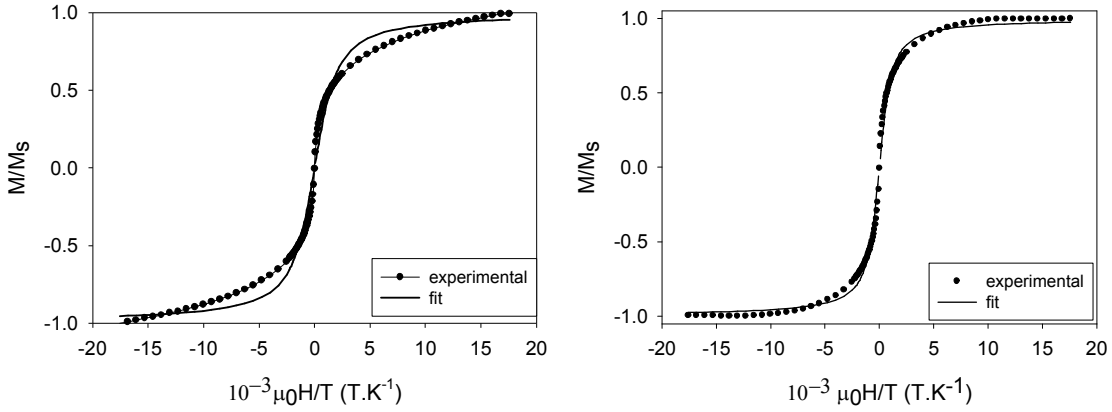

Figure 4.12: Fit of the Langevin function for the La01 sample before correction (left plot) and after correction (right plot) to paramagnetic part of sample.

Table 4.10: The magnetic moment per the particle, μ_1 and the unit cell, μ_2 obtained from Langevin fit for the La-doped samples:

	Before correction		After correction	
sample	μ_1 (μ_B)	μ_2 (μ_B)	μ_1 (μ_B)	μ_2 (μ_B)
La01	1878	3.6	3393	6.5
La02	1625	3.1	3224	6.2
La03	2061	1.57	2277	2.6

4.1.6. A.c. susceptibility

The La01 and La03 samples have the blocking temperatures below 400 K therefore measurements of temperature dependence of the a.c. susceptibility were performed (see Figure 4.13) in the temperature range 10 – 400 K.

The real part of the susceptibility exhibits a broad flat maximum that shifts to higher temperature with increasing frequencies. The La03 sample shows two broad maxima that is probably due to relaxation of two different fractions in the sample. This behavior is correspondent with the ZFC-FC measurement, the ZFC curve as the χ' also displays two broad maxima over a large temperature range indicating the particle size distribution in the sample. For fitting procedure the maxima located in the lower temperature were used, they belong to relaxation process of the fraction with smaller particles.

The dependence of the ln$f$ vs. T_B were fitted using Vogel-Fulcher law (relation (2.29)) with effort to involve the inter-particle interactions in the calculations. The obtained relaxation times, τ_0 and anisotropy effective constants, K_{eff} are summarized in Table 4.11. There is a contradiction between the relaxation times obtained from the a.c. susceptibility and results of the Mössbauer spectroscopy. The Mössbauer spectra of the La01 and La03 sample showed the magnetic ordered state at room temperature signalizing that the relaxation time is of about the same order as measuring time of

Mössbauer spectroscopy (around 10^{-7}s – 10^{-8}s) or lower. As the Vogel-Fulcher law is applicable only in case of low interparticle interaction, these results suggest that the inter-particle interactions in these samples are strong and they cannot be treated by the Vogel-Fulcher law.

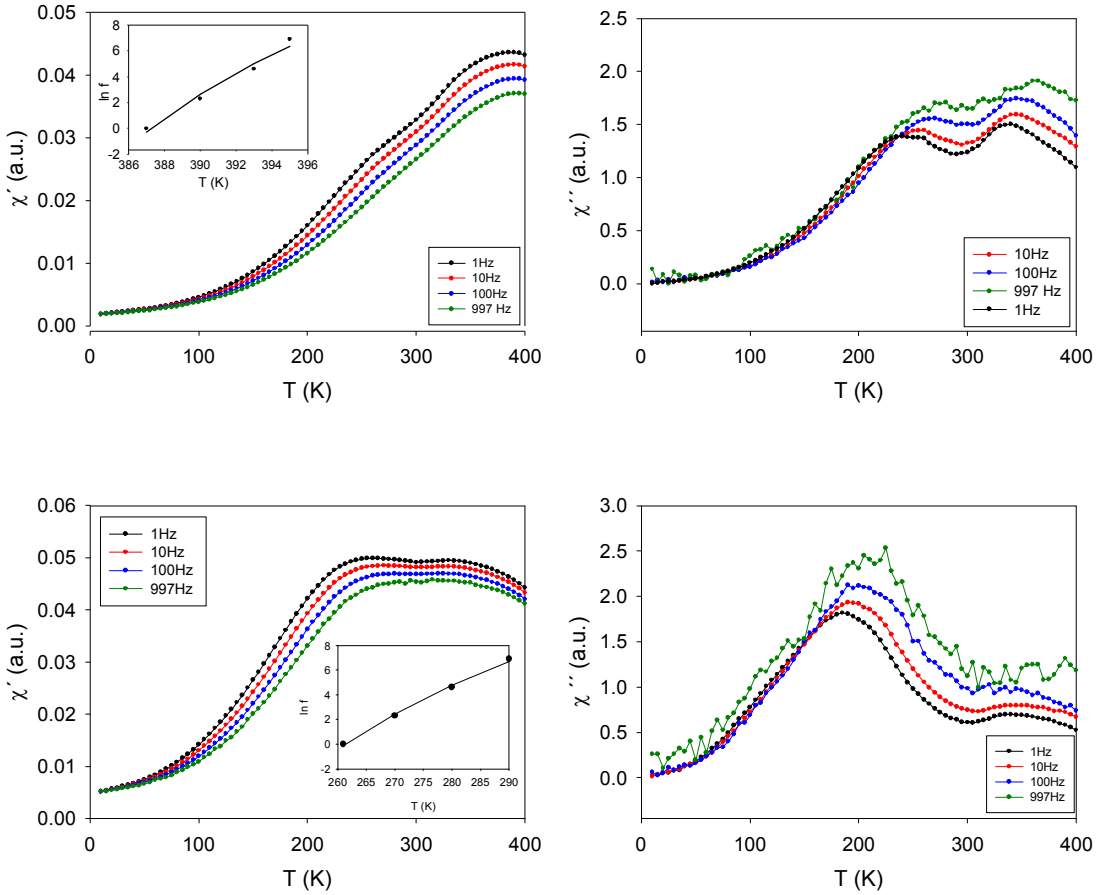

Figure 4.13: Temperature dependence of a.c. susceptibility at different frequencies of the La01 (top panel) and La03 (bottom panel) samples. The inset shows fit according to Vogel-Fulcher law.

Table 4.11: Fitted parameters from the Volger-Fulcher law:

sample	τ_0 (10^{-12}s)	T_0 (K)	K_{eff} (J.cm^{-3})
La01	2.2	362.3	0.24
La03	2.07	175.7	0.32

4.2. Nanocomposites by the sol-gel method

4.2.1. X-ray diffraction

The X-ray diffraction (XRD) phase analysis showed that all samples consist of at least of two phases – peaks belonging to the spinel structure of $CoFe_2O_4$ and α-Fe_2O_3 were observed. The α-Fe_2O_3 phase was also observed in the La-doped $CoFe_2O_4$ nanoparticles prepared by sol-gel method by other authors [11].

The details of phase composition of measured samples are summarized in Table 4.12, where the phase content is roughly described as follows: x means that only trace amount was detected, xx means that the peaks are well distinguishable and xxx means considerable intensity of the foreign peaks.

In Figure 4.14 the XRD patterns of the samples annealed at 800°C doped by different amount of La^{3+} instead of Co^{2+} are presented. With increasing amount of La^{3+} the broad peak around 25° is observed that can be attributed to the amorphous fraction of the sample comprising the SiO_2 matrix, and probably also silicates or lanthanum oxide. The same tendency was observed in samples annealed at 900°C.

With higher annealing temperature (1000°C, 1100°C) this peak practically disappears and crystalline phases of α-quartz SiO_2, La_2O_3 or $LaFeO_3$ are detected instead (see Figure 4.15). The appearing of crystalline SiO_2 at annealing temperature 1000°C is unusual as in $CoFe_2O_4/SiO_2$ the amorphous matrix is stable up to 1100°C and converts to its crystalline form at 1100°C or higher temperature. Therefore introducing La^{3+} into the composite affects the stability of amorphous matrix that is transformed to the crystalline phase already at 1000°C.

Samples where La^{3+} was doped instead of Fe^{3+} showed a little different behavior (see Figure 4.16). When only small amount of La^{3+} is doped, the broad peak around 25° is observed that belongs to the amorphous fraction of the sample. However, even at low annealing temperature, the increasing amount of La^{3+} stimulated formation of other phases as cobalt silicate and lanthanum orthoferrite. Decrease of the intensity of the peak related to the amorphous fraction was also observed.

These results indicate that if more than $x = 0.2$ amount of the La^{3+} ions are doped in the sample, the sample is multiphase (see Figure 4.15). This effect was also observed by other authors [12, 53, 59].

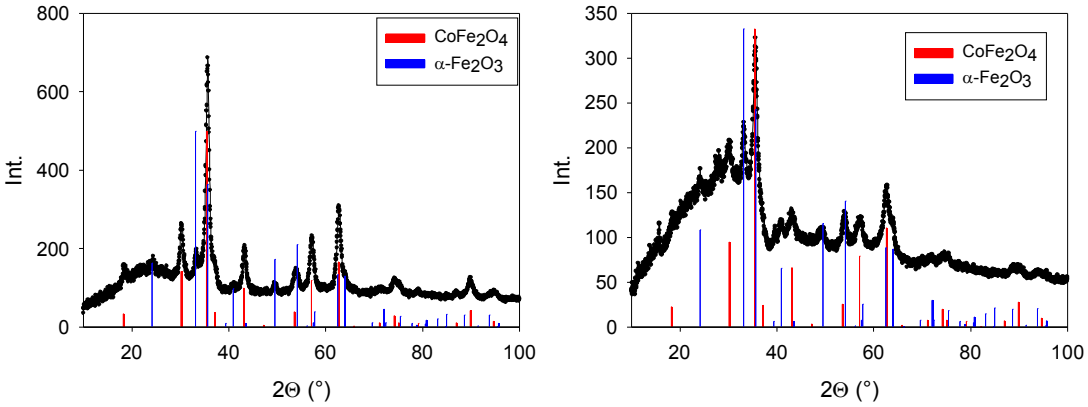

Figure 4.14: X-ray diffraction patterns of the La005_Co095_800 (left plot) and La05_Co05_800 (right plot) samples. The lines demonstrate the Bragg positions of the observed phases.

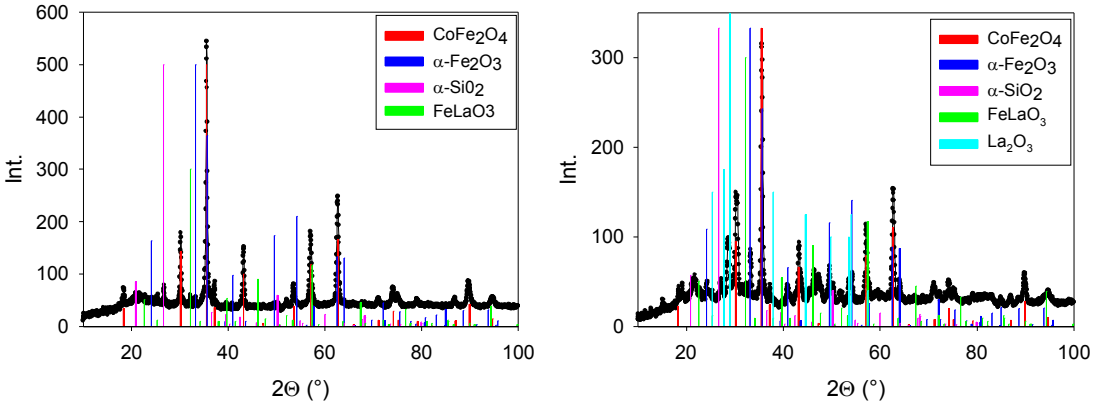

Figure 4.15: X-ray diffraction patterns of the La005_Co095_1100 (left plot) and La05_Co05_1100 (right plot) samples. The lines demonstrate the Bragg positions of the observed phases.

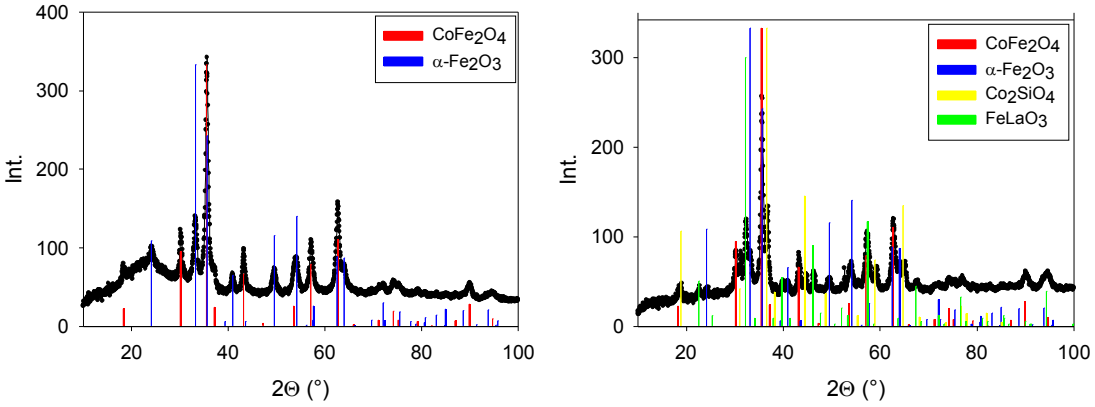

Figure 4.16: X-ray diffraction patterns of the La001_Fe199_800 (left plot) and La05_Co05_1100 (right plot)samples. The lines demonstrate the Bragg positions of the observed phases.

Table 4.12: The XRD phase analysis of the sol-gel samples:

sample	$CoFe_2O_4$	α-Fe_2O_3	$FeLaO_3$	La_2O_3	SiO_2	Co_2SiO_4
La005_Co095_800	xxx	xx				
La05_Co05_800	xxx	xxx				
La05_Co05_800_leach	xxx	x				
La005_Co095_900	xxx	x				
La05_Co05_900	xxx	xxx				
La005_Co095_1000	xxx	x				
La01_Co09_1000	xxx	xx				
La02_Co08_1000	xxx	xx				
La03_Co07_1000	xxx	xxx		x	x	
La04_Co08_1000	xxx	xxx		xx	x	
La05_Co05_1000	xxx	xxx		xx	xx	
La005_Co095_1100	xxx	x	x		xx	
La05_Co05_1100	xxx	xxx	x	xxx	xx	
La001_Fe199_800	xxx	xx				
La005_Fe195_800	xxx	x				
La01_Fe19_800	xxx	x				
La02_Fe18_800	xxx	x	xx			xx

Rietveld refinement

The two-phase samples were fitted by means of the Rietveld procedure to obtain lattice parameters and the sizes of the mean coherent diffraction domain size (particle diameter). These values are summarized in Table 4.13 and Table 4.14 respectively. The broad peak around 25° corresponding to amorphous matrix was included into the background.

By comparing the samples doped by the same amount of La^{3+}, it is obvious that with the increasing annealing temperature, the particle size increases as expected. However, no dependence of the particle size on amount of La^{3+} was observed

Most of the lattice parameters are in good agreement with obtained by L.B.Tahar [9] (*a = 8.401 Å*) suggesting occupation of La^{3+} ion in the spinel lattice. However, there is no significant increase of lattice parameters of $CoFe_2O_4$ upon higher La^{3+} doping as would be expected [59]. For the higher annealing temperatures (1000°C, 1100°C) increase of the lattice parameter of the α-Fe_2O_3 is observed indicating possibility of La^{3+} occupation in the α-Fe_2O_3 lattice.

For lower annealing temperatures (800°C, 900°C) the La^{3+} ions can be also dissolved in the amorphous matrix probably in a form of lanthanum orthoferrite, therefore the change in lattice parameters in most of the samples was not observed.

Table 4.13: Lattice parameters, *a* particle diameters, *d* Bragg factor, R_B and crystallographic factor, R_F obtained from XRD for the phase $CoFe_2O_4$:

Sample	*d* (nm)	*a* (Å)	R_B	R_F
La005_Co095_800	9	8.39(1)	11.3	14.9
La05_Co05_800	5	8.37(5)	8.8	7.8
La005_Co095_800_leach	8	8.39(2)	6.0	9.5
La005_Co095_900	11	8.39(5)	9.9	11.7
La05_Co05_900	11	8.39(1)	19.5	17.8
La005_Co095_1000	15	8.39(8)	7.5	8.8
La01_Co09_1000	25	8.39(9)	8.2	10.6
La02_Co08_1000	21	8.39(9)	11.1	12.6
La03_Co07_1000	18	8.39(5)	12.4	7.7
La001_Fe199_800	12	8.36(6)	7.8	9.0
La005_Fe195_800	12	8.36(1)	8.3	7.5
La01_Fe19_800	11	8.39(3)	6.3	6.3

Table 4.14: Lattice parameters, *a* particle diameters, *d* Bragg factor, R_B and crystallographic factor, R_F obtained from XRD for the phase α-Fe_2O_3

Sample	*d* (nm)	*a* (Å)	*c* (Å)	R_B	R_F
La005_Co095_800	16	5.04(9)	13.74(9)	22.3	37.5
La05_Co05_800	9	5.03(8)	13.72(5)	10.9	11.4
La005_Co095_800_leach	7	5.06(0)	13.71(4)	15.6	20.4
La005_Co095_900	14	5.04(6)	13.76(6)	17.8	41.0
La05_Co05_900	19	5.04(3)	13.74(8)	11.4	19.6
La005_Co095_1000	20	5.05(3)	13.72(8)	35.0	40.2
La01_Co09_1000	38	5.04(6)	13.76(3)	31.7	42.3
La02_Co08_1000	25	5.04(7)	13.76(3)	24.1	38.6
La03_Co07_1000	31	5.04(4)	13.76(0)	11.1	13.5
La001_Fe199_800	11	5.02(9)	13.73(0)	14.7	27.3
La005_Fe195_800	13	5.01(9)	13.75(1)	15.7	13.8
La01_Fe19_800	11	5.04(9)	13.79(2)	16.2	14.4

4.2.2. TEM

For selected samples the TEM measurements were performed, the micrographs are displayed in Figure 4.17. Some particles at the edges of samples can be distinguished. The broad particle distribution can be seen as the particles belong to different phases with different particle size.

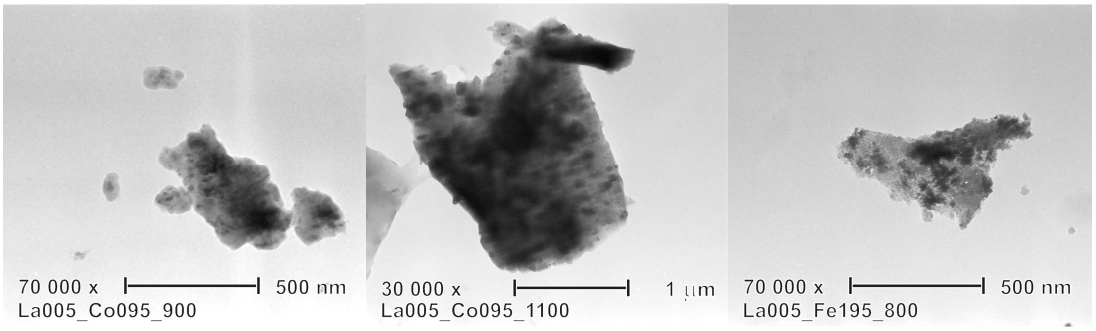

Figure 4.17: TEM observation of the La005_Co095_900, La005_Co095_1100 and La005_Fe195_800 samples.

4.2.3. Mössbauer spectroscopy

4.2.3.1. Room-temperature Mössbauer spectroscopy

The main feature of all spectra is the sextet splitting that is consistent with magnetic measurement, which revealed the mean blocking temperatures above 400 K (section 4.2.4.1). The XRD measurement showed that the α-Fe_2O_3 is also present in all samples, so the Mössbauer spectra were always fitted with at least three sextets – two of them correspond to the $CoFe_2O_4$ (as the octahedral and tetrahedral sites of the spinel), and the third sextet corresponds to the α-Fe_2O_3.

In the composites annealed at 800°C and 900°C, respectively, an additional doublet is observed representing the non-negligible amount of particles in the super/paramagnetic state. Also the effect of the line broadening due to small particles can be seen when comparing the spectra of samples annealed at 800°C and 1100°C, respectively, as shown in Figure 4.18. The obtained Mössbauer parameters are summarized in Table 4.15.

The subspectra were assigned to the octahedral and tetrahedral sites from values of the isomer shifts [48, 56]. However these assignments are only estimative due to not resolved sextet and cannot be used to determine the degree of inversion on the octahedral and tetrahedral sites . The so-called saturation effect is observed in measured data (arbitrary high intensities of the inner lines) therefore the fits do not reflect the data very well at these line positions.

The fitting of the α-Fe_2O_3 was treated in two ways. At first, the tabulated values for the pure, bulk α-Fe_2O_3 ($\delta=0.38 mm.s^{-1}$, $\Delta E_q=-0.2 mm.s^{-1}$, $B_{hf}=51.8 T$) were used [48]. This fit can be seen in the left plot of Figure 4.19 for the sample La05_Co05_900. It is obvious that this model does not correspond to the results of the XRD measurements as only a few percents of the α-Fe_2O_3 were revealed by Mössbauer spectroscopy in comparison to the significant amount (35 %) of α-Fe_2O_3 detected by XRD.

As the limiting room-temperature hyperfine field, B_{hf} for the pure, bulk α-Fe_2O_3 is 51.8 T the value of the hyperfine field was “unlocked” and significant decrease of the B_{hf} was observed. It was earlier seen in the Al-doped α-Fe_2O_3 that the substitution of

diamagnetic for paramagnetic ions leads to reduction of the saturation hyperfine field. This would correspond to the possibility of α-Fe_2O_3 substitution by La^{3+} in the measured samples. However, the interpretation is not so obvious as in small particles both the particle size reduction and the size substitution lead to the reduction of magnetic hyperfine field [48, 60].

The increase of the value of the hyperfine field of α-Fe_2O_3 with increasing particle size is observed. This coincides with the general theory that small particle size decreases the hyperfine field. However, by comparing the value of the hyperfine field for sample with the highest amount of La^{3+} (La05_Co05_900) 50.3 T to the sample with 10 times lower amount of La^{3+} with nearly the same particle size (La005_Co095_1100) 51.2 T , a significant decrease of the B_{hf} value is observed. This observation suggests that the La^{3+} ions are also introduced into α-Fe_2O_3 .

Table 4.15: The Mössbauer parameters of the sol-gel samples measured at room temperature:

	Isomer shift δ ($mm.s^{-1}$)	Quadrupole splitting ΔE_q ($mm.s^{-1}$)	Hyperfine field B_{Hf} (T)	FWHM ($mm.s^{-1}$)	Rel. area (%)	Interpretation
La005_Co095_800						
Subsp. 1	0.29	-0.01	47.6	0.36	39.8	Fe^{3+} T_d
Subsp. 2	0.32	-0.06	43.6	0.93	30	Fe^{3+} O_h
Subsp. 3	0.38	-0.02	50.3	0.40	13.2	Fe^{3+} La_hem
Subsp. 4	0.36	0.00	N/A	2.75	17	Fe^{3+} super/para
La005_Co095_900						
Subsp. 1	0.29	0.0	48.3	0.47	48.8	Fe^{3+} T_d
Subsp. 2	0.30	-0.06	44.9	0.76	31.1	Fe^{3+} O_h
Subsp. 3	0.38	-0.2	50.9	0.37	17.0	Fe^{3+} La_hem
Subsp. 4	0.29	0.66		0.35	3.1	Fe^{3+} super/para
La05_Co05_900						
Subsp. 1	0.30	0.0	47.9	0.51	27.2	Fe^{3+} T_d
Subsp. 2	0.36	-0.09	43.6	1.12	25.6	Fe^{3+} O_h
Subsp. 3	0.38	-0.2	50.3	0.38	29.1	Fe^{3+} La_hem
Subsp. 4	0.35	-1.03	-	1.97	18.1	Fe^{3+} super/para
La005_Co095_1000						
Subsp. 1	0.28	0.00	48.6	0.46	54.5	Fe^{3} T_d
Subsp. 2	0.31	-0.08	45.5	0.69	29	Fe^{3+} O_h
Subsp. 3	0.38	-.02	51.2	0.39	16.5	Fe^{3+} La_hem
La005_Co095_1100						
Subsp. 1	0.29	0.00	49.0	0.41	50.3	Fe^{3+} T_d
Subsp. 2	0.32	0.00	46.8	0.59	29.7	Fe^{3+} O_h
Subsp. 3	0.38	-0.20	51.5	0.37	20.0	Fe^{3+} La_hem

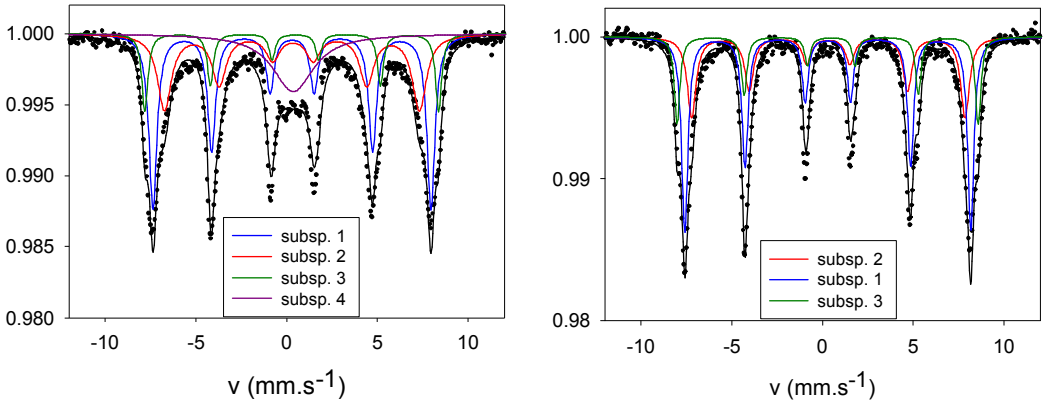

Figure 4.18: Mössbauer spectra of the La005_Co095_800 (left plot) and La005_Co095_1100 (right plot) samples measured at room temperature.

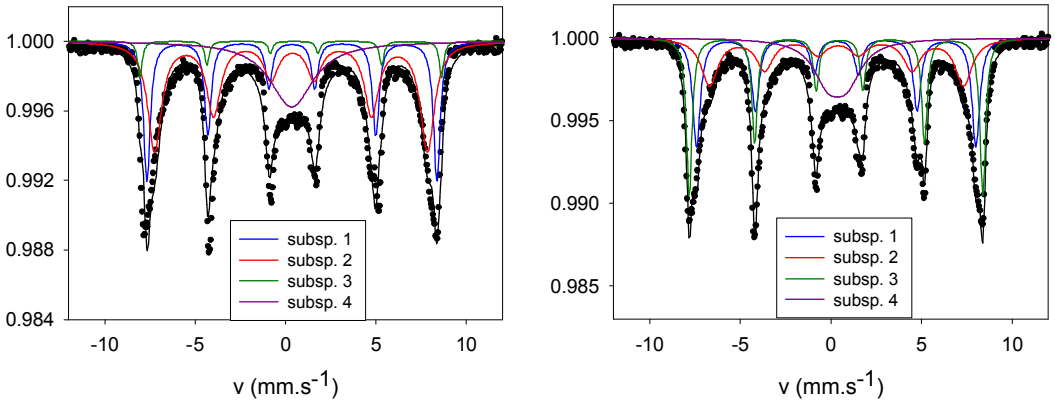

Figure 4.19: Mössbauer spectra of the La05_Co05_900 sample measured at room temperature. On the left is model using the values for pure α-Fe_2O_3, on right is the best mathematical fit with the "unlocked" B_{hf}.

4.2.3.2. In-field Mössbauer spectroscopy

The La005_Co095_900, La05_Co05_900 and La005_Fe195_800 samples were measured at 4.2 K with and without 6 T applied field perpendicular to the direction of γ-rays.

The expected splitting of the overlapped sextets by the applied field was observed (see Figures 4.20 and 4.21). For both samples annealed at 900°C the doublet appears at low temperature without applied field indicating that small amount of the sample in paramagnetic state. The in-field spectra were treated in the same way as in case of the samples prepared by the microemulsion method. The obtained Mössbauer parameters are summarized in Table 4.16.

Table 4.16: The in-field Mössbauer parameters of the sol-gel samples :

	Isomer shift δ (mm.s^{-1})	Quad. spl. ΔE_q (mm.s^{-1})	Eff. field B_{eff} (T)	Hyp. field B_{Hf} (T)	FWHM (mm.s^{-1})	Rel. area (%)	Interpr.
La005_Co095_900							
Subsp. 1	0.38	0.00	56.4	53.8	0.39	29.2	Fe^{3+} T_d
Subsp. 2	0.49	0.03	48.4	51.5	0.67	59.1	Fe^{3+} O_h
Subsp. 3	0.49	-0.20	53.5	53.5	0.54	9.6	Fe^{3+} Hem_wf
Subsp. 4	0.28	0.37		N/A	0.24	2.1	Fe^{3+} para
La05_Co05_900							
Subsp. 1	0.38	-0.02	56.4	53.4	0.35	15.5	Fe^{3+} T_d
Subsp. 2	0.50	-0.03	48.6	51.4	0.77	41.5	Fe^{3+} O_h
Subsp. 3	0.49	-0.2	53.5	53.5	0.50	38.9	Fe^{3+} Hem_wf
Subsp. 4	0.30	0.41	N/A	N/A	0.34	4.1	Fe^{3+} para
La005_Fe195_800							
Subsp. 1	0.38	-0.01	56.4	53.5	0.42	27.5	Fe^{3+} T_d
Subsp. 2	0.49	0.0	48.4	51.8	0.63	53.1	Fe^{3+} O_h
Subsp. 3	0.49	-0.2	53.5	53.5	0.59	17..3	Fe^{3+} Hem_wf
Subsp. 4	0.31	0.38	N/A		0.39	2.1	Fe^{3+} para

As it was discussed in the theoretical section, the α-Fe_2O_3 undergoes the so-called Morin transitions from the weak ferromagnetic state (wf) to the antiferromagnetic state (af). For pure, bulk α-Fe_2O_3 the Morin temperature is near 260 K. As the local structure of the Fe^{3+} ions is changing, these two states have different Mössbauer parameters therefore these states can be distinguished by Mössbauer spectroscopy. It was observed that in case of nanoparticles, the Morin temperature, T_M is reduced to lower temperature and below critical size (15 – 20 nm) the T_M is completely suppressed [48]. Reduction and diffusion of T_M is also caused by substitution of diamagnetic ion for paramagnetic ion [48, 61]. Therefore it was expected that α-Fe_2O_3 is in weak ferromagnetic state (wf). The spectrum of the La05_Co05_900 sample was fitted in two ways. At first the model with parameters corresponding to af-state were used, but this fit was not successful. Therefore the model for wf-state was fitted and the resulting spectra are shown in Figure 4.20. The tendency of lacking the Morin transition was also determined in other samples. This result supports the idea, that the La^{3+} ion substitute Fe^{3+} in the α-Fe_2O_3. The resulting parameters are presented in Table 4.16.

In Table 4.17 the resulting composition of the samples (with assumption that La^{3+} ions are located in the octahedral sites) and the spin canting angles are presented, where α_1 denotes the tetrahedral sites and α_2 denotes the octahedral sites.

The doping of small amount of La^{3+} ions leads to high spin canting, however the canting angles does not change with the increasing amount of La^{3+}. As was discussed before, in the highly La-doped samples the La^{3+} ions are mostly presented in α-Fe_2O_3 . Therefore any significant change in the canting angles was not registered as they are calculated for the spinel structure only. Second reason for the unchanged canting angles could be due to higher error of determination of these angles as the sextets are not well resolved.
The spinel structures of the La005_Co095_900 and La005_Fe195_800 samples are not completely inverse, the degree of inversion is in the same order as in samples prepared by the microemulsion route. On the other hand the structure of the sample La05_Co05_900 corresponds to almost normal spinel that is in agreement with the results reported by L. B. Tahar [9] that due to the presence of La^{3+} ions in spinel lattice the Co^{2+} ions transfer from the octahedral sites to tetrahedral sites and Fe^{3+} ions transfer in opposite way to relax the strain.

Table 4.17: The spin canting angles and composition of the sol-gel samples:

Sample	α_1 (°)	α_2 (°)	composition
La005_Co095_900	67	123	$(Co_{0.34}Fe_{0.66})[Co_{0.61}Fe_{1.34}La_{0.05}]O_4$
La05_Co05_900	64	121	$(Co_{0.46}Fe_{0.64})[Co_{0.04}Fe_{1.46}La_{0.5}]O_4$
La005_Fe195_800	64	128	$(Co_{0.37}Fe_{0.63})[Co_{0.63}Fe_{1.32}La_{0.05}]O_4$

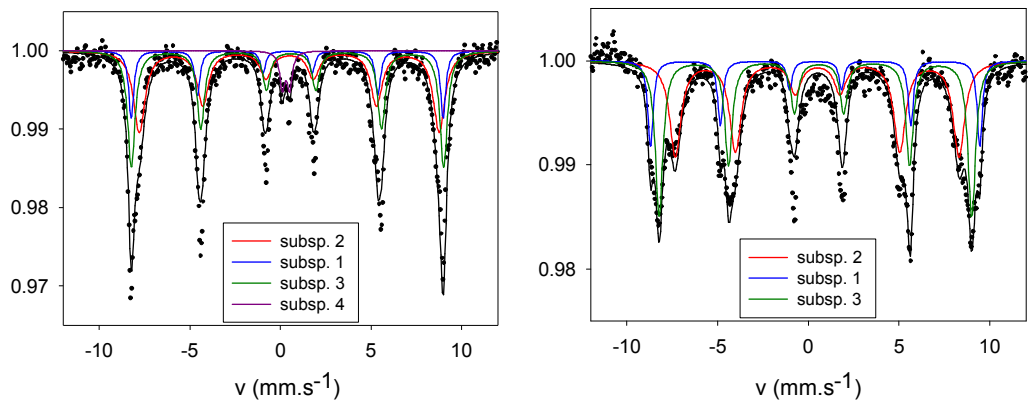

Figure 4.20: Mössbauer spectra of La05_Co05_900 measured at 4.2 K in the absence (left plot) and presence (right plot) of the external field.

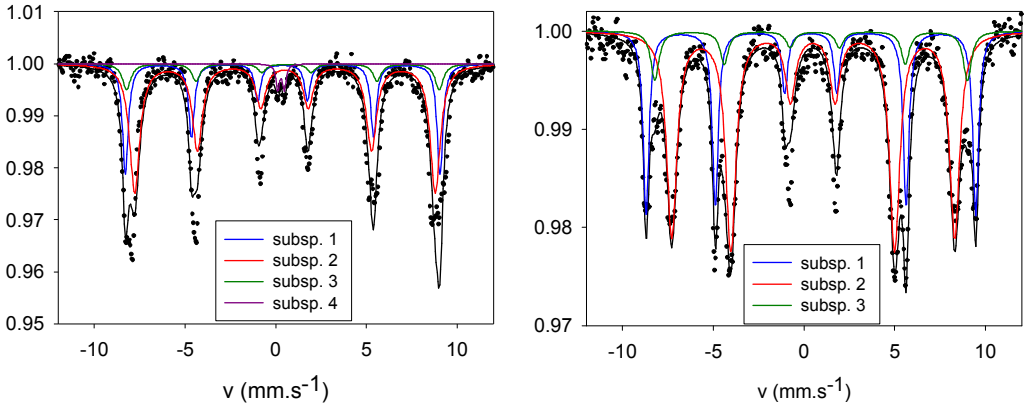

Figure 4.21: Mössbauer spectra of La005_Co095_900 measured at 4.2 K in the absence (left plot) and presence (right plot) of the external field.

4.2.4. Magnetic measurements

The ZFC-FC measurements were performed in the temperature range 10 – 400 K with the applied field of 10 mT. The magnetization isotherms were measured at different temperatures. The magnetization of all experimental data was finally recalculated on the cobalt ferrite content (without SiO_2 matrix).

4.2.4.1. ZFC-FC measurement

All the sol-gel samples show the same behavior as is demonstrated in Figure 4.22 for the La005_Co095_800 and La005_Fe195_800 samples. No maxima of the ZFC curves and no bifurcation points were observed indicating that the blocking temperature is well above 400 K. All samples contain at least detectable amount of the α-Fe_2O_3, however no feature in the ZFC curve indicating the Morin transition was observed. This is consistent with the results of Mössbauer spectroscopy, where it was shown that the Morin transition is completely suppressed.

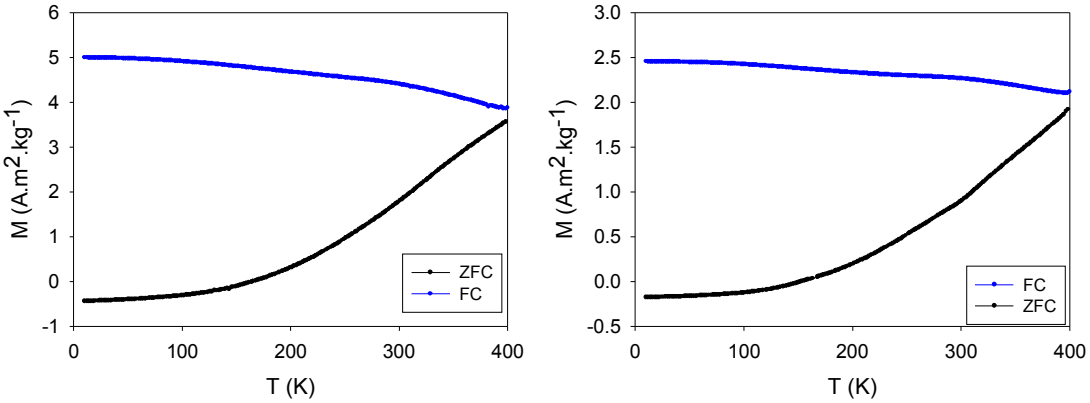

Figure 4.22: Temperature dependence of ZFC-FC magnetization of the La005_Co095_800 (left plot), La005_Fe195_800 (right plot) samples at 10 mT.

4.2.4.2. Hysteresis loops

Hysteresis loops were measured at different temperatures between 10 K – 400 K up to the applied magnetic field of 7 T (see Figures 4.23 and 4.24). There is no saturation magnetization even at maximum applied field, probably due to the non-negligible surface effect [57-58] causing the spin canting at the surface. The spin canting was confirmed by Mössbauer spectroscopy. The obtained results of the coercivity, magnetization at 7 T and remanent magnetization for the samples where the La^{3+} ions were doped instead of the Co^{2+} and Fe^{3+} ions are summarized in Table 4.18. and Table 4.19, respectively.

The high coercivity up to 2 T at 10 K was observed that is comparable with undoped $CoFe_2O_4$ prepared by the identical sol-gel method [5]. As expected, the increasing annealing temperature implies increase of the particle size, which generally yields the increase of the coercivity. This effect was expected as is consistent with relation (2.27).

Comparing coercivity of the La005_Co095_900 and La05_Co05_900 samples that has nearly similar particle size, it is obvious that doping of higher amount of La^{3+} does not make any significant change in its value. The reason can be explained by the fact that the La^{3+} ions in higher amount preferably substitute the α-Fe_2O_3 .

The coercivity is much lower in samples where the La^{3+} ions were doped instead of the Fe^{3+} ions as it is compatible with the analogues results from samples prepared by the microemulsion route.

The values of magnetization at 7 T are significantly lower than expected (80 $A.m^2.kg^{-1}$) that is consistent with the high canting angles of the magnetic moments of Fe^{3+} that was determined by Mössbauer spectroscopy. It was observed by other authors [24, 57, 58] that the so-called spin canting causes a significant decrease of the saturation magnetization.

The different values of the magnetization at 7 T in the La001_Fe199_800 and La005_Fe195_800 samples is rather caused by different cation distribution within

spinel structure than different level of doping. To confirm this idea the in-field Mössbauer spectroscopy experiment is needed.

Table 4.18: The coercivity (H_C), remanent magn. (M_r) and magn. at 7 T (M_{7T}) of the sol-gel samples:

sample	T (K)	H_C (T)	M_{7T} (A.m^2.kg^{-1})	M_r (A.m^2.kg^{-1})
La005_Co095_800	10	1.37	66.9	45.7
	400	0.00	47.3	1.5
La005_Co095_900	10	1.71	49.6	37.3
	200	0.29	47.7	19.2
	400	0.03	36.0	5.0
La05_Co05_900	10	1.79	46.8	30.7
	400	0.02	31.5	3.2
La005_Co095_1000	10	1.96	70.8	54.1
	100	1.19	70.4	47.7
	200	0.45	67.9	29.9
	400	0.08	54.5	13.3
La005_Co095_1100	10	1.65	89.1	66.1
	100	1.01	89.0	59.7
	200	0.38	85.7	42.5
	300	0.17	78.5	29.6
	400	0.09	68.8	23.0

Table 4.19: The coercivity (H_C), remanent magn. (M_r) and magn. at 7 T (M_{7T}) of the sol-gel samples:

sample	T (K)	H_C (T)	M_{7T} (A.m^2.kg^{-1})	M_r (A.m^2.kg^{-1})
La001_Fe199_800	10	1.18	44.8	29.9
	400	0.03	32.4	5.9
La005_Fe195_800	10	1.16	65	42.6
	200	0.25	60.3	25.3
	400	0.03	46.7	8.0
La01_Fe19_800	10	1.20	60.8	40.0
	400	0.02	42.6	5.0

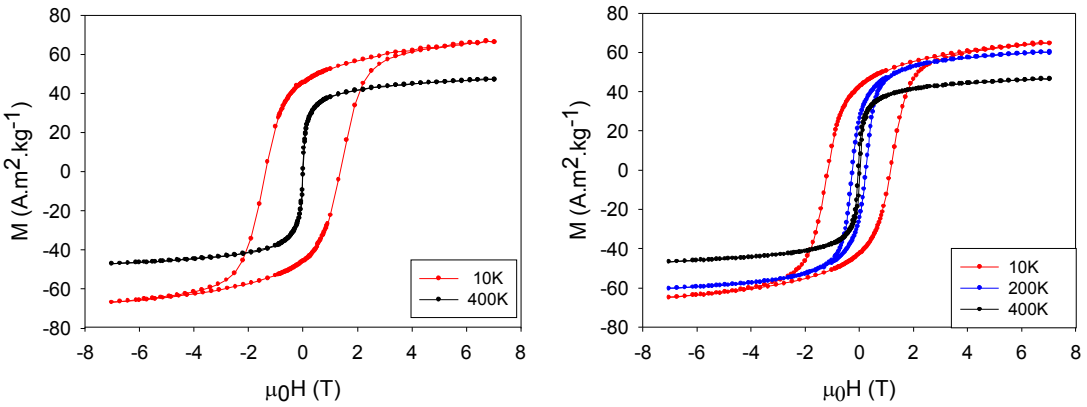

Figure 4.23: Hysteresis loops of the La005_Co095_800 (left plot), La005_Fe195_800 (right plot) samples measured at different temperatures.

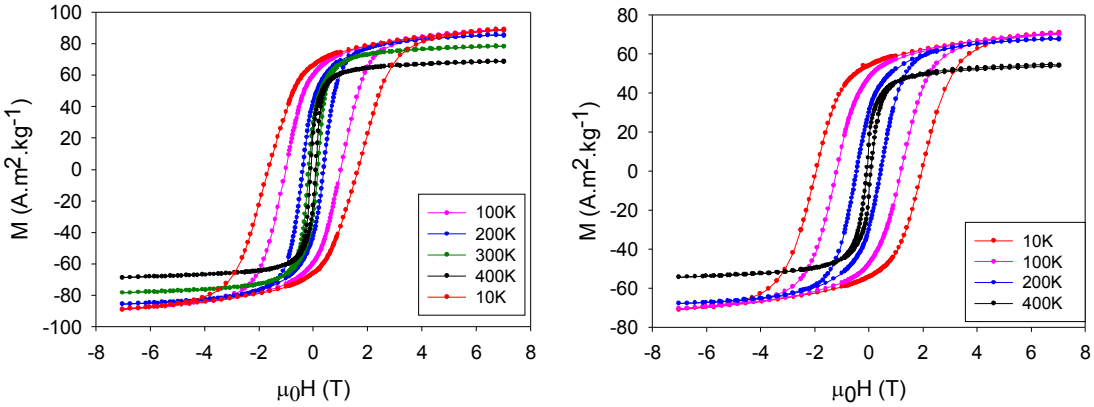

Figure 4.24: Hysteresis loops of the La005_Co095_1100 (left plot) and La005_Co095_1000 (right plot) samples measured at different temperatures.

4.2.5. Leached sample

The sample La005_Co095_800 was leached with purpose to remove the amorphous SiO_2 matrix (see Experimental part 3.1.3.). The goal was to investigate influence of the silica matrix on magnetic properties, namely the inter-particle interactions. The removing of the SiO_2 matrix was confirmed by XRD (Figure 4.25). After leaching process the broad peak near 25° corresponding to the SiO_2 matrix disappeared. By the Rietveld refinement the lattice parameters and particle size were subsequently obtained (see Table 4.20). There is no significant change of size of the $CoFe_2O_4$ nanoparticles after leaching, however the particle size of the α-Fe_2O_3 nanoparticles rapidly decreased.

Table 4.20: Lattice parameters of La005_Co095_800 with and without SiO_2 matrix:

	$CoFe_2O_4$		α-Fe_2O_3		
Sample	*d* (nm)	*a* (Å)	*d* (nm)	*a* (Å)	*c* (Å)
La005_Co095_800	9	8.39(1)	16	5.04(9)	13.74(9)
La005_Co095_800_leach	8	8.39(2)	7	5.06(0)	13.71(4)

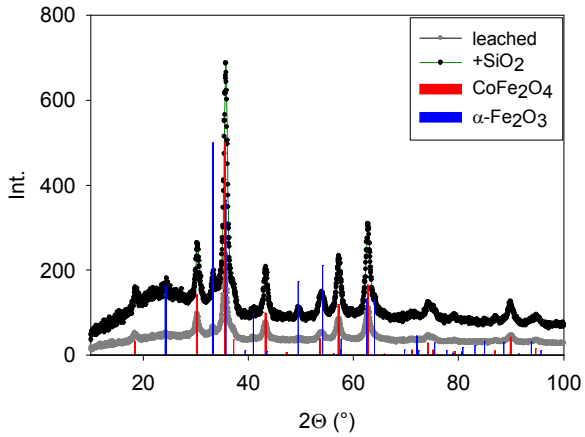

Figure 4.25: Comparison of X-ray diffraction pattern of La005_Co095_800 with and without SiO_2 matrix (leached).

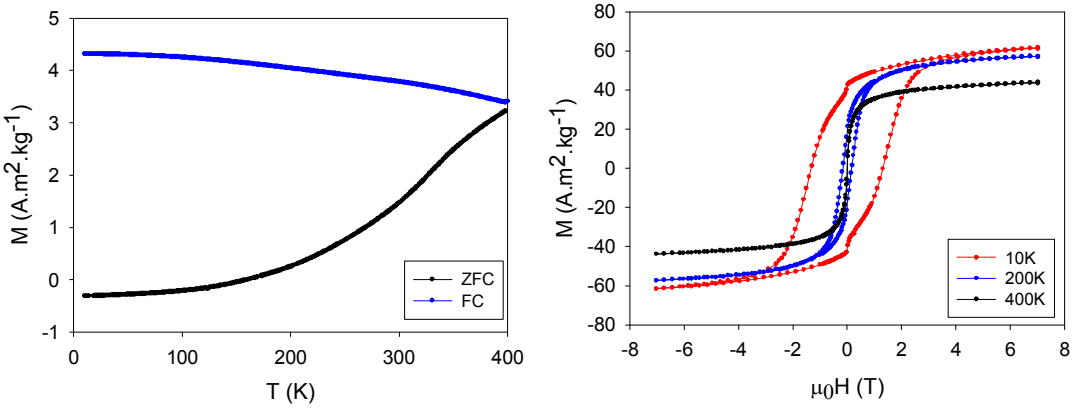

Figure 4.26: Temperature dependence of the ZFC-FC magnetization (left plot) and hysteresis loops (right plot) of the La005_Co095_800_leach sample.

The ZFC-FC curves of the La005_Co095_800_leach sample show identical behavior as the La005_Co095_800 sample with the silica matrix. Also the coercivity and magnetization at 7 T did not significantly change. By removing the diamagnetic matrix the nanoparticles are closer together that should increase the inter-particle interactions of dipolar origin. Therefore the increase in coercivity is expected. The lack of the effect supports the fact that the enhanced coercivity observed is due to significant inter-particle interactions already in the presence of the silica. Typically, the $CoFe_2O_4$ nanocrystals with high crystallinity show maximum coercivity of 1.2 T [62], while the

nanoparticles obtained by the sol-gel method exhibit lower crystallinity resulting in large number of surface defects, which enhance the channels of the dipolar interactions. Therefore, any coarsing of the crystallites does not enhance the coercivity significantly.

Table 4.21: The coercivity (H_C), remanent magn. (M_r) and magn. at 7 T (M_{7T}) of the leached sample:

sample	T (K)	H_C (T)	M_{7T} (A.m^2.kg^{-1})	M_r (A.m^2.kg^{-1})
La005_Co095_800	10	1.37	66.9	45.7
	400	0.00	47.3	1.5
La005_Co095_800_leach	10	1.32	61.3	41.4
	200	0.17	57.5	18.6
	400	0.00	43.9	1.3

4.2.6. Summary: The microemulsion vs. sol-gel samples

In all samples the spinel structure was confirmed from the XRD measurements. In the sol-gel samples the α-Fe_2O_3 phase also appeared and the samples with higher doping amount of La^{3+} ($x > 0.2$) were found out to be multiphase. The lattice parameters and particle diameters are summarized in Table 4.22. There was not observed any significant increase of the lattice parameter exclude the La03 sample, where La^{3+} was substituted instead of Fe^{3+}. The La-doping affects the particle size of samples prepared by the microemulsion route. On the other hand, in the sol-gel method the particle size is tuned by the final annealing temperature only.

Table 4.22: Comparison of lattice parameters and particle diameters:

Microemulsion route			Sol-gel method		
sample	*d* (nm)	*a* (Å)	sample	*d* (nm)	*a* (Å)
Substitution instead of Co^{2+}					
Co550	22	8.39(8)	La005_Co095_800	9	8.39(1)
Co750	26	8.37(7)	La05_Co05_800	5	8.37(5)
Co950	33	8.38(7)	La005_Co095_900	11	8.39(5)
La01	4.2	8.38(0)	La05_Co05_900	11	8.39(1)
La02	4.2	8.35(7)	La005_Co095_1000	15	8.39(8)
Substitution instead of Fe^{3+}					
La03	5.7	8.42(9)	La001_Fe199_800	12	8.36(6)
			La005_Fe195_800	12	8.36(1)
			La01_Fe19_800	10	8.39(3)

The comparison of results from magnetic measurements at 10 K is presented in Table 4.23. The both kinds of samples show the increase of the coercivity with increasing particle size and the higher spin canting angles for the samples doped with La^{3+} that results in the lower saturation magnetization. The undoped $CoFe_2O_4$ prepared by the microemulsion route show significantly lower coercivity than the sol-gel samples even their particle size is larger. The significant decrease of the coercivity in cobalt ferrite nanoparticles prepared by microemulsion method in comparison to the same-sized nanoparticles prepared by the sol-gel method were also observed by other authors [63]. The sol-gel samples show the significant inter-particle interactions within the silica matrix that contributes to the effective anisotropy constant, therefore the coercivity is larger. In the case of the microemulsion route the samples are matrix free therefore only the intrinsic contribution to the anisotropy constant dominates.

Table 4.23: Comparison of coercivity (H_C), remanent magn. (M_r) and magn. at 7 T (M_{7T}) at 10 K:

Microemulsion route				Sol-gel method			
sample	H_c	M_{7T}	M_r	sample	H_c	M_{7T}	M_r
	(T)	($A.m^2.kg^{-1}$)			(T)	($A.m^2.kg^{-1}$)	
Substitution instead of Co^{2+}							
Co550	0.52	88.4	56.5	La005_Co095_800	1.4	66.9	45.7
Co750	0.73	84.3	60.1	La005_Co095_900	1.7	49.6	37.3
Co950	0.9	60.7	31.2	La005_Co095_1000	2.0	70.8	54.1
La01	1.0	53.7	26.3	La005_Co095_1100	1.65	89.1	66.1
La02	1.03	53.7	26.3	La05_Co05_900	1.8	46.8	30.7
Substitution instead of Fe^{3+}							
La03	0.2	62.1	23.4	La001_Fe199_800	1.2	44.8	29.9
				La005_Fe195_800	1.2	65.0	42.6
				La01_Fe19_800	1.2	60.8	40.0

5. Conclusions

To conclude, aim of the work was to investigate the crystal structure and magnetic properties of $CoFe_2O_4$ nanoparticles upon La-doping. For this purpose, two different kinds of samples were used – they were prepared by the microemulsion route and the sol-gel method, respectively.

In the former case, the samples were matrix-free and they were found out to be mostly single-phase. It was observed that the La-doping affects the particle size; the doped particles are typically 5 nm in diameter, while the undoped $CoFe_2O_4$ show 25-30 nm. The Mössbauer spectroscopy was performed to study the cation distribution within the spinel structure and to determine the spin canting of magnetic moments of the Fe^{3+}. Upon La-doping the Fe^{3+} spins were more canted than in undoped $CoFe_2O_4$. The magnetic measurements indicated that the blocking temperature of undoped $CoFe_2O_4$ is much higher in comparison to the La-doped samples that is mainly due to different particle size. The a.c. susceptibility showed that the inter-particle interactions are not negligible in samples and they cannot be treated by the Vogel-Fulcher law, which is valid only in case of weak interactions. Doping of La^{3+} instead of Fe^{3+} dramatically changes the magnetic properties of $CoFe_2O_4$ as demonstrated by the lowering coercivity (0.2 T at 10 K). To explain this effect further studies are needed.

In the latter case, the samples were encapsulated in SiO_2 matrix and they were found out to be at least double-phase; in all samples the α-Fe_2O_3 was also detected. Doping of the higher amount of La^{3+} (critical value $x = 0.2$) caused precipitation of extra phases as lanthanum orthoferrite, cobalt silicate and lanthanum tri-oxide. These samples also showed high spin-canting angles that lowers their saturation magnetization at 7 T. Moreover the La^{3+} ions caused the redistribution of Co^{2+} and Fe^{3+} within the spinel network. Magnetization measurements confirmed the large values of coercivity that increased with increasing particles size (up to 2 T in 10 K for the 16 nm nanoparticles).

It is claimed that the La^{3+} ions are also well introduced into the α-Fe_2O_3 that was supported by several independent observations. First, the lattice parameters of α-Fe_2O_3 increased with increasing amount of La^{3+} ions. Second, the lower values of the hyperfine fields both in room-temperature and in low-temperature in-field Mössbauer spectroscopy were observed. Third, no change in the coercivity with increasing amount of the La^{3+} ions was detected.

The expected changes in magnetic properties upon La-doping were not straightforward. It is suggested that the cation distribution (by means of the inversion of the spinel structure) and the particles size govern the magnetic properties in the sol-gel samples, because most of the La^{3+} substitutes the Fe^{3+} in α-Fe_2O_3. In the samples prepared by the microemulsion route, the particle size is much different when introducing $La^{3+,}$ therefore the obtained magnetization data are not easily comparable. To obtain more

information about our samples, the HR-TEM measurements, infrared and Raman spectroscopy are in progress.

The obtained results will be used to optimize the conditions of preparation in order to get well-crystalline single-phase samples with controlled size.

6. References

[1] Ch. Liu, A. J. Rondinone, Z. J. Zhang (2000): *Chemical control of superparamagnetic properties of magnesium and cobalt spinel ferrite nanoparticles through atomic level couplings*, J. Am. Chem. Soc. **122**, 6263-6267

[2] J. Vejpravova, V. Sechovsky, J. Plocek et al (2005): *Magnetism of sol-gel fabricated $CoFe_2O_4/SiO_2$ nanocomposites*, J. Appl. Phys. **97**, 124304

[3] G.A. Sawatzky, F. Van Der Woude, A. H. Morrish (1969): *Mössbauer study of several ferimagnetic spinels*, Phys. Rev. **187**, 747

[4] P. W. Anderson (1956): *Ordering and antiferromagnetism in ferrites*, Phys. Rev. **102**, 1008

[5] A. Hutlova, D. Niznansky, J. Rehspringer et al (2003): *High coercive field for nanoparticles of $CoFe_2O_4$ in amorphous silica sol-gel*, Adv. Mater. **15**, 1622

[6] M. Grigorova, H.J.Blythe, V. Blaskov et al (1998): *Magnetic properties and Mössbauer spectra of nanosized $CoFe_2O_4$ powders*, J. Magn. Magn. Mater. **183**, 163-172

[7] M. George, S. S. Nair, K. A. Malini (2007): *Finite size effects on the electrical properties of sol-gel synthetized $CoFe_2O_4$ powders: Deviation from Maxwell-Wagner theory and evidence of surface polarization effets*, J. Phys. D: Appl. Phys. **40**, 1593-1602

[8] M. Pita, J. M. Abad, C. Van-Dominguez et al (2008): *Synthesis of cobalt ferrite core/metallic shell nanoparticles for the development of a specific PNA/DNA sensor*, J. Colloid Interface Sci. **321**, 484-492

[9] L. Ben Tahar, M. Artus, S. Ammar et al (2008): *Magnetic properties of $CoFe_{1.9}RE_{0.1}O_4$ nanoparticles (RE = La, Ce, Nd, Sm, Eu, Gd, Tb, Ho) prepared in polyol*, J. Magn. Magn. Mater. **320**, 3242-3250

[10] L. Ben Tahar, L.S. Smir, M. Artus et al (2007): *Characterization and magnetic properties of Sm- and Gd-substituted $CoFe_2O_4$ nanoparticles prepared by forced hydrolysis in polyol*, Mat. Sci Forum **42**, 1888-1896

[11] W. Ch. Kim, S. W. Lee, S.J. Kim et al (2000): *Magnetic properties of Y-, La-, Nd-, Gd- and Bi-doped ultrafine $CoFe_2O_4$ spinel grown by using a sol-gel method*, J. Magn. Magn. Mater. **215-216**, 217-220

[12] M. L. Kahn, Z. J. Zhang (2001): *Synthesis and magnetic properties of $CoFe_2O_4$ spinel ferrite nanoparticles doped with lanthanide ions*, Appl. Phys. Lett. **78**, 3651

[13] S. Blundell (2001): *Magnetism in Condensed Matter*, Oxford University Press, New York

[14] N. W. Ashcroft. N. D. Mermin (1976): *Solid State Physics*, Harcourt College Publisher

[15] V. Sechovsky: Presentation of lecture NFPL122

[16] S. Krupička (1969): *Fyzika Feritů a Příbuzných Kysličníků*, Academia, Praha

[17] http://wwwchem.uwimona.edu.jm:1104/courses/CFT.html)

[18] Ch. Kittel (1946): *Theory of the structure of ferromagnetic domains in films and small particles*, Phys. Rev. **70**, 965
[19] M. Knobel, W.C. Nunes, L. M. Socolovsky et al (2008): *Superparamagnetism and other magnetic features in granular materials: A review on ideal and real systems*, J. Nanosci. Nanotechnol. **8**, 2836-2857
[20] J. Poltierova Vejpravova: Presentation of lecture: *Magnetic properties of nanoparticles*
[21] S. Shtrikman, E. P. Wohlfart (1981): *The theory of the Vogel-Fulcher law of spin glasses*, Phys. Lett. **85A**, 467
[22] J. L. Dormann, L. Bessais, D. Fiorani (1988*): A dynamic study of small interacting particles:superparamagnetic model and spin-glass laws*, J. Phys. C: Solid State Phys. **21**, 2015
[23] S.Morup, E. Tronc (1994): *Superparamagnetic relaxation of weakly interacting particles*, Phys. Rev. Lett. **72**, 3278
[24] J. M. D. Coey (1971): *Noncollinear spin arrangement in ultrafine ferrimagnetic crystallites*, Phys. Rev. Lett. **27**, 1140
[25] B. L. Lin, X. D. Shen, S. Cui (2007): *Application of nanosized Fe_3O_4 in anticancer drug carriers with target-orientation and sustained-release properties*, Biomed. Mater. **2,** 132
[26] C. V. Gopal Reddy, S. V. Manorama, V. J. Rao (2000): *Preparation and characterization of ferrites as gas sensor materials*, J. Mater. Sci. Lett. **19**, 775-778
[27] N. Rezlescu, N. Iftimie, E. Rezlescu et al (2006): *Semiconducting gas sensor for acetone base on the fine grain nickel ferrite*, Sens. Act. B **114**, 427
[28] L. E. F Néel, Matériaux Ferrimagnétiques
[29] D. S. Mathew, R. S. Juang (2007): *An overview of the structure and magnetism of spinel ferrite nanoparticles and their synthesis in microemulsions,* Chemical Engineering Journal **129**, 51-65
[30] PDF 4 databasis
[31] Q. Song, Z. J. Zhang (2006): *Correlation between Spin-Orbital coupling and the superparamagnetic properties in magnetite and cobalt ferrite spinel nanocrystals*. J. Phys. Chem. B **110**, 11205
[32] L. Pauling, S. B. Hendricks (1925): *The crystal structures of hematite and corundum*, Phys. Rev. **47**, 781
[33] http://www.geol.ucsb.edu/faculty/hacker/geo114A/lectureNotes.htm
[34] G. Adachi, N. Imanaka (1998): *The binary rare earth oxides*, Chem. Rev. **98**, 1479
[35] M. L. Huggins (1922): *The crystal structure of quartz*, Phys. Rev. **19**, 363
[36] http://cst-www.nrl.navy.mil/lattice
[37] T. Caronna F. Fontana, I. N. Sora et al (2009): *Chemical synthesis and structural characterization of the substitution compound $LaFe_{1-x}Cu_xO_3$ (x = 0.0 – 0.4)*, Mat. Chem. Phys. **116**, 645
[38] S. Nomura, R. Santoro, J. Fang et al (1964): *Antiferromagnetism in cobalt orthosilicate*, J. Phys. Chem. Solids **25**, 901

[39] John D. Wright, Nico A. J. M. Sommerdijk (2001): *Sol-Gel Materials Chemistry and Applications*, CRC Press
[40] B. L. Cushing, V. L. Kolesnichenko, Ch. J. O'Connor (2004): *Recent advances in the Liquid/Phase Syntheses of inorganic nanoparticles*, Chem. Rev. **104**, 3893
[41] J. Rodríguez-Carvajal (2000): *An introduction to the program Fullprof*
[42] R. Kuzel: Presentation of lecture NFPL 030
[43] J. Rodríguez-Carvajal: *Study of Micro-Structural Effects by Powder Diffraction Using the Program Fullprof*
[44] P. H. Herber (1984): *Chemical Mössbauer spectroscopy*, Plenum Press, New York
[45] http://www.rsc.org/Membership/Networking/InterestGroups/MossbauerSpect
[46] D. Peddis, M. V. Mansilla, S. Morup (2008): *Spin canting and magnetic anisotropy in ultrasmall $CoFe_2O_4$ nanoparticles*, J. Phys. Chem. B **112**, 8507
[47] V. Rusanov, V. Gushterov, S. Nikolov et al (2009): *Detailed Mössbauer study of the cation distribution in $CoFe_2O_4$ ferrites*, Hyperfine Interact. **191**, 67
[48] E. Murad, J. H. Johnston (1987): *Mössbauer spectroscopy applied to inorganic chemistry*, Vol. 2, Plenum Publishing Corporation
[49] F. Bodker M. F. Hansen, Ch. B. Koch et al (2000): *Magnetic properties of hematite nanoparticles*, Phys. Rev. B **61**, 6826
[50] A. Pankhurst, R. J. Pollard (1990): *Mössbauer spectra of antiferromagnetic powders in applied fields*, J. Phys.: Condens. Matter **2**, 7329-7337
[51] MPMA-Magnetic Property Measurement Systém, User's Manual, Quantum Design, San Diego 2004
[52] PPMS- Physical Property Measurement Systém, User's Manual Quantum Design, San Diego 2004
[53] L. Zhao, H. Yang, X. Zhao et al (2006): *Magnetic properties of $CoFe_2O_4$ ferrite doped with rare earth ion*, Mater. Lett **60**, 1
[54] F. X. Cheng, J. T. Jia, Z. G. Xu et al (1980): *Microstructure, magnetic and magnet-optical properties of chemical synthesized Co-RE (RE=Ho, Er, Tm, Yb, Lu) ferrite nanocrystalline films*, J. Appl. Phys. **86**, 2727
[55] T. Methasiri. K. Yoodee, I. M. Tang (1980): *Magnetic hyperfine fields in $CoFe_2O_4$ Phys*. **101B**, 243
[56] G. A. Petit, D. W. Forester (1971): *Mössbauer study of cobal-zinc ferrite*, Phys. Rev. B **4**, 3912
[57] E. De Biasi, R. D. Bysler, C. A. Ramos et al (2002*): Magnetization enhancement at low temperature due to surface ordering in Fe-Ni-B amorphous nanoparticles*, Physica B Conden. Matt **320**, 203
[58] H. Kachkachi, A. Ezzir, M. Nogues et al (2000): *Surface effects in nanoparticles: application of maghemite γ-Fe_2O_3* Eur. Phys. J. B **14**, 681
[59] Ch. Yan, F. Cheng, Ch. Liao et al (1999): *Sol-gel synthesis, magnetic and magneto-optical properties of $CoFe_{2-x}Tb_xO_4$ nanocrystalline films*, J. Magn. Magn. Mater. **192**, 396-402

[60] E. Murad, U. Schwertmann (1986): *Influence of Al substitution and crystal size on the room-temperature Mössbauer spectrum of hematite*, Clays Clay Miner. **34**, 1
[61] J. K. Srivastava, R. P. Sharma (1972): *Magnetic dilution effects on Morin phase transition in hematite*, Phys. Status Solidi B **49**, 135
[62] A. Repko, unpublished
[63] J. Poltierova Vejpravova, V. Tyrpekl, S. Danis et al (2010): *SSG or SFM state in $CoFe_2O_4$ nano-agglomerates fabricated by micro-emulsion method*, J. Magn. Magn. Mater., in press

7. Appendix

7.1. Samples prepared by the microemulsion route

7.1.1. X-ray diffraction

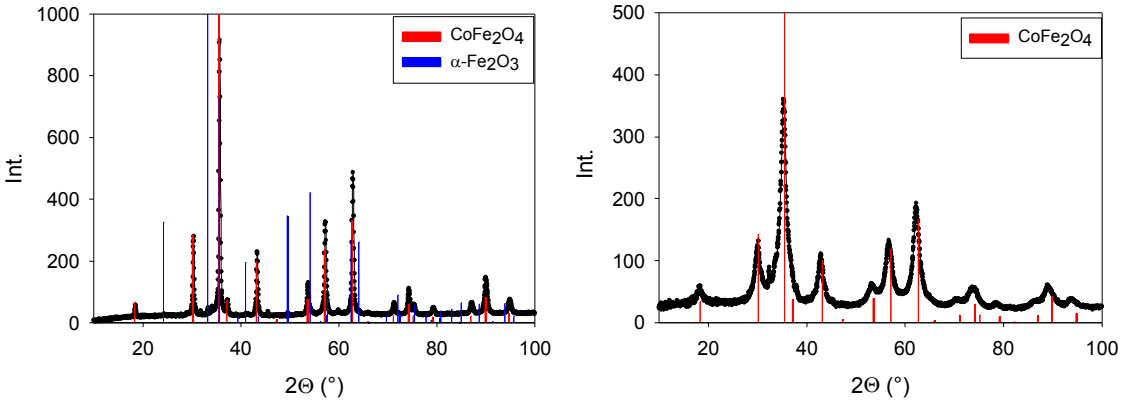

Figure 7.1: X-ray diffraction patterns of the Co750 (left) and La03 (right) samples. The lines demonstrate the Bragg positions of the observed phases

7.1.2. Mössbauer spectroscopy

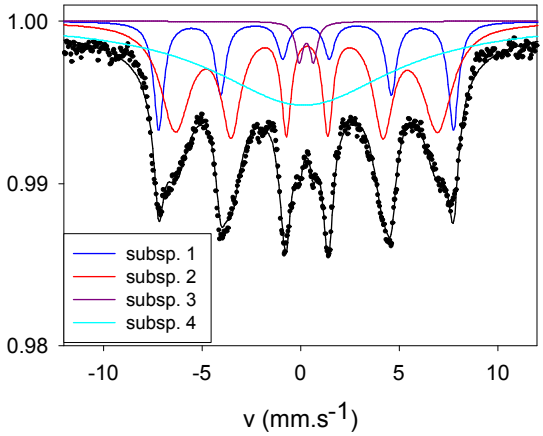

Figure 7.2: Mössbauer spectrum of La01 measured at room temperature. The assignment of individual subspectra can be found in Table 4.4.

7.1.3. ZFC-FC measurements

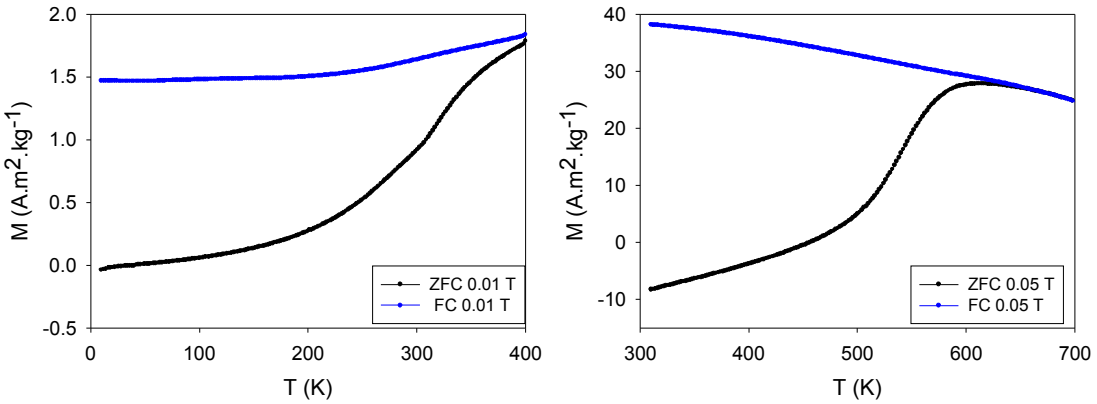

Figure 7.3: Temperature dependence of ZFC-FC magnetization of Co750. The left plot displays the temperature range 10 – 400 K at 0.01 T. The right plot displays the temperature range 310 – 700 K at 0.05T.

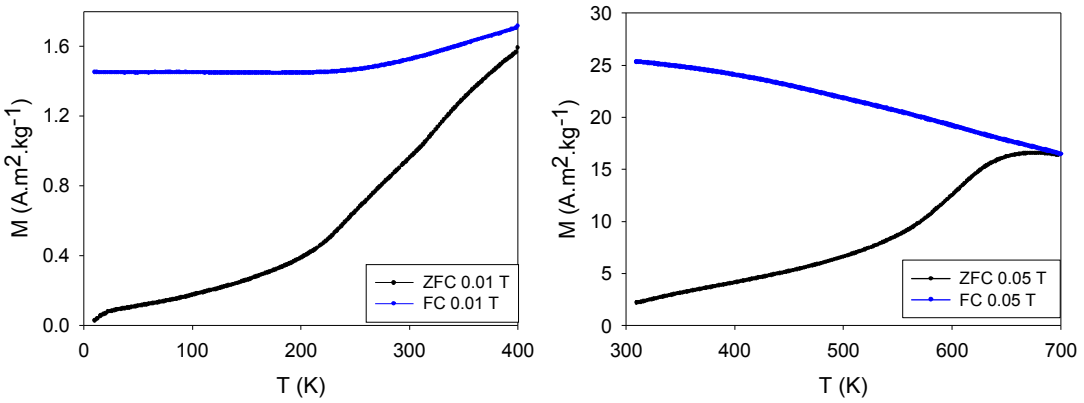

Figure 7.4: Temperature dependence of ZFC-FC magnetization of Co950. The left plot displays the temperature range 10 – 400 K at 0.01T. The right plot displays the temperature range 310 – 700 K at 0.05 T.

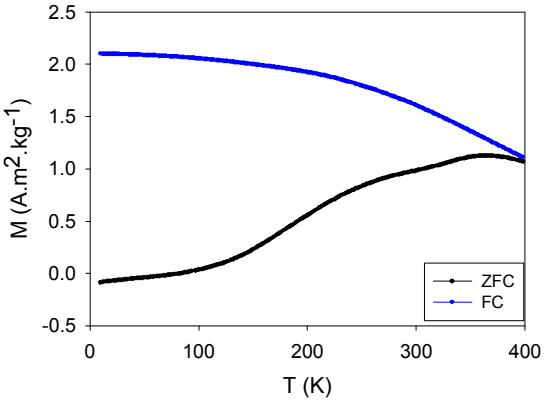

Figure 7.5: Temperature dependence of ZFC-FC magnetization of La02 at 0.01T.

7.1.4. Hysteresis loops

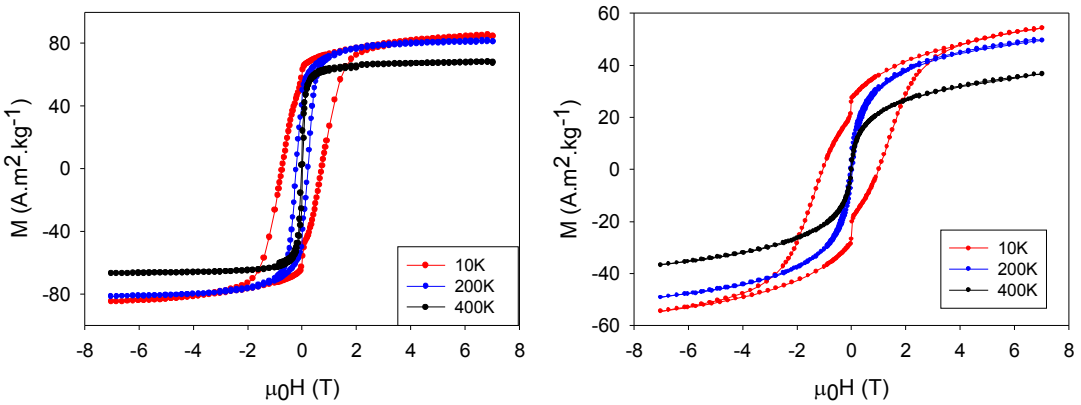

Figure 7.6: Hysteresis loops of the Co750 (left plot) and La02 (right plot) samples measured at different temperatures.

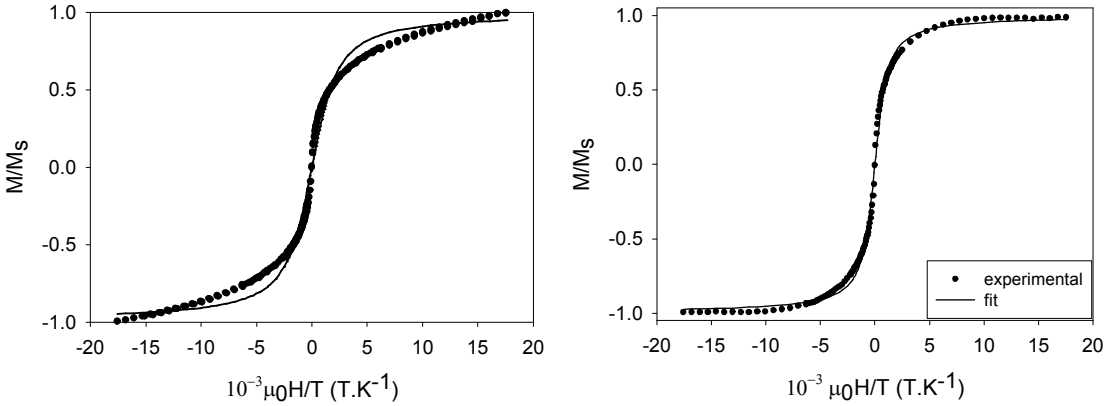

Figure 7.7: Fit of the Langevin function for La02 before correction (left plot) and after correction (right plot) to paramagnetic part of the sample.

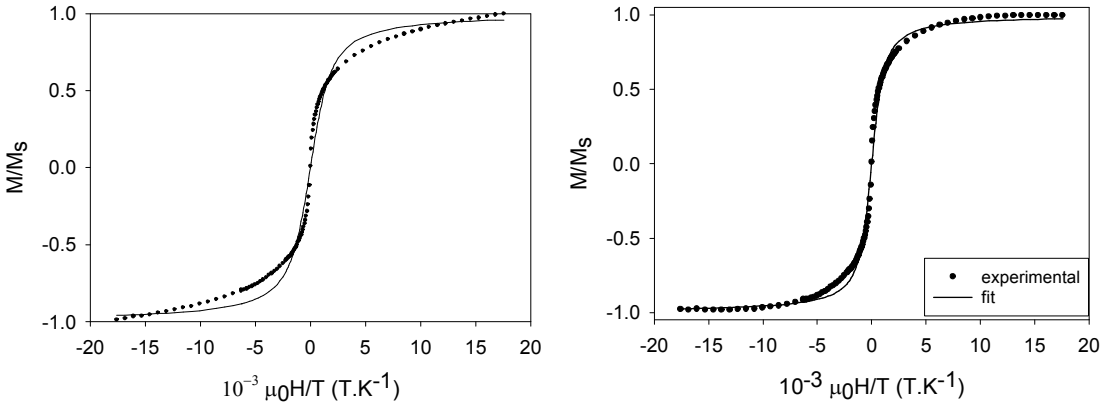

Figure 7.8: Fit of the Langevin function for La03 before correction (left plot) and after correction (right plot) to paramagnetic part of the sample.

7.2. Samples prepared by the sol-gel method

7.2.1. X-ray diffraction

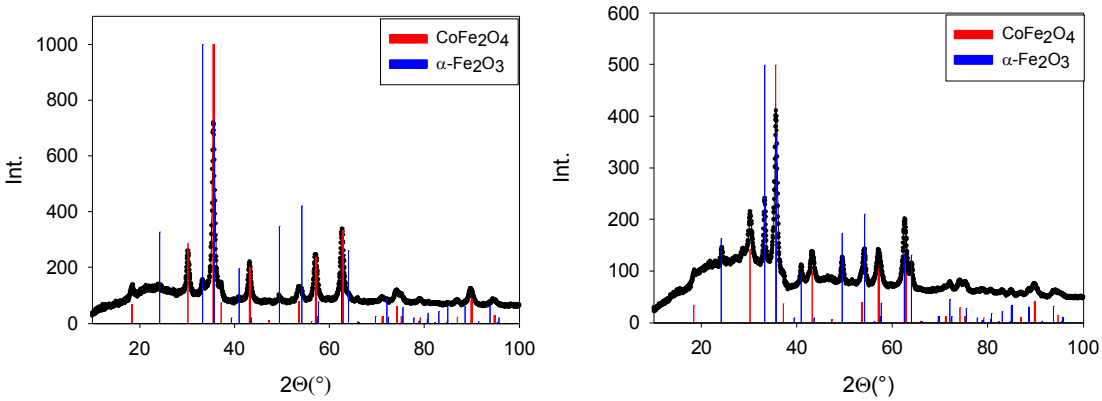

Figure 7.9: X-ray diffraction pattern of the La005_Co095_900 (left plot) and La05_Co05_900 (right plot) samples. The lines demonstrate the Bragg positions of the observed phases

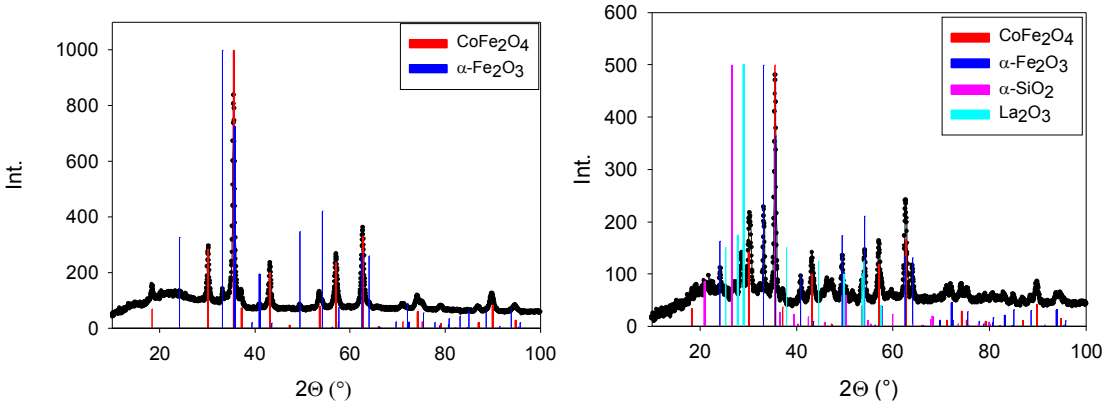

Figure 7.10: X-ray diffraction patterns of the La005_Co095_1000 (left plot) and La05_Co05_1000 (right plot) samples. The lines demonstrate the Bragg positions of the observed phases

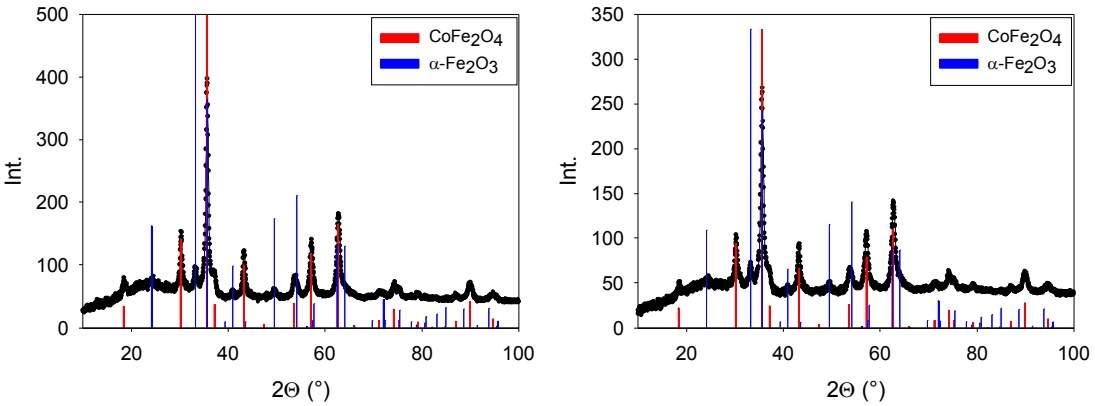

Figure 7.11: X-ray diffraction patterns of the La005_Fe195_800 (left plot) and La01_Co19_800 (right plot) samples. The lines demonstrate the Bragg positions of the observed phase.

7.2.2. Mössbauer spectroscopy

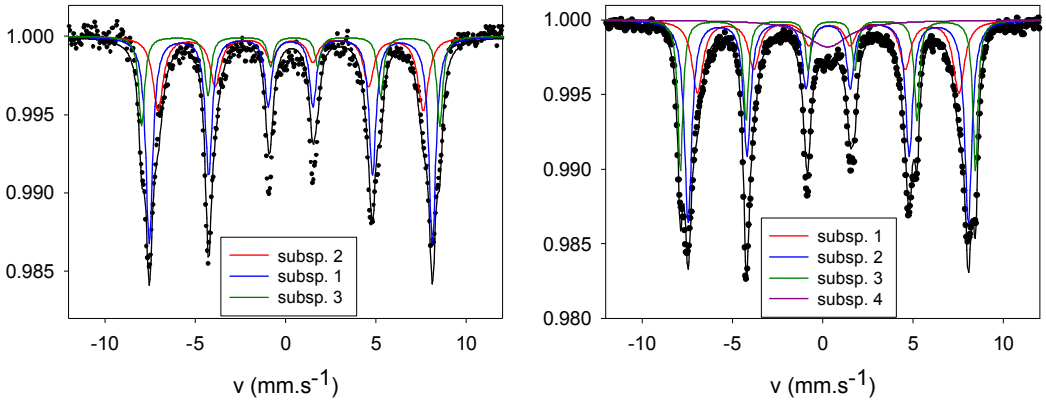

Figure 7.12: Mössbauer spectra of the La005_Co095_1000 (left plot) and La005_Fe195_800 (right plot) samples measured at room temperature. The assignment of individual subspectra can be found in Table 4.15.

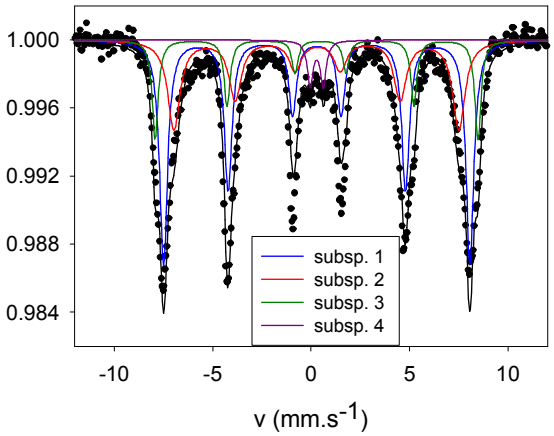

Figure 7.13: Mössbauer spectrum of the La005_Co095_900 sample measured at room temperature. The assignment of individual subspectra can be found in Table 4.15.

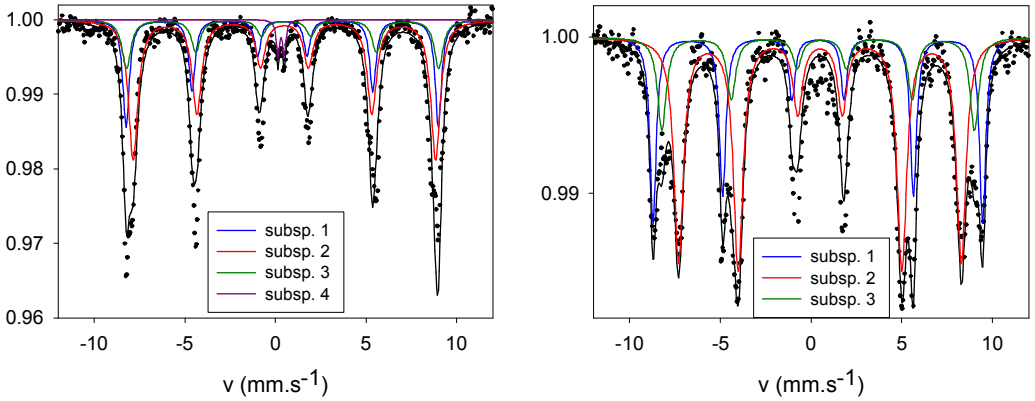

Figure 7.14: Mössbauer spectra of the La005_Fe195_800 measured at 4.2K in the absence (left plot) and presence (right plot) of the external field. The assignment of the individual subspectra can be found in Table 4.16.

7.2.3. ZFC-FC measurement

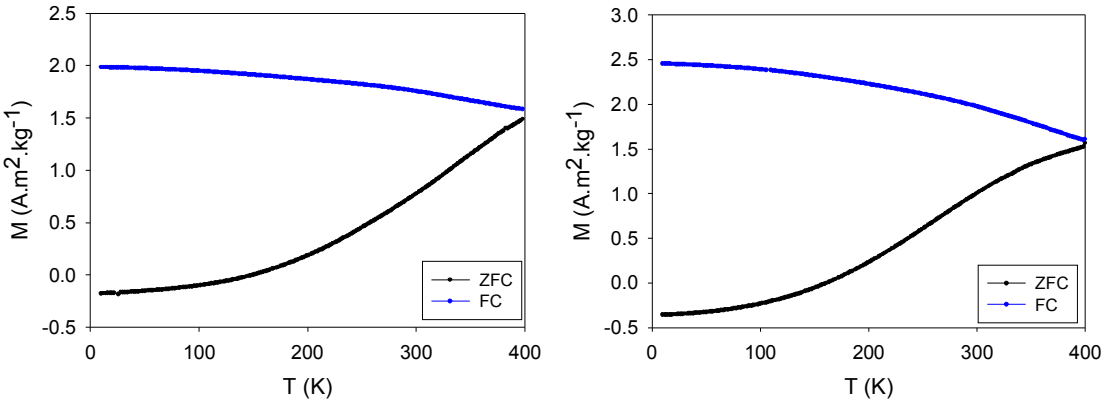

Figure 7.15: Temperature dependence of ZFC-FC magnetization of the La005_Co095_900 (left plot) and La05_Co05_900 (right plot).

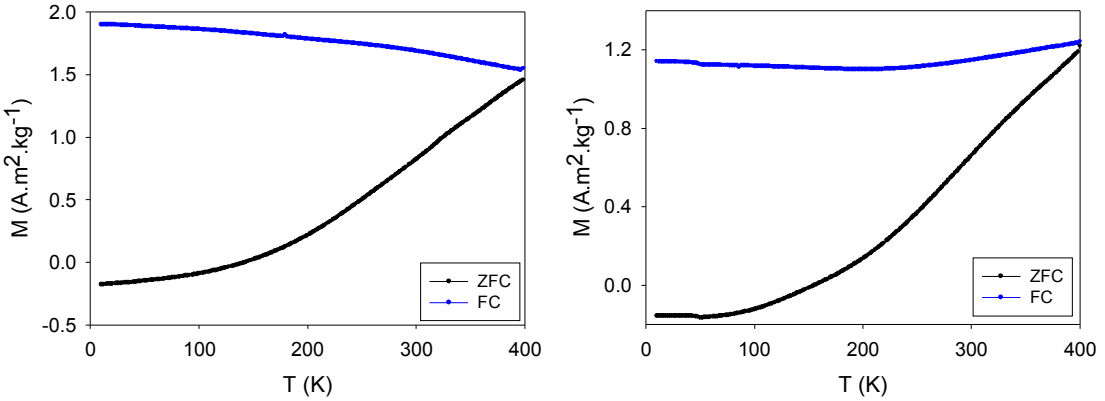

Figure 7.16: Temperature dependence of ZFC-FC magnetization of the La005_Co095_1000 (left plot) and La005_Co095_1100 (right plot).

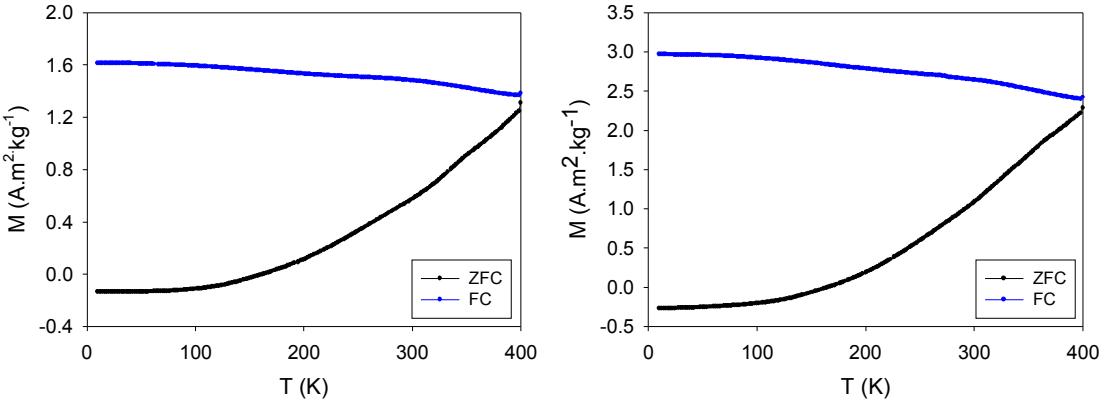

Figure 7.17: Temperature dependence of ZFC-FC magnetization of the La001_Fe199_800 (left plot) and La01_Fe19_800 (right plot).

7.2.4. Hysteresis loops

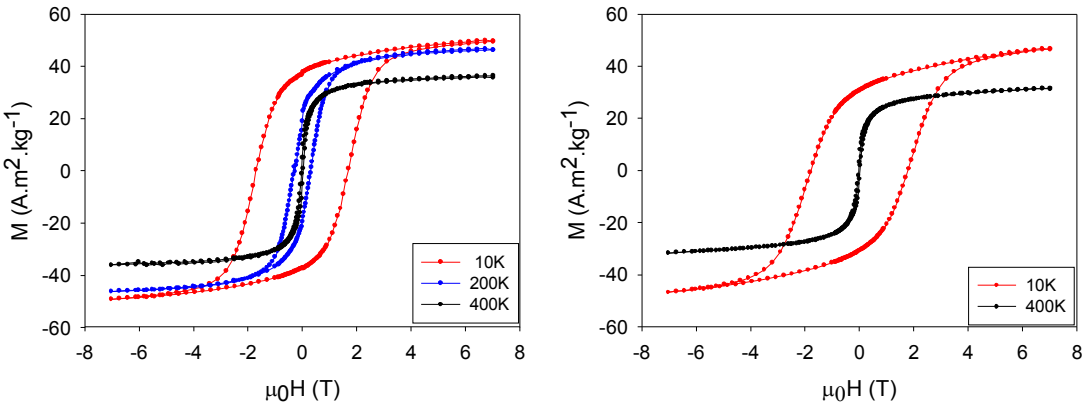

Figure 7.18: Hysteresis loops of the La005_Co095_900 (left plot) and La05_Co05_900 (right plot) samples measured at different temperatures.

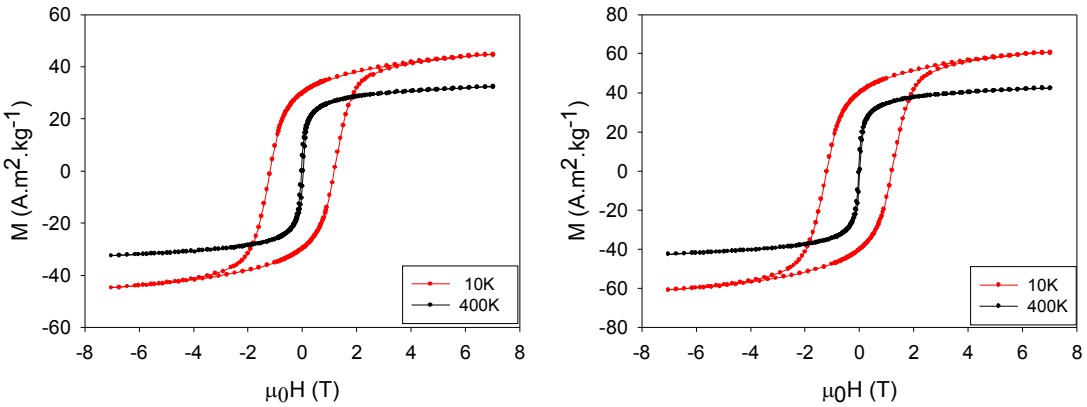

Figure 7.19: Hysteresis loops of the La001_Fe199_800 (left plot) and La01_Fe19_800 (right plot) samples measured at different temperatures.